The Dissertation Committee for Hariharan Ramachandran Certifies that this is the approved version of the following dissertation:

MODELING CO_2 LEAKAGE THROUGH FAULTS AND FRACTURES FROM SUBSURFACE STORAGE SITES

Committee:

Gary A. Pope, Supervisor

Kamy Sepehrnoori

David N. Espinoza

Mojdeh Delshad

Peter Eichhubl

MODELING CO_2 LEAKAGE THROUGH FAULTS AND FRACTURES FROM SUBSURFACE STORAGE SITES

by

Hariharan Ramachandran

Dissertation

Presented to the Faculty of the Graduate School of

The University of Texas at Austin

in Partial Fulfillment

of the Requirements

for the Degree of

DOCTOR OF PHILOSOPHY

The University of Texas at Austin

December 2017

I dedicate my dissertation to my parents and all my teachers

Acknowledgements

I express sincere gratitude to my supervising professor, Dr. Gary A. Pope, for his continued guidance, advice and patience during my doctoral research. I am thankful to Dr. Sanjay Srinivasan for his advice and support during my research. It has been a privilege to work with them. I thank my committee members, Drs Kamy Sepehrnoori, David Espinoza, Mojdeh Delshad and Peter Eichhubl for their suggestions to better this dissertation.

I appreciate the resource and administrative help provided by Joanna Castillo, Frankie Hart, Amy Stewart, Jin Lee and Mary Pettengill. I am thankful to the Geological Carbon Storage (GCS) JIP, for providing financial support for this research. I thank MATLAB, CMG and PVTSIM for providing software used in this research.

I am grateful to my friends, Ashwin Venkatraman, Gurpreet Singh, Himanshu Sharma, Nagarajan Natarajan, Paromita Pain, Sriram Chandrasekhar, Sriram Solairaj and others, for time, conversations and overall support.

I am forever grateful for the support and encouragement of my parents, Ramachandran Venkatrajan and Sarada Ramachandran, my brother, Giridharan Ramachandran and all the extended family members.

MODELING CO_2 LEAKAGE THROUGH FAULTS AND FRACTURES FROM SUBSURFACE STORAGE SITES

Hariharan Ramachandran, Ph.D.

The University of Texas at Austin, 2017

Supervisor: Gary A. Pope

Due to the concerns about the effect of greenhouse gases on the climate, geologic CO_2 storage is a very active area of research. Storage will take place in specifically selected target formations to achieve permanent containment. The biggest risk associated with geological storage is the possibility of leakage. The motivation for this research was the need to have a better understanding of potential leakage scenarios, leakage behavior, factors controlling leakage and other essential information about potential leakage. Possible leakage pathways include faults/fractures and leaky wells. Multiphase flow is likely because spatial gradients in pressure and temperature will occur as the CO_2 flows toward the surface. Below the CO_2 saturation pressure, liquid condensation of the CO_2 may occur. At even lower temperatures and pressures and in the presence of water, hydrate formation may occur. As a consequence, the fluid properties will change and affect leakage mass flux. The main purpose of this dissertation research was to develop and test models needed to estimate the leakage mass flux for different scenarios taking thermodynamic phase changes into account.

A numerical model with coupled mass and energy balances was developed to estimate the flux as a function of time. Due to wide temperature and pressure changes

over the course of the simulation, an accurate fluid properties model was required. The multi-parameter Span-Wagner technical equation of state for CO_2 was used to achieve this. The numerical model allows for CO_2 to exist in gas, liquid and hydrate phases. Heat flux from the surroundings plays an important role because of its effect on the phase behavior. Example calculations indicate a cyclical nature of the leakage mass flux under certain conditions. Hydrate formation results in partial to complete blockage of the fault until melted. The effect of factors such as constant and varying reservoir pressure at the bottom of the fault, permeability and fault effective width were quantified with numerical simulations.

A steady-state flow model was also developed for quick estimation of leakage mass fluxes through faults and fractures. The model was highly simplified and was intended for inclusion in risk assessment studies at the site-selection phase for geologic storage. The model was motivated by geological, non-isothermal properties and multiphase flow considerations. The leakage mass fluxes are calculated assuming two different conditions (1) The temperature of the CO_2 was assumed to be the same as the surroundings based on an assumed geothermal gradient and (2) The temperature of the CO_2 was calculated from the constant flowing total enthalpy specified at the leakage source. The enthalpy is constant when there are no heat losses (adiabatic system). The resulting estimates act as upper and lower bounds for leakage mass flux for a particular set of physical properties of the pathway and surrounding geology. The effects of multiphase coexistence and hydrates on leakage mass flux were quantified. The effects of factors such as reservoir pressure and temperature, depth and permeability that affect multiphase coexistence and leakage mass flux were quantified with a sensitivity analysis.

Table of Contents

List of Tables

List of Figures

Chapter 1: Introduction and Background

This chapter introduces the CO_2 leakage problem and objectives of this dissertation. A brief introduction to geologic storage as a mitigation option is provided in the first section. The advantages, methods and risks of geologic storage are discussed in the subsequent section. CO_2 leakage and its consequences and potential leakage pathways are discussed in the third section. Fault leakage, natural analogues, typical fault properties and fluid behavior along faults are discussed in the fourth section. The final section includes the research objectives and the structure of this dissertation.

1.1 CARBON PROBLEM

Beginning with the industrial revolution in the 18th century, energy from fossil fuel sources has contributed significantly to the increase in the concentration of CO_2 in the atmosphere and oceans. Specifically, CO_2 concentrations have increased to nearly 400 ppm (Mauna Loa observatory) compared to the pre-industrial levels of 280 ppm and are expected to continue to increase at the rate of 2-3 ppm/year without mitigation (NOAA, 2015). The increase in concentrations of CO_2 and other Green House Gases (GHGs) (CO_2, CH_4, N_2O etc.,) is predicted to impact the global climate (Wigley et al., 1996). The latest climate model projections report an average temperature increase of 0.5 to 4 °C and an average sea level increase of 0.1 to 0.6m for different emission scenarios by the end of 21st century (IPCC, 2014).

Global effort has been undertaken with the announcement of Paris agreement to limit the average temperature rise to 2 °C and limit the CO_2 concentration to 450 ppm by the end of the 21st century (UNFCC 2015 a, b). The suggestions to mitigate the increase of CO_2 include (Leung et al., 2014),

1) Increase energy efficiency of industrial processes
2) Switch to less carbon-intensive fuels (coal to natural gas)
3) Increase capacity of biological sinks (afforestation, agriculture etc.)
4) Increase energy production from renewable (solar, wind, hydro, etc.) and nuclear sources
5) Addition of carbon capture and storage (CCS) capability to fossil-fuel based power sources and energy intensive industries

These options become effective at different time scales due to the technological advancements and economic factors (Leung et al., 2014). No single option is sufficient by itself and instead, these mitigation measures have to be implemented in an integrated manner. The first four suggestions provide a long-term strategy to reduce CO_2 whereas the CCS option provides a good near-term strategy (Stangeland and Baird, 2006). Total U.S. CO_2 emissions by the fossil-fuel based power-sector was around 38% of the total U.S. energy-related CO_2 emissions or 2043 million metric tons (2.04 GT) in 2014 (EIA, 2014). Until the renewable alternatives can be developed at competitive scale and prices, CCS offers a viable option to geologically store billions of tons of CO_2 per year.

1.2 CARBON CAPTURE AND STORAGE

Carbon Capture and Storage (CCS) involves the capture of CO_2 at point sources (e.g. fossil fuel based power plant) and its transportation, injection and storage in deep geological formations. In some sense, CCS is the process of returning carbon to where it was originally produced from, albeit in an altered form (RISCS, 2014). Typical CCS operations include a portfolio of technologies that involve capture, transport, storage and monitoring as shown in Figure 1.1.

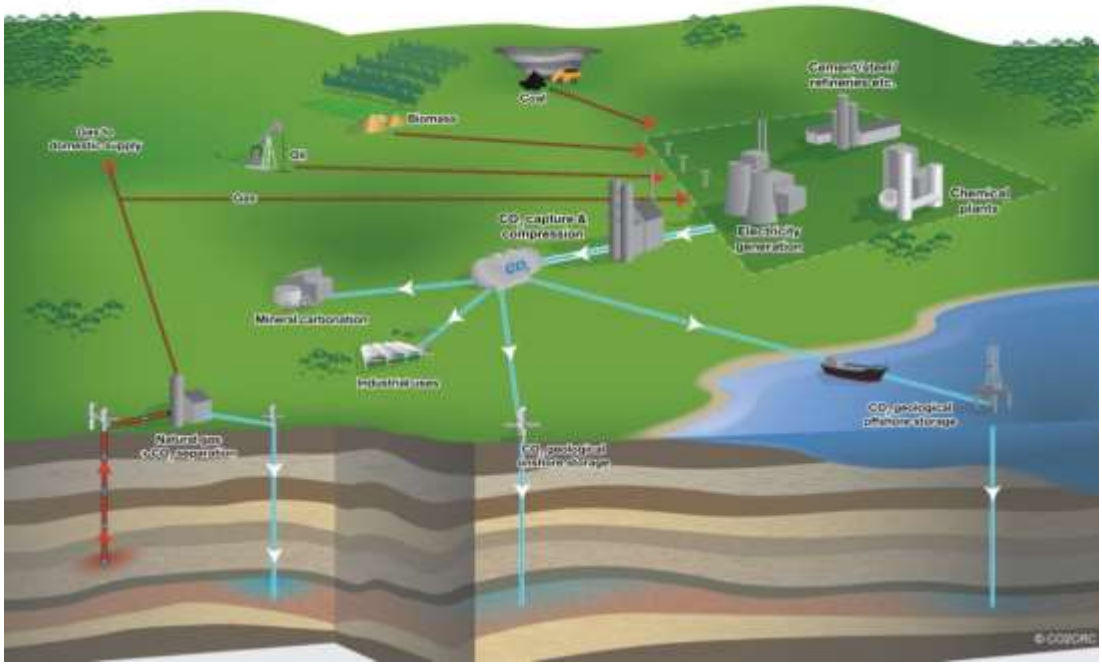

Figure 1.1: Typical CCS operations with a range of CO_2 sources and storage site options (Image courtesy: CO2CRC).

Nearly 75 large-scale projects which capture and store around 36 million tons of CO_2 per annum are currently in operation including projects such as Sleipner CO_2 injection (Baklid et al., 1996), Weyburn-Midale CO_2 project (Emberley et al., 2005), Boundary Dam project (Rostron et al., 2014), In Salah CO_2 injection (Mathieson et al., 2011) among several others (Leung et al., 2014). The expected storage capacity could increase up to 10000 $GtCO_2$ by the end of the current century (IEA, 2004). A global map of potential geological storage locations is shown in Figure 1.2.

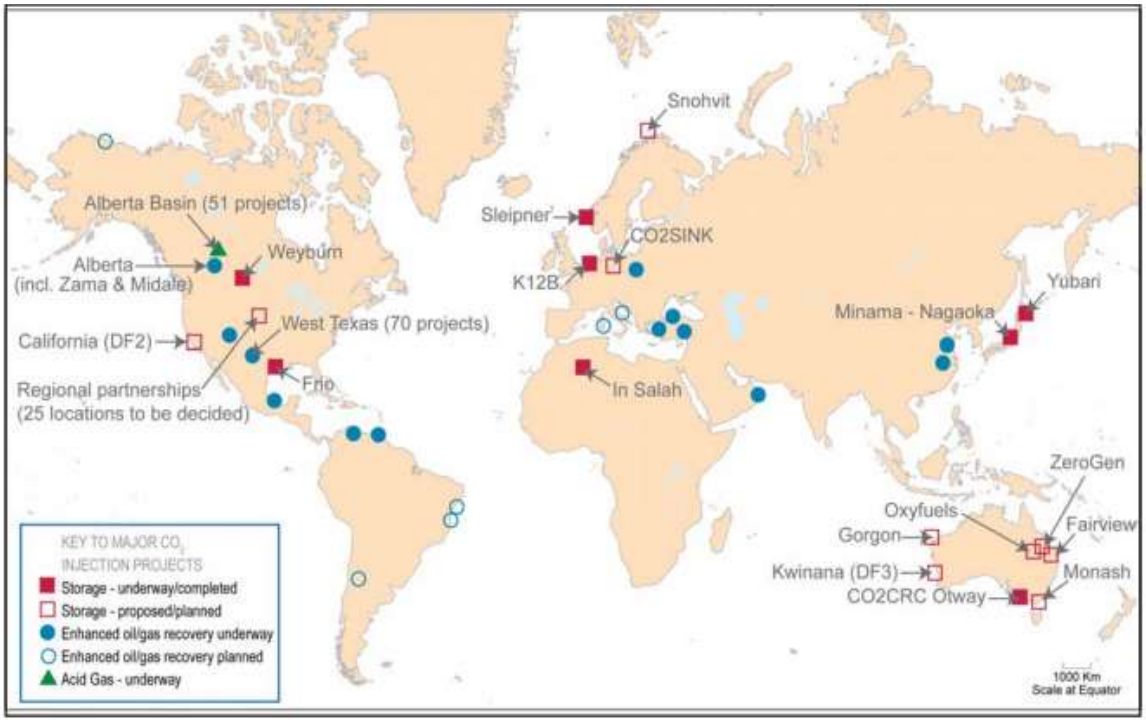

Figure 1.2: Global map of geological storage projects that are in operation or proposed (Image courtesy: CO2CRC).

1.2.1 Capture and Transportation

CO_2 has been captured from industrial sources such as fossil-fuel based power plants, cement production, steel production, hydrocarbon refineries etc. Capture processes that have been implemented include 1) pre-combustion (Jansen et al., 2015), 2) post-combustion (Wall, 2007) or during 3) oxyfuel combustion (Stanger et al., 2015). Mechanisms used to accomplish capture are 1) Physical and chemical absorption, 2) Adsorption, 3) Cryogenic distillation, 4) Membrane separation, 5) Gas hydrates and 6) Chemical looping among others (Abanades et al., 2015; Leung et al., 2014). The most common mechanism for capture is the use of amine solvents (Liang et al., 2015). The appropriate site-specific choice of CO_2 capture technology is based on the combustion

methods, fuel composition, the influence of water, the resulting partial pressure of the gas mixture, plant configuration and costs (Rao and Rubin, 2002).

The captured CO_2 is compressed and transported to the storage site by means of pipelines, ship or tankers. The means of transportation depends on whether the storage site is onshore or offshore. Transportation methods are chosen based on the amount of CO_2 transported and the distance. For large amounts and long distances, pipelines are preferred (Rubin et al., 2015). Captured CO_2 can also be used for enhanced oil recovery (EOR) (Blunt et al., 1993), used to produce methane from gas reservoirs and coalbeds (Mazzotti et al., 2009), used to generate geothermal energy (Brown, 2000; Randolph and Saar, 2011) or stored chemically by mineral carbonation (Seifritz, 1990).

1.2.2 Geological Storage

Characteristics of ideal formations for storage of CO_2 include thick formations with high porosity and high permeability with a caprock with excellent sealing integrity and a stable geologic environment (Bachu, 2000). Other factors that affect site selection are proximity to CO_2 sources, storage capacity, formation depth and a location where hazardous geological events such as earthquakes are not expected to occur over long time periods.

Sedimentary basins are good candidates for geological storage since they have porous and permeable rocks such as sandstones and carbonates for target reservoir and claystones or evaporites with a very low permeability and porosity for caprock seals (Gunter et al., 2004). The most commonly considered storage formations are depleted oil and gas fields (Stevens et al., 2001), deep saline aquifers (White et al., 2003) and unminable coal seams (Reeves, 2001; White et al., 2003). Alternative CO_2 storage

options include oil and gas shales (Busch et al., 2008), basalts (Matter et al., 2009) and salt caverns (Dusseault et al., 2004). Some examples of the storage and utilization options are shown in Figure 1.3. The expected storage capacity could increase up to 10,000 Gt CO_2 by the end of the current century (IEA, 2004). Commercial-scale experience in engineered storage of natural gas, acid gas and liquid waste provide confidence for secure CO_2 storage (Benson et al., 2006).

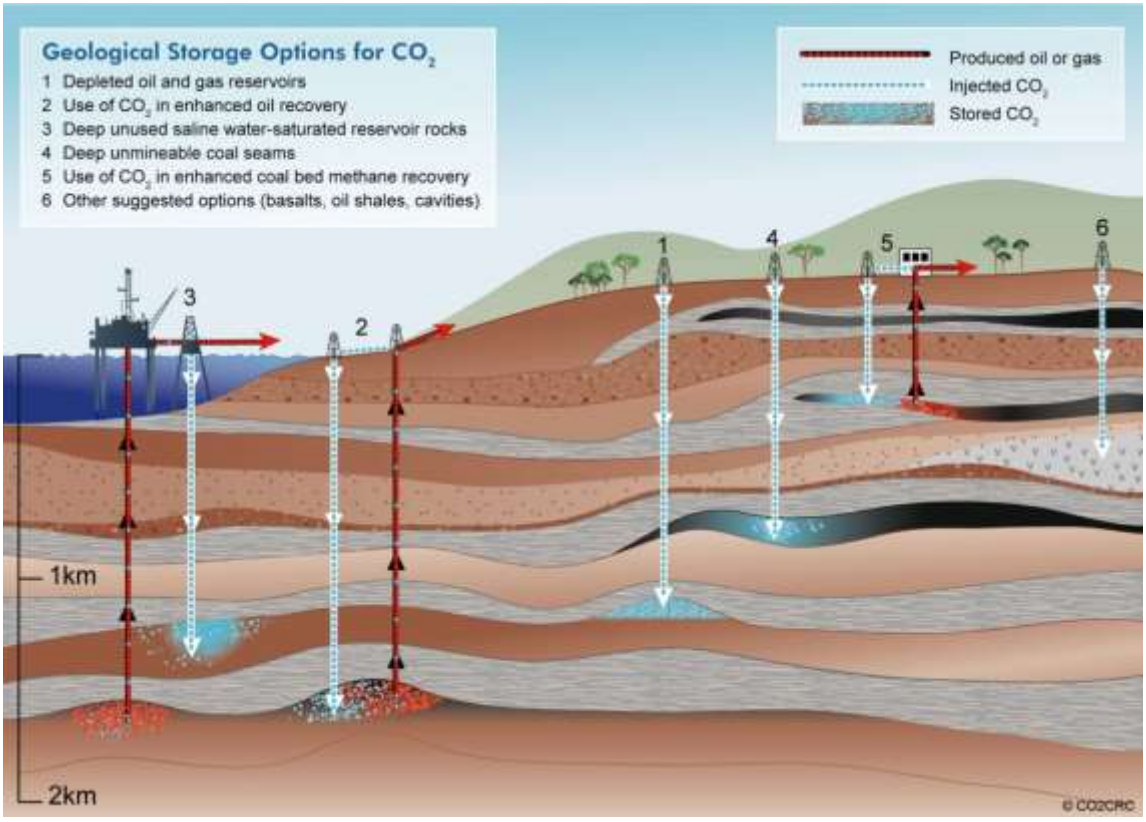

Figure 1.3: Geological storage options for CO_2 (Image courtesy: CO2CRC)

CO_2 is typically stored as a gas at pressures greater than 7.38 MPa and temperatures greater than 304.12 K (NIST, 2015). These so-called supercritical CO_2 conditions are common for storage reservoirs at depths greater than 800 m. The CO_2

density in the reservoir is greater by a factor of about 1000 compared to surface conditions (NIST, 2015).

Trapping mechanisms include the following:

1) Structural Trapping – Injected CO_2 is trapped below an impermeable confining layer by virtue of the structure/boundedness of the target formation.
2) Residual Trapping – CO_2 is trapped by capillary forces as an immobile gas in the pores of the rock.
3) Dissolution Trapping – CO_2 is dissolved in water.
4) Geochemical Trapping – CO_2 reacts with the rock to form a solid mineral. .
5) CO_2 is adsorbed on the organic matter.

The effectiveness of the different trapping mechanisms is shown in Figure 1.4. At early times, structural trapping will play a major role to retain the injected CO_2 (Gunter et al., 2004). At late times, CO_2 is retained by more secure trapping mechanisms such as geochemical and solubility trapping (Kumar et al, 2005). The dominant trapping mechanism will depend on the thickness, pore structure, rock type, mineral/organic matter content, and boundedness of the target formation (Leung et al., 2014). Rigorous site-selection procedures with a major emphasis on secure storage requirements is important to reduce the possibility of leakage (Pawar et al., 2015).

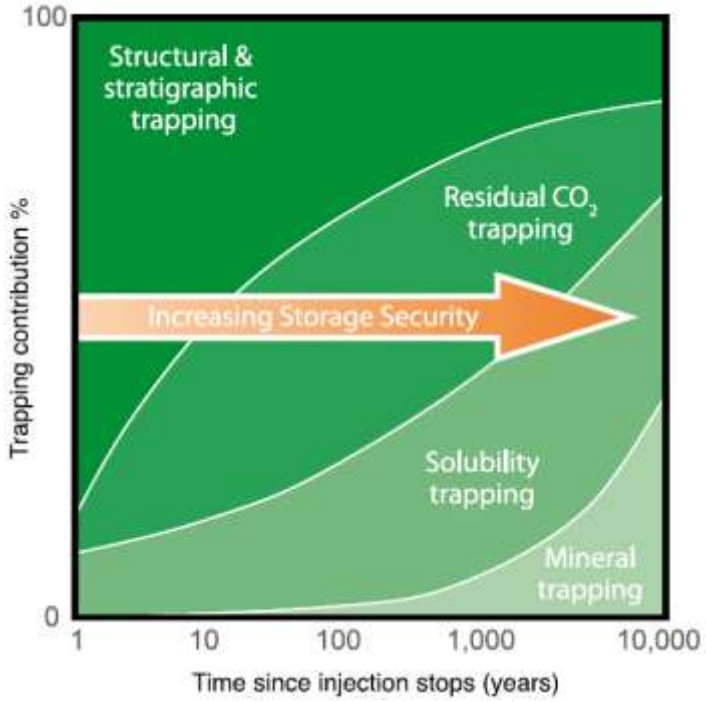

Figure 1.4: Contribution of different trapping mechanism towards storage security as a function of time (Benson et al., 2012).

1.2.3 Monitoring

Monitoring of a geologic CO_2 storage reservoirs is needed to detect possible leakage pathways or other deterioration of storage integrity (Wright et al., 2004). Monitoring will also be essential for initiation of remediation methods for CO_2 leakage in the event that leakage occurs. Variety of monitoring techniques have been developed to acquire data about the migration of CO_2 in the subsurface such as seismic monitoring (Chadwick et al., 2010), remote sensing (Ringrose et al., 2013), gravimetry (Alnes et al., 2011), well based monitoring (Freifeld et al., 2014), pressure (Sun et al., 2013), above zone monitoring interval (AZMI) (Bourne et al., 2014), temperature (Bielinski et al., 2008), geoelectric monitoring (Kiessling et al., 2010), geochemical sampling (Boreham et

al., 2011), atmospheric monitoring (Leuning et al., 2008), tracers (Myers et al., 2013), and soil gas monitoring (Romanak et al., 2012).

1.2.4 Challenges

There are several challenges related to the large-scale deployment of CCS including 1) Increases in the cost of energy production by up to 40% and fuel costs by up to 25% for new power plants with integrated capture and sequestration of CO_2 and energy production costs will increase up to 90% to retrofit old power plants (Rubin et al., 2015), 2) No legal/regulatory framework to reward carbon reduction technologies and/or penalties for carbon emitting sources (Dixon et al., 2015), 3) Demonstration of storage security in geological formations on a large scale. These challenges have to be overcome for CCS to become a viable option for climate mitigation.

1.3 LEAKAGE

The viability of CCS depends on the secure long-term containment of stored CO_2. The biggest risk associated with geological storage is the possibility of leakage. In CCS context, leakage refers to any injected CO_2 that migrates away from the initially intended storage formation. A storage project will be considered successful if more than 99% of the injected CO_2 is stored in the intended formation for more than 100 years (IPCC, 2005).

1.3.1 Leakage Consequences

Potentially detrimental consequences of leakage on the environment and human health have been broadly divided into 5 categories (Benson, 2006),

1) Potential hazards to humans - Worst of the potential leakage scenarios involve a direct release to the atmosphere. Elevated CO_2 concentrations close to surface release zone lead to increased risk to people living in the vicinity. The magnitude of the consequences depend on the CO_2 concentration (Benson et al., 2002):
   i) <1% - Less adverse long term health effects, possible short-term health effects
   ii) >2% - strong effect on respiratory physiology and
   iii) >5% - causes unconsciousness and death
2) Contamination of groundwater – Leaked CO_2 dissolves in the groundwater to form carbonic acid with a low pH that could result in toxic metals migrating to shallow groundwater and detrimentally affect its use for drinking and agricultural (Jaffe and Wang, 2003).
3) Impact on ecosystems - Increase in concentration of CO_2 in the subsurface will affect microbial habitat. This will help microbes that prefer CO_2 and be detrimental to other microbes and hence alter the microbial environment (Jimenez and Chalaturnyk, 2003). Leakage also affects the fauna near the surface. The CO_2-laced soil gas is a phytotoxic and alters the vegetation at the surface (RISCS, 2014).
4) Induced seismicity – Storage of CO_2 at pressures substantially higher than formation pressure can induce fracturing and movement along faults (Streit and Hillis, 2004). Fault reactivation can induce earthquakes large enough to cause

damage and provide a leakage pathway towards subsurface to impact the groundwater, fauna and humans near surface.

5) Potential hazards of flue gas – Leakage of flue gases containing SO_X and NO_X would have much more detrimental consequences to the atmosphere than leakage of pure CO_2 (West et al., 2005).

1.3.2 Potential Leakage Pathways

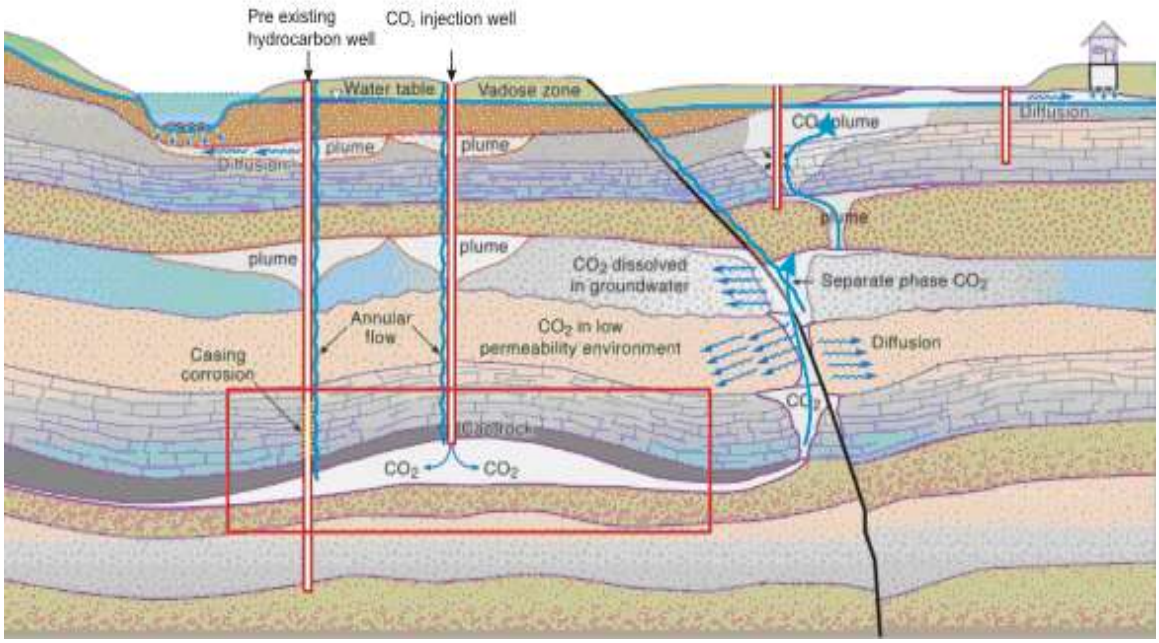

Figure 1.5: Geological representation of leakage pathways (Benson, 2006)

The leakage pathways enable CO_2 to migrate out of the intended storage formation through the subsurface towards the atmosphere as shown in Figure 1.5. Unless water is withdrawn, the pressure will increase in the storage reservoirs since CO_2 will be injected into formations that are saturated with water. This will act as a driving force for

leakage. CO_2 that is not trapped will migrate to the top of the storage formation with the cap rock acting as a seal. The ability of caprock to contain CO_2 migration will depend on several factors related to the integrity of the caprock such as continuity, permeability, faults/fractures, operational/abandoned wells etc. Once compromised, the presence of permeable pathways such as faults/fractures and leaky wells will allow the CO_2 to migrate toward the surface.

Leakage through the caprock may occur for the following reasons (Jimenez and Chalaturnyk, 2003; Busch et al., 2010; Benson, 2006):

1) The pressure in the storage formation is higher than the capillary entry pressure of the caprock (Wollenweber et al., 2010).
2) Permeability of the caprock is not low enough to stop flow into the caprock.
3) Diffusion through the caprock (Krooss et al., 2003).
4) Discontinuities in the caprock such as fissures.
5) Leakage due to the lack of laterally extensive caprock.
6) Induced fractures in the caprock. Mechanical failure occurs when 1) the reservoir is over-pressured; 2) there are consistent pressure fluctuations during storage, and 3) prior production of hydrocarbons from the reservoirs and enhanced hydrocarbon recovery processes (Rutqvist, 2012).
7) Chemical reaction/interaction between the CO_2 and the caprock weaken the caprock and create a leakage pathway. The reaction rate will depend on the physical nature of the caprock (Wollenweber et al., 2010).
8) Seismic disturbances and tectonic activity may cause caprock failure (Mazzoldi et al., 2012).
9) Presence of unsealed or reactivated faults/fractures (Rutqvist et al., 2007)

10) Caprock is compromised by wellbore issues related to the injection wells, observation wells, improperly abandoned wells during prior injection or production operations and/or undocumented production/injection wells. The different modes of leakage initiation that could occur are shown in Figure 1.5. Leakage could occur along the casing-cement interface (a, b), through cement matrix permeability (c), via corrosion of the steel casing (d), through fractures in the cement, and along the cement-rock interface (e, f) (Gasda et al., 2004).

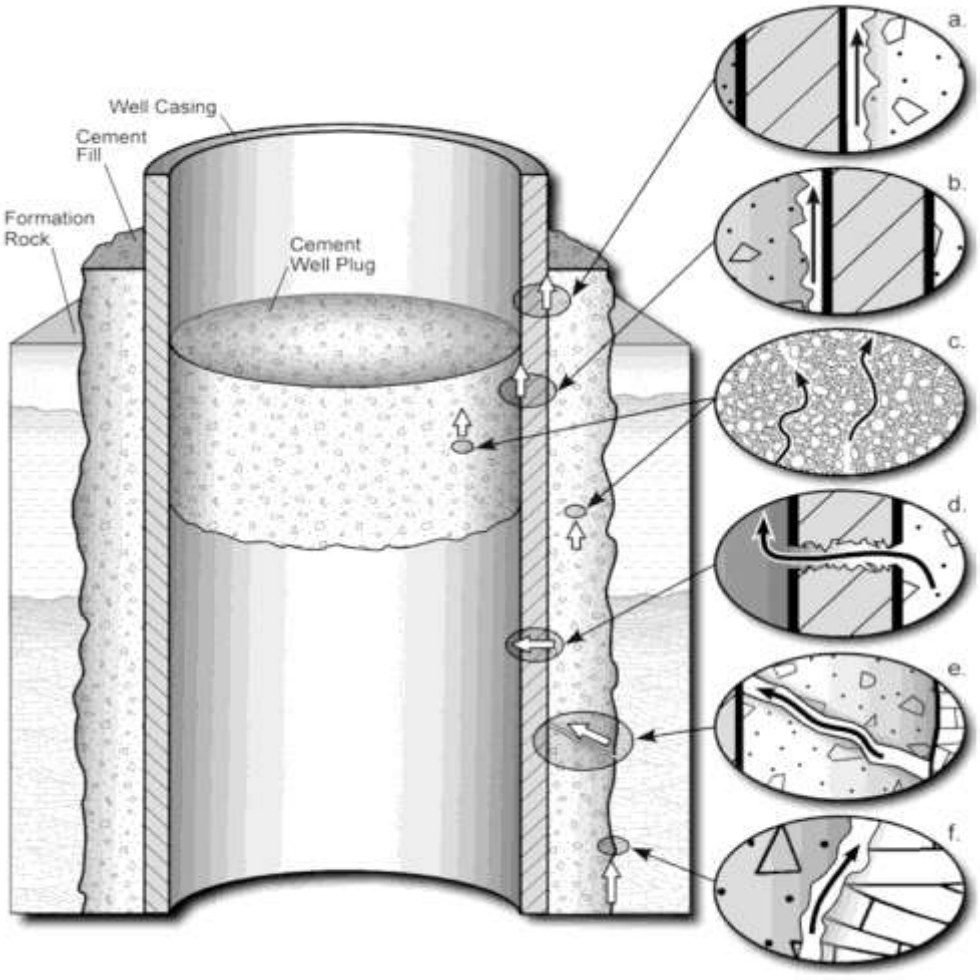

Figure 1.5: Wellbore leakage mechanisms (Gasda et al. 2004)

The leakage mass flux will depend on the geological characteristics of the leakage pathway and the fluid properties in the pathway. The risk of leakage is expected to be highest during the injection phase since the reservoir pressure is highest during injection (Pawar et al., 2015). The leakage likelihood through wellbore-based pathways is considered to be the highest, but the potential leakage mass fluxes are thought to be low and easily detected in most cases since these pathways should be mapped prior to storage (Pawar et al., 2015). Leakage through high permeability pathways such as faults/fractures is a major concern since the leakage mass fluxes could be high. The leakage likelihood through fault/fracture pathways is quite complex due to wide ranges of key characteristics such as fault permeability and aperture/effective width and the large technical uncertainty regarding the mechanism of leakage.

Concerns about leakage and the possible environmental impacts provide motivation to quantify leakage risk with better estimation of leakage mass flux, variation of leakage mass flux and duration and the amount of leakage. Quantifying leakage risks depends on modeling the evolution of leakage taking into account various factors such as the properties of the subsurface rocks along the leakage pathway, the pressure, temperature, fluid saturations, fluid properties, etc.

1.4 FAULT LEAKAGE

Fault and fracture zones present a leakage pathway for CO_2. Leakage will depend on the fault dimensions, stress regimes, fault juxtaposition and the host rock lithology (Fisher and Knipe, 1998; Caine et al., 1996). Presence of clay smear or gouge materials and juxtaposition of low permeability rocks will inhibit flow. Open/unsealed/transmissive and reactivated fault/fracture networks may be key leakage pathways. Reactivations

occur due to the increase in pressure that affect the stress conditions or could be caused by chemical reaction between CO_2 and fault zone rocks (Rinaldi et al., 2014).

1.4.1 Natural Analogues of CO_2 Leakage through Faults/Fractures

The review of natural analogues of leakage through faults/fractures is shown in Table 1.1 (Lewicki et al., 2007). Natural analogues provide a basis for possible leakage mass fluxes from fault zones and mechanisms of leakage. The source for the leaked CO_2 was from natural accumulations. The accumulated CO_2 was most commonly from thermal decomposition of carbonate-rich sedimentary rocks and/or degassing of magma bodies at depth. CO_2 from these sources accumulated in permeable formations (e.g. sandstones and fracture limestones) under low permeability cap rocks (e.g. shale and siltstone).

Faults were found to be the primary leakage pathway once the accumulated CO_2 moved away from the storage reservoirs. The leakage mechanism for the mammoth mountain case is shown in Figure 1.6 (Sorey et al., 1998). The leakage rates/fluxes for these analogues were quantified from soil flux data and measurements of atmospheric and vent gas CO_2 fluxes. The leaked CO_2 released at the surface as diffuse gas emissions over large land areas, focused vent emissions, eruptive emissions and degassed through surface water bodies and spring discharges. CO_2 leakage from marine vents (> 600m depth) such as Okinawa trough (Sakai et al., 1990; Konno et al., 2006), Mariana arc (Lupton et al., 2006, 2008) showed that the temperature at the sea floor was low enough for liquid CO_2 and CO_2-hydrates to form.

These fluxes must be used with caution since they were measured at the surface as opposed to a direct measurement from the specific faults. These measurements also

disregarded potential losses between the CO_2 reservoir and surface such as dissolution in shallow aquifer brines, transport to locations not covered in the surface flux measurements etc. Hence, they are most likely to represent the low end of the expected leakage. The reported along fault permeabilities for natural analogues ranged between 0.1 mD to 1000 mD (IEAGHG, 2016).

Table 1.1: CO_2 leakage mass flux from natural analogues

Site	**Leakage pathway**	**Measurement method**	**Flux ($kg/s/m^2$)**	**Reference**
Latera, Tuscany	Fault and fracture	Soil flux data	1.25×10^{-3}	(Pearce et al., 2002)
Paradox Basin, USA	Fault and fractures	Atmospheric CO_2 concentration and fluxes	4.05×10^{-4}	(Jung et al., 2015)
Albani hills, Italy	Fault and fractures	Soil flux data	3.67×10^{-4}	(Lewicki et al., 2007)
Matraderecske, Hungary	Fault and fractures	Soil flux data	2.03×10^{-4}	(Pearce et al., 2002)
Mammoth mountain, USA	Fault and fractures	Atmospheric CO_2 concentration and fluxes	1.15×10^{-4}	(Lewicki et al., 2007)
Solfatara, Italy	Fault and fractures	Soil flux data	5.78×10^{-5}	(Lewicki et al., 2007)

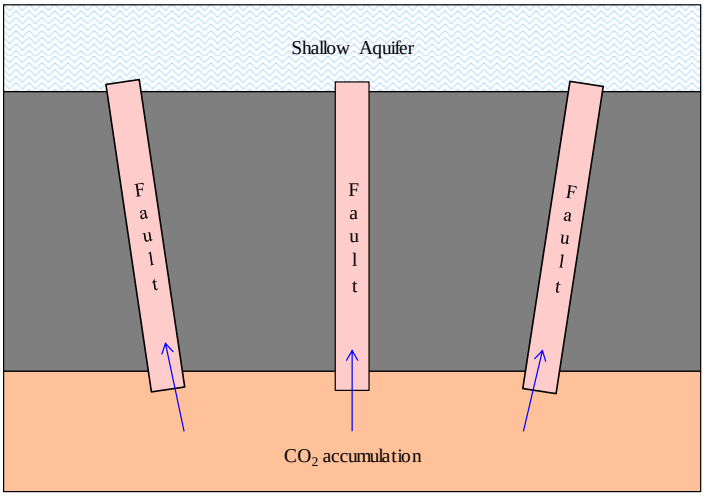

Figure 1.6: Mechanism for fault leakage at Mammoth Mountain (Sorey et al. 1998)

1.4.2 Fault Structure and Permeability

The critical control of leakage through faults/fractures was the permeability, width, structure and extent of the fault zone. The typical fault zone as shown in Figure 1.7a has 3 substructures namely 1) single or multiple fault cores where the displacement has occurred, 2) a fracture damage zone with the fracture density highest closest to the core 3) the unfaulted/unfractured host rock (protolith) (Rinaldi et al., 2014; Cappa and Rutqvist, 2011; Caine et al., 1996; Faulkner et al., 2010).

Faults in low porosity rocks generally have a fine-grained fault core surrounded by a fracture dominated damage zone. Conversely, in coarser grained high porosity rocks, the damage zone tends to be comprised of low porosity deformation bands whilst the core maintains a higher permeability slip surface (Caine et al., 1996; Faulkner et al, 2010). The density of the micro-fractures in the damage zone was highest close to the fault rock and decreased away from it. The characteristics of the host rock, fault deformation characteristics and the rock lithology varied with depth (Seebeck et al., 2014).

Fault zone structure depends on the depth of formation, lithology, tectonic environment (extensional, compressional etc.), throw (magnitude of displacement) and fluid flow (Faulkner et al., 2010). The width of the damage zone may be estimated from the length of faults, since the displacement of faults scaled with their length for various subsurface strata (Seebeck et al., 2014; Childs et al., 2009; Faulkner et al., 2010). The maximum fracture density occurs at fault zone thickness between 0 to 0.5m (Childs et al., 2009).

The permeability of the fault zone will depend on the rock deformation products such as fault gouge, fractures, clay smears etc. and the interconnectedness of the fracture network (Fisher and Knipe, 1998; Caine et al., 1996; Seebeck et al., 2014). Regions of

high fracture densities are most likely to contain long fractures and/or interconnected fracture networks that enhance vertical hydraulic conductivity (Seebeck et al., 2014). The damage zone may also contain subsidiary faults, veins, joints, folds, fault relays, bends and tips among other features that enhance vertical conductivity (Rinaldi et al., 2014; IEAGHG, 2016). The permeability along the fault zone can be as high as 100 D (Ingebritsen and Manning, 2010).

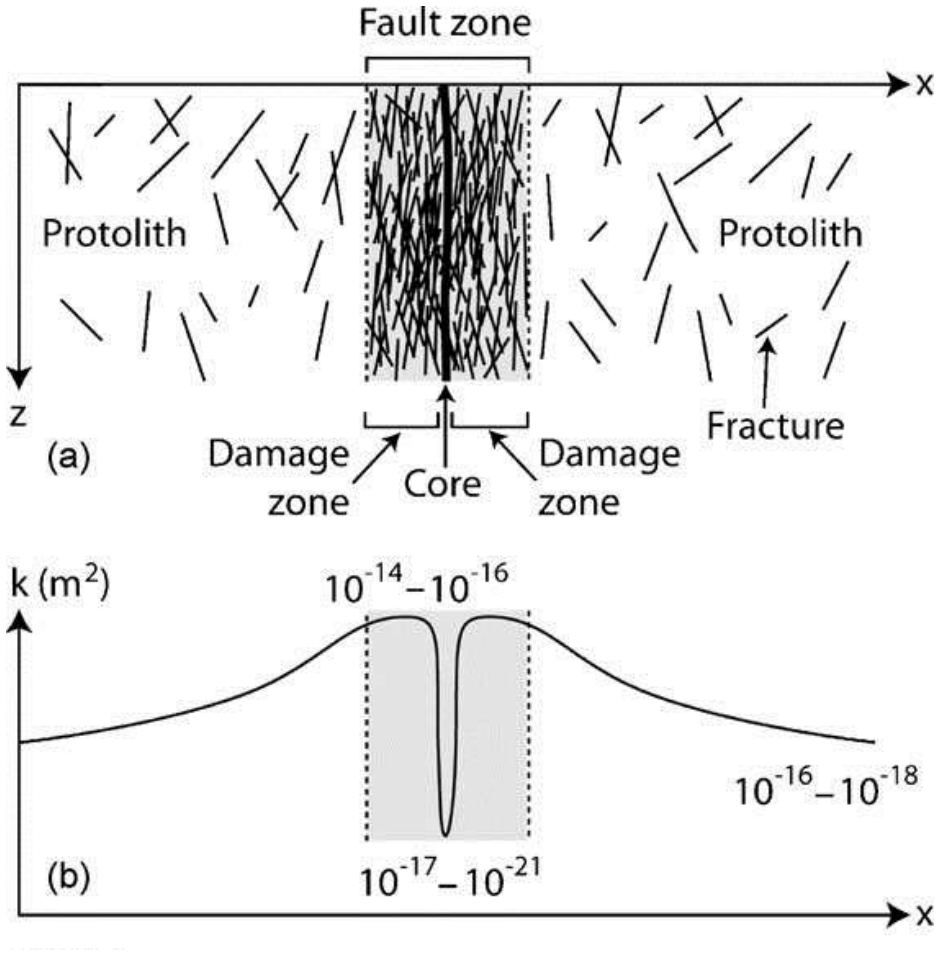

Figure 1.7: a) Typical fault zone structure with three substructures namely fault core, damage zone and host rock (protolith). b) Typical permeability for the different substructures. The fault rock has very low permeability (Cappa and Rutqvist, 2011).

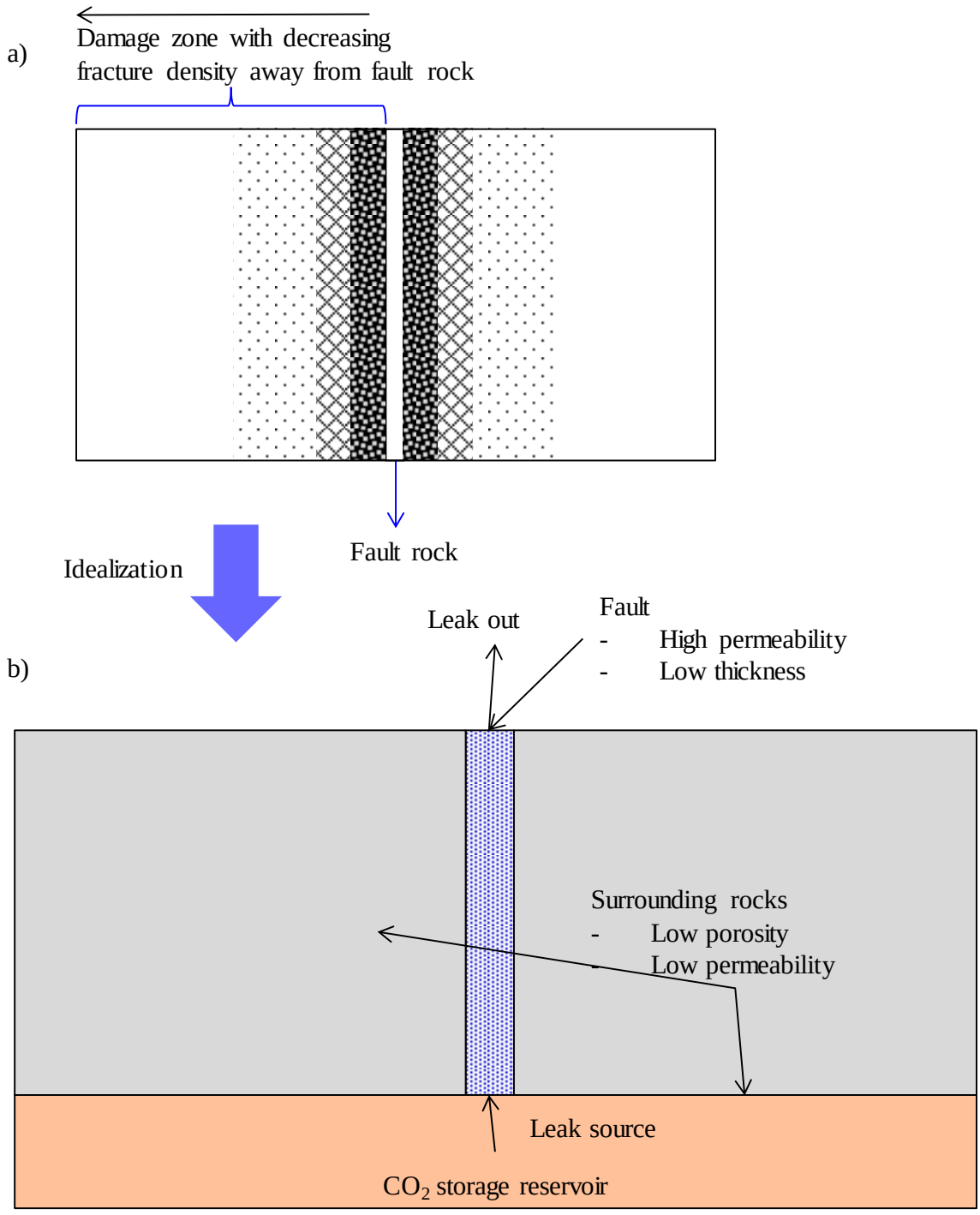

Figure 1.8: a) Representation of fault and damage zone b) Idealized representation of fault leakage model based on the fault zone approach.

Hence, there is always a huge uncertainty in the fault parameters such as fault length, fault displacement, fault width and fault permeability. The fault geometry will be complex with parameters such as width and permeability varying with depth. The idealized leakage pathway representation shown in Figure 1.8 has been used to make systematic estimates of leakage mass flux (Pruess, 2003, 2007, 2008; Lu et al., 2012; Ramachandran et al., 2014, 2017). Henceforth, the fault zone will be addressed as fault and the fault width will be addressed as fault effective width. Since there is always a huge uncertainty in the fault parameters, the estimates of leakage mass flux are considered relative values and not absolute predictions.

1.4.3 Fluid Behavior during CO_2 Migration along Faults

This section is a review of the fate of CO_2 after it leaks from the storage formation. Not all of the leaked CO_2 will reach the surface. Some of it is attenuated into intersecting permeable layers/secondary traps encountered during upward migration (Chang et al, 2008). The extent of migration is restricted by the geological characteristics and the structural nature of the fault. The leakage mass flux depends on the fluid properties such as density and viscosity of the leaked CO_2. The interactions between water and CO_2 and the phase behavior of CO_2 have been found to be very important factors affecting the estimates of the leakage mass flux (Pruess, 2003, 2007, 2008).

Understanding the pressure and temperature conditions that occur during leakage is important since CO_2 can exist in multiple phases (gas, liquid and hydrate.). The temperature and pressure profile of a vertical fault at hydrostatic (0.433 psi/ft) and an assumed geothermal gradient of 0.03 K/m is shown on a CO_2 phase diagram in Figure 1.9. Pressure and temperature decrease from the leakage source to the surface. At low

pressures (< 1070 psi) and temperatures (< 303 K), CO_2 will exist in either a liquid or gas phase. At lower P-T (647 psi & 283K) CO_2 hydrates will form (as shown by the red curve) if adequate amounts of water are present. The key observation from Figure 1.9 is that CO_2 can exist in different phases during leakage. Since the pressure and temperature decrease continuously, there will be substantial variations in CO_2 properties such as density and viscosity as shown in Figure 1.10.

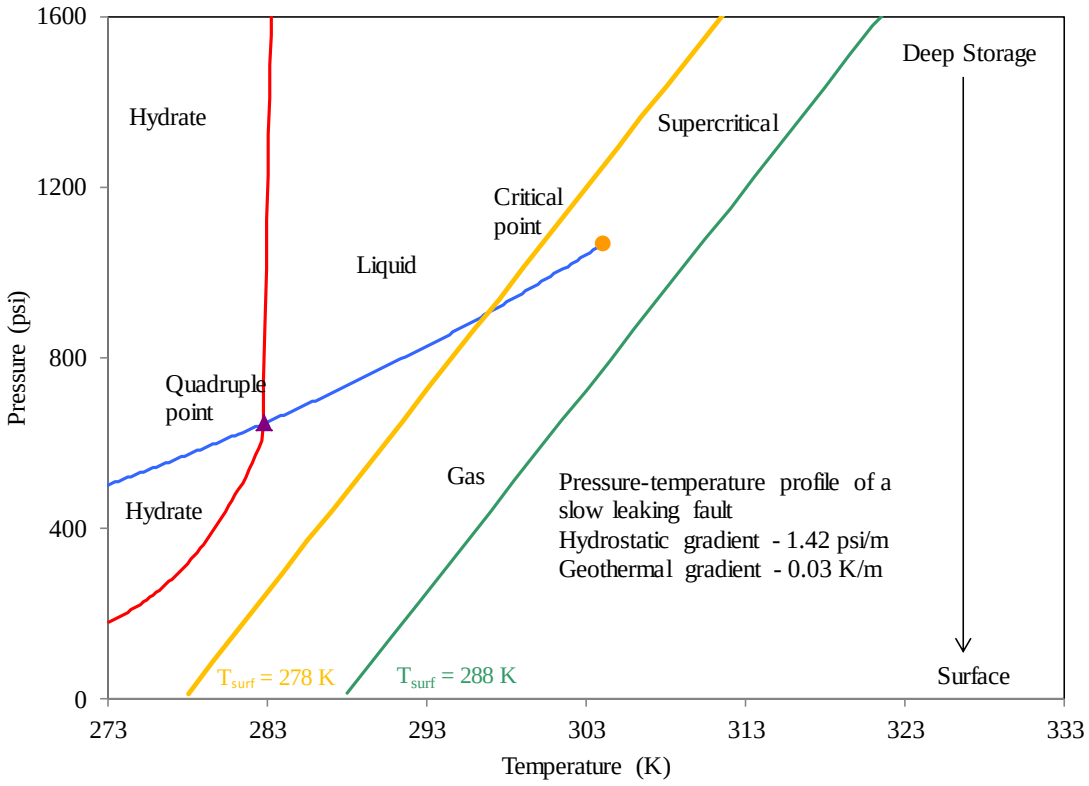

Figure 1.9: Liquid and gas phases will coexist if the pressure and temperature are on the blue saturation curve. The hydrate forming conditions for CO_2-H_2O mixtures is shown by the red curve. Q is the quadruple point for the CO_2-water mixture where four phases coexist: liquid CO_2, liquid water, gas and hydrate phases coexist. The green and yellow lines show the pressure-temperature profile along a slow leaking fault corresponding to two different surface temperatures of 288K and 278K, respectively.

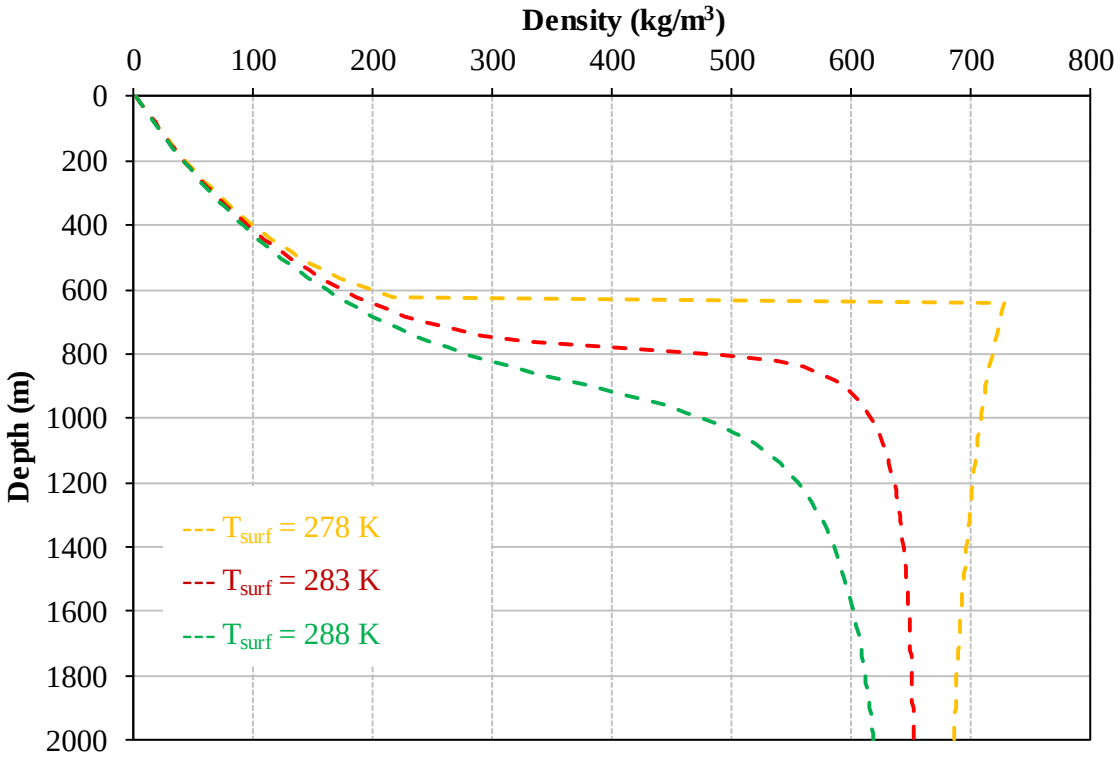

Figure 1.10: Density of CO_2 as a function of depth corresponding to three different surface temperatures. The pressure was given by the hydrostatic gradient and the temperature by the geothermal gradient. Density exhibits non-linear behavior during leakage.

At pressures below 647 psi and temperatures below 283 K, CO_2 hydrates can form. Gas-hydrates are ice-like solid particles that form at specific temperature and pressure conditions, in a reaction between the host water molecules and gas molecules (Pedersen and Christensen, 2007). CO_2 readily forms hydrates at conditions at or below the red curve shown in Figure 1.9. The reaction for CO_2 hydrate formation is

$$CO_2 + nH_2O \rightarrow CO_2 \bullet nH_2O \tag{1.1}$$

where n is the hydration number (average moles of water required to cage one molecule of CO_2). CO_2 hydrate formation requires a ratio of 5.75 moles of water to 1 mole of CO_2

for full cage occupancy (Uchida et al., 1995). Typically, the hydration number varies between 6-8 moles of water to 1 mole of CO_2 (Uchida, 1998). Hydrates will precipitate when CO_2 migrates upwards and reaches hydrate forming conditions. Hydrates will reduce the permeability of the fault and partially block the upward flow. Stability of the formed hydrates depends on factors such as (IEA, 2008):

1) The pressure and temperature conditions
2) Availability of adequate amount of water to cage the molecules
3) Availability of adequate amount of CO_2
4) Salinity and impurities in water that adversely affect the hydrate forming conditions

Inherently, all the factors mentioned above are strongly coupled. This coupled nature can be understood by looking at a CO_2 pressure-enthalpy diagram as shown in Figure 1.11. The blue curve is the gas-liquid coexistence boundary. CO_2 exists as gas and liquid inside this region and as a single phase everywhere else. At pressures below 647 psi in the presence of water, hydrates will form as shown in the light blue region. The enthalpy path along a 1000 m long vertical fault with a surface temperature of 283 K is shown as the red curve. The pressure is given by the hydrostatic gradient and the temperature by the geothermal gradient.

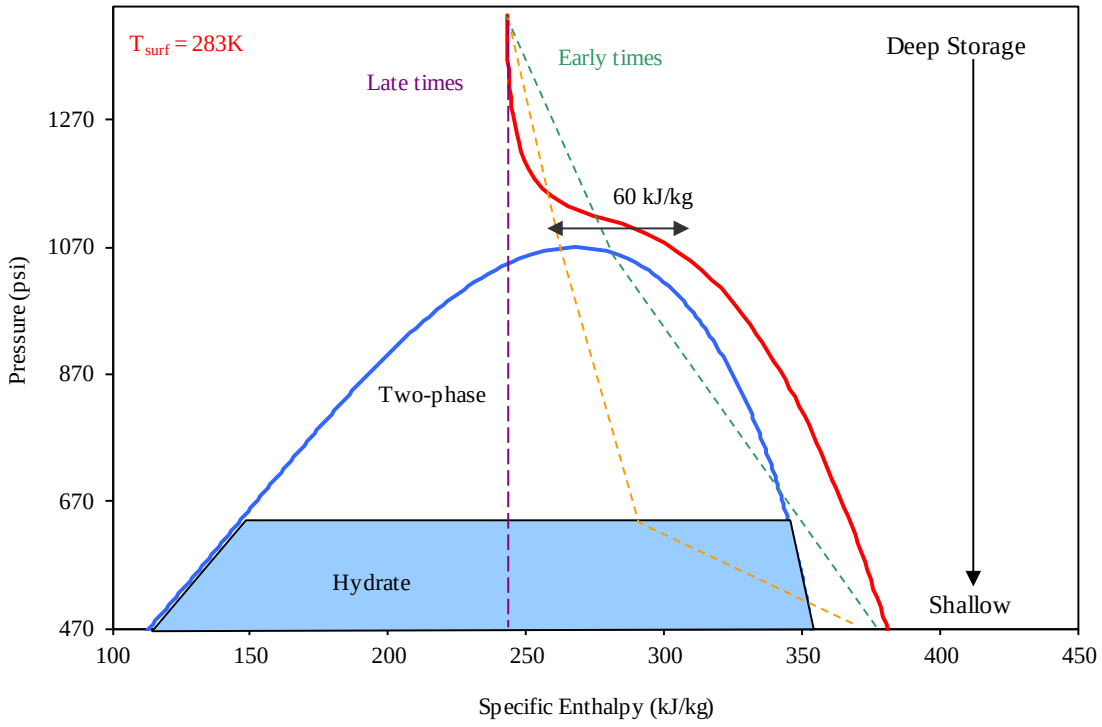

Figure 1.11: Pressure-Enthalpy diagram of CO_2 was shown here. The pressure-enthalpy profile of a slow leaking fault corresponding to a surface temperature of 283K is shown by the red curve. The CO_2 leakage source pressure is given by the hydrostatic pressure at the source depth of 1000 m. Some of the leaked CO_2 condenses to form a liquid phase at early time as shown by the green curve. With time, the two-phase region increases in size and hydrates formed at low pressures to form a three phase region of gas, liquid and hydrate as shown by the yellow curve. At late times, leakage reaches constant enthalpy flow as shown by the purple line.

The increase in enthalpy along the leakage path is due to the heat gain from the surroundings (geological formations). Heat gain was a function of the thermal conductivity of the surrounding rocks. At pressures and depths close to the CO_2 critical point, an increase in enthalpy of 60 kJ per kilogram of CO_2 was needed to remain along this profile. This value is specific to this case and may increase or decrease based on the initial conditions of the fault. Because of low thermal conductivity, the rock surroundings

will not be able to provide this energy continuously. This will result in only a moderate increase in enthalpy along with a strong cooling of leaked CO_2 in this region.

At early times, the enthalpy in the fault will follow the profile shown by the green line where CO_2 will be at saturation conditions (gas-liquid) for a portion of the fault. Some of the CO_2 will condense to form liquid CO_2. Gas and liquid phases will coexist which will result in multiphase flow over a portion of the fault (Pruess, 2003, 2007, 2008). The two-phase region of gas and liquid CO_2 will grow with time. Condensation of the CO_2 will affect the relative permeability of the gas and consequently decrease the leakage mass flux. The decrease in flux will result in additional time for the CO_2 to undergo thermal interaction with the surroundings. Heat from the warmer part of the surrounding rock will evaporate the liquid. This cycling between condensation and evaporation will go on until the rock in the immediate vicinity of the fault cools and ultimately reach a steady state at late times as shown by the purple line. At this stage, the leakage profile becomes isenthalpic. These conditions will strongly depend on the characteristics of the leakage pathway and the properties of the surrounding rock and may take a long time (of the order of 10,000 years) to reach. Along this isenthalpic path, CO_2 will cool enough for hydrates to form. Hence, any estimate of the leakage mass flux must take these phase changes into account.

In the leakage quantification context, the leakage analysis models need to consider non-isothermal conditions and they need to incorporate a phase behavior model that can identify phase changes between liquid, gas and hydrates. The Span-Wagner multi-parameter technical equation of state was used to compute the thermodynamic properties of each fluid phase (Span and Wagner, 2003). This EOS was a reduced form (12 parameters) of Span-Wagner EOS for CO_2 (56 parameters) used in the NIST database (NIST, 2015). Although computationally intensive, this EOS was the most accurate in all

fluid regions encountered in this study (Böttcher et al, 2012). The hydrate saturation is calculated using the Van der Waals-Platteeuw method available in PVTSIM software (Pedersen, 2014). It is assumed that all the water available is converted to hydrates when the pressure-temperature condition for hydrate formation is attained. This is a reasonable assumption for low water saturations. The purpose of this estimation will be to find the impact of non-isothermal nature and multiphase coexistence on leakage mass flux and gain insight into the effect of different parameters.

The mobility of the flowing phases during condensing/evaporating flow is expressed with relative permeability functions. The specific flow encountered in the leakage problem is complex because of phase changes. Similar flows were observed at geothermal reservoirs and magma hydrothermal systems. The suggested approach was to use conventional Corey-type curves to describe relative permeability with less phase interference effects (Ingebritsen et al., 2010).

1.5 DISSERTATION OBJECTIVE

The main objective of this dissertation was to develop models to estimate the leakage mass flux through faults/fractures from CO_2 storage formations. The models help estimate leakage mass flux, variations in the flux, leakage volumes and leakage duration. This problem is inherently complex because many factors influence leakage. The major factors are

1) The volume and pressure of the CO_2 source have a strong impact on the magnitude of leakage mass flux.
2) Geometry of pathways –Pathways characteristics such length, width, straight, angled or tortuous affect the leakage mass flux.

3) Flow properties of pathways – Permeability (homogenous, heterogeneous or engineered materials), porosity of pathways and initial saturations in the pathways.
4) Pressure and temperature gradients – Pressure and temperature continuously decrease from storage formation to surface. This will affect fluid properties such as density, viscosity of the fluid during leakage and introduce possibilities of multiphase coexistence.
5) Thermodynamic nature of leakage – Decompressive nature of leakage will result in phase changes such as condensation of vapor CO_2, evaporation of liquid CO_2 and formation of hydrates if adequate water is present. The salinity of the water present will affect this phase behavior.

The different factors that influence leakage are strongly coupled as discussed in the previous section.

A simplified steady-state flow model was developed to estimate the leakage mass flux taking CO_2 phase changes into account. This model will be a useful tool to estimate the leakage mass flux ranges prior to performing full-physics simulation and perform risk assessment at site selection stage. Numerical results of the leakage mass flux as a function of time will be useful to identify governing mechanisms for various leakage pathway scenarios. A numerical model with coupled mass and energy balances was developed and used to estimate the flux. This model integrated a phase behavior module that is capable of identifying CO_2 phase changes between gas, liquid and hydrates.

The mass flux estimates illustrated in this dissertation should be considered as relative values based on the idealized assumptions and approximations rather than predictions of actual values. The purpose was to determine the impact of phase changes and the fault properties on the leakage mass flux and to gain insight into the effect of

different parameters. The geometry and properties of an actual fault will be much more complex than assumed in these simple models. Some of the advantages to perform leakage quantification are

1) Quantify the governing leakage mechanisms (single-phase/multiphase flow) for different injection conditions and leakage pathway properties,
2) Estimate potential leakage mass flux, leakage duration, leakage amount ranges for specific storage formations that help determine the suitability of sites, evaluate potential liabilities/costs and design monitoring strategies,
3) Develop effective and rapid monitoring techniques based on estimated leakage mass fluxes and observations made on important parameters such as pressure and temperature,
4) Design remediation strategies for different leakage scenarios based on estimated leakage volumes.

1.6 LIST OF CHAPTERS

Chapter 1 introduces the CO_2 leakage problem and objectives of this dissertation. A brief introduction to geologic storage as a mitigation option is provided in the first section. The advantages, methods and risks of geologic storage are discussed in the subsequent section. CO_2 leakage and its consequences and potential leakage pathways are discussed in the third section. Fault leakage, natural analogues, typical fault properties and fluid behavior along faults are discussed in the fourth section. The final section includes the research objectives and the structure of this dissertation.

Chapter 2 describes the numerical model developed for dynamic leakage analysis starting with a brief introduction to the specific requirements for the numerical model.

The second section is a description of the mathematical model including the conservation equations, constitutive relations and the initial and boundary conditions. The phase behavior, fluid properties and the equation of state used in the model are discussed in the third section. The fourth section includes the numerical formulation of the finite difference representations of the flow equations and the formulation of the sequential solution of the non-linear equations. The final section includes a comparison of numerical results with analytical solutions and results using a commercial simulator.

Chapter 3 presents the results obtained from the numerical simulation of leakage through faults/fractures. A brief introduction about the numerical modeling of leakage is presented in the first section. An example result for a typical fault leakage scenario is discussed next. The coupled nature of thermal and multiphase flow aspects will be investigated in this discussion. The factors affecting these phase changes were identified with the help of a sensitivity analysis on permeability, effective width, and overpressure in the final part of this chapter.

Chapter 4 presents the results obtained from the steady-state flow model based on constant flowing total enthalpy. The modelling approach, transport equations and solution methods used are discussed. The model is used to analyze various leakage scenarios. The effect of factors such as reservoir pressure and temperature, depth and permeability that affect the multiphase coexistence, hydrate formation and leakage mass flux in general are quantified with a sensitivity analysis.

Chapters 5 presents a summary and the conclusions of this research as well as suggestions for future research.

Chapter 2: Numerical Model Description

Chapter 2 describes the numerical model developed for dynamic leakage analysis starting with a brief introduction to the specific requirements for the numerical model. The second section is a description of the mathematical model including the conservation equations, constitutive relations and the initial and boundary conditions. The phase behavior, fluid properties and the equation of state used in the model are discussed in the third section. The fourth section includes the numerical formulation of the finite difference representations of the flow equations and the formulation of the sequential solution of the non-linear equations. The final section includes a comparison of numerical results with analytical solutions and results using a commercial simulator.

2.1 INTRODUCTION

The idealized leakage model and its special characteristics are described here. A homogeneous, thin and long (~1000 m) vertical fault with no mass flux across lateral boundaries is assumed. The fault is assumed to be an equivalent porous medium with specific geometry (width, breadth), rock properties (porosity, permeability) and rock-fluid properties (relative permeability, initial saturations). The aqueous phase is assumed to be immobile (at residual saturation). CO_2 is assumed to migrate through the fault from storage reservoir conditions at the base of the fault towards the surface at atmospheric pressure and surface temperature conditions. The flow can be divided into 5 key regions as shown in Figure 2.1.

The balance between the convective energy flux in the fault and the conductive heat flux to the surroundings control the occurrence and extent of the above mentioned

multiphase coexistence regions besides fault properties such as permeability and effective width. The requirements for the numerical model to capture these characteristics include

1) Fluid properties – Because of variations in temperature and pressure along the fault, the phase behavior changes in a complex way. The changes in fluid properties such as density, viscosity, etc., must be taken into account. Hence, the fluid properties must be implemented as functions of the intensive variables. The Span-Wagner multi-parameter technical equation of state was employed to compute the thermodynamic properties of each fluid (Span and Wagner, 2003).
2) Heat exchange – Heat exchange between the fault and the surroundings is modelled. Vinsome and Westerveld heat-loss function was used to compute the heat losses through lateral boundaries (Vinsome and Westerveld, 1980).
3) Phase fluxes – The fluxes are another crucial aspect of the model. The fault is assumed to be an equivalent porous medium with small Reynolds number flow. Darcy's law was used as simplified momentum balance to estimate phase fluxes.
4) Phase appearance and disappearance – A major difficulty with the model was the existence of several regions with multiple phases present. Depending on the number of phases present, the primary variables change in the regions. A strong coupling with phase behavior and mass, momentum and energy balance is required to ensure the correct intensive variables are estimated. Pressure – total internal energy based numerical formulation as opposed to the conventional P-T formulation was used to overcome this issue.

The issues discussed above have been faced in geothermal reservoir modeling and hydrothermal systems modeling. Specifically, the mathematical model used in this research was based on the equations derived in geothermal research and hydrothermal research (Faust and Mercer, 1979 a, b; Hyaba and Ingebritsen, 1994a; Faust and Mercer,

1976, 1977a, 1977b; Mercer and Faust, 1975, 1979; Mercer et al., 1982; Hyaba and Ingebritsen, 1994b; Ingebritsen et al., 2010; Ingebritsen and Rojstaczer, 1996; and Kipp et al., 2008).

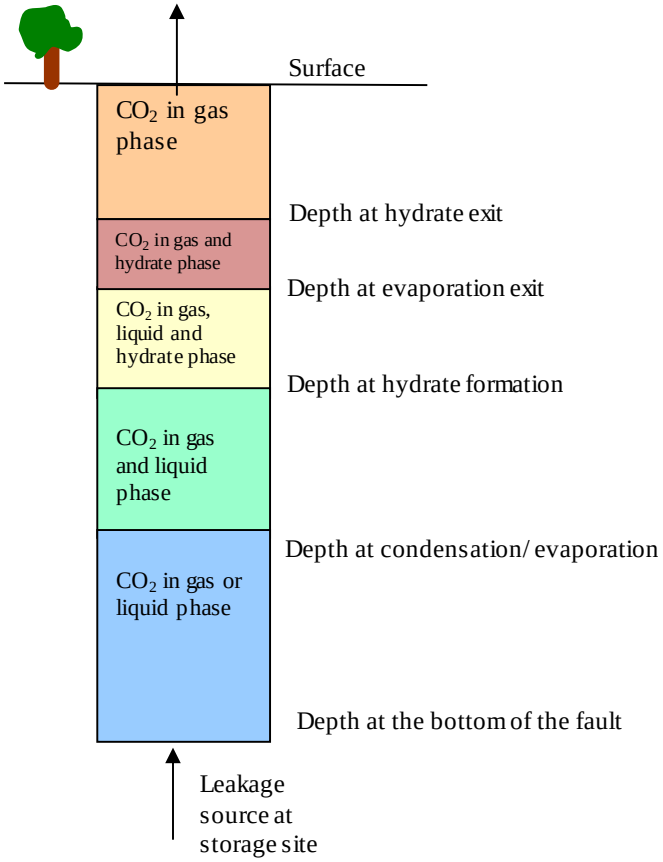

Figure 2.1: Schematic representations of key phase regions during CO_2 leakage. CO_2 is in gas or liquid phase close to the leakage source as shown by the blue region. Leaked CO_2 reaches saturated state in the green region. CO_2 will condense or evaporate to form two phases in this region. The condensation/ evaporation depend on the P-T conditions at the entrance. CO_2-hydrates forms with adequate amount of water and amenable P-T conditions as shown by the yellow region. Below a certain pressure, the liquid CO_2 evaporates to form a two-phase region with gas and hydrates as shown by the red region. The hydrate melts to form a single gas phase as shown by the orange region close to the exit.

2.2 MATHEMATICAL MODEL

A non-isothermal, quasi-1D mathematical model was developed to estimate the leakage mass flux as a function of time. Mass flux is allowed only in the vertical direction. The conductive heat flux is accounted for in the direction perpendicular to flow. Equations shown can model non-isothermal multiphase flow in heterogeneous porous media. The mathematical model is based on the following assumptions:

1) Local thermodynamic equilibrium exists amongst all phases. Phase equilibrium was instantly reached within gridblocks.
2) Multiphase Darcy's law is used to compute fluxes of flowing phases.
3) Mass and energy transfer due to dispersion is negligible.
4) There is no chemical reaction or sorption of any species.
5) The contribution of kinetic energy to internal energy is negligible.
6) Work done by viscous forces is negligible.
7) Diffusive, radiative and conductive energy transfers are negligible.
8) Capillary pressure is neglected
9) Heat losses through vertical boundaries are negligible.
10) Mass and energy transfer due to dispersion are negligible.
11) Rock mass within a gridblock is constant.
12) Water component is insoluble in any CO_2 phase and CO_2 component is insoluble in aqueous phase. CO_2 content in hydrates is negligible.
13) Aqueous phase is immobile.
14) The salinity of the aqueous phase is zero.
15) Formed hydrates only affect the permeability.
16) The heat of hydrate formation/dissociation is neglected
17) The rocks surrounding the fault are impermeable.

Aqueous phase properties vary by less than 1.5% in the pressure and temperature ranges of interest compared to values at surface conditions and hence are assumed to be constant. The potential energy contribution (gD) is taken into account since the flow is vertical (Dodson, 1971, Ramberg 1971). The fluid will gain potential energy at the expense of enthalpy for flow in the vertical direction (Hagoort, 2005 and Patterson et al., 2008). For example, there is a gain in potential energy of 9.81 kJ/kg with an equivalent loss in fluid enthalpy for flow in a 1000 m vertical fault. Shown below are some terms which will help understand the subsequent equations.

1) Bulk volume, V_b, the product of the length, breadth and height of the gridblock/ chosen space. (m^3)
2) Porosity, φ, defined by the ratio of pore volume to bulk volume.
3) Pore volume, $V_p = \varphi V_b$. (m^3)
4) The area perpendicular to flow, A_f, product of length and breadth of the gridblock/chosen space for vertical flow. (m^3)

2.2.1 Conservation of Mass

Conservation of mass for each component taking the assumptions into account is shown in equation (2.1).

$$\frac{\partial(\varphi\rho_t)}{\partial t} + \nabla\bullet\sum_{j=l,g}\left(\rho_j v_j\right) = \dot{q}_i$$

where, (2.1)

$$\rho_t = \rho_g S_g + \rho_l S_l$$

$$S_g + S_l + S_w = 1$$

The first term refers to the net rate of accumulation of each component over specified volume. Fluxes in and out of the volume are accounted for in the second term. Source and sink terms are accounted in the third term. The term v_j refers to the volumetric flux of phase j (Darcy velocity), subscripts l, g and w refer to the liquid, gas and water phase respectively and ∇ is the gradient operator in the vertical direction. ρ_j is the mass density of phase j, q_i represents the point sources or sinks for flowing components, S_j represents the volumetric saturation of phase j and t is time. The volumetric saturations are defined so that they sum to 1 (saturation constraint).

2.2.2 Conservation of Momentum

The generalized Darcy's law for multiphase flow in porous media was used as a simplified momentum balance as shown in equation (2.2). The volumetric flux, v_j of each phase in terms of the phase pressure is given by.

$$
\begin{aligned}
v_j &= -\frac{kk_{rj}}{\mu_j}\left[\nabla P_j - \rho_j g\right] \equiv -\lambda_j\left[\nabla P_j - \rho_j g\right] \\
\lambda_j &= \frac{kk_{rj}}{\mu_j} \\
k &= k_{red}k_{abs} \\
k_{red} &= \left(1 - S_h\right)^{n_h}
\end{aligned}
\tag{2.2}
$$

where k_{abs} is the permeability of the medium, k_{rj} is the relative permeability of phase j k_{red} is the permeability reduction factor due to the presence of hydrates, s_h is the hydrate saturation and n_h is the hydrate exponent. Relative permeability depends on the saturation only, g is the gravitational force, μj is the viscosity of phase j. Density and viscosity are functions of pressure (P) and temperature (T). λj is the mobility of phase j.

2.2.3 Conservation of Energy

The total energy conservation equation after the assumptions are taken into account is shown in equation (2.3).

$$\frac{\partial U_t}{\partial t} + \nabla \bullet \sum_{j=l,g} \left(\rho_j v_j \left(h_j - gD \right) \right) + \dot{Q}_L = \dot{q}_h$$

Where,

$$U_t = (1-\varphi)\rho_r u_r + \varphi\left(\rho_w S_w u_w + \rho_g S_g u_g + \rho_l S_l u_l\right) \quad (2.3)$$

$$-\varphi g D\left(\rho_w S_w + \rho_g S_g + \rho_l S_l\right)$$

The first term is the net rate of accumulation of internal energy in the specified volume. Energy fluxes in and out of the volume are accounted for in the second term as convective flux. Heat losses to the surroundings are accounted for in the third term. Source and sink terms are accounted for in the fourth term. U_t is the sum of rock and total fluid internal energies; h_j is the mass enthalpy of phase j, u_j is the mass internal energy of phase j, Q_l is the heat losses, q_h is the source and sink of enthalpy rates, D is the depth, ρ_r is rock density, u_r is rock internal energy, ρ_w is water density and u_w is water internal energy.

2.2.4 Constitutive Relationships

The balance equations are not sufficient to describe the leakage problem. Additional equations, relationships and assumptions are required. This section presents the constitutive relationships for rock, rock-fluid and fluid properties that provide the additional equations.

1) Porosity is assumed to be independent of pressure. It is allowed to vary spatially.
2) Rock density and permeability are functions of space.

3) Rock internal energy is assumed to be a function of its heat capacity (C_{vr}) and temperature (T) as shown in equation (2.4). T_{ref} is the reference temperature, which was taken as 298K. C_{vr} is assumed to be constant.

$$u_r = C_{vr}(T - T_{ref}) \tag{2.4}$$

4) Thermal conductivity - The thermal conductivity is assumed to vary spatially but not with time.

5) Water density is assumed to be constant. Water internal energy is assumed to be a function of its heat capacity (C_{vw}) and temperature (T) as shown in equation (2.5).

$$u_w = C_{vw}(T - T_{ref}) \tag{2.5}$$

6) Temperature and mole fractions are calculated as a function of pressure and total internal energy.

7) The fluid properties such as density, viscosity, fluid enthalpies and fluid internal energies are estimated using pressure and total internal energy.

8) Fluid saturation is calculated using the saturation constraint and known mole fractions. In the single phase regions, the saturation is determined based on the density of the fluid. In the two phase regions, the saturations are calculated with the equations shown in equation (2.6). V_j is the molar volume of phase j and x_j is the mole fraction of phase j.

$$\begin{aligned} &S_g + S_l + S_w = 1 \\ &x_g + x_l = 1 \\ &S_g = (1 - S_w)\frac{x_g V_g}{x_g V_g + x_l V_l}, S_l = (1 - S_w)\frac{x_l V_l}{x_g V_g + x_l V_l} \end{aligned} \tag{2.6}$$

9) Several experiments have been reported showing the effect of CO_2-hydrates on rock permeability (Kumar et al., 2010, Masuda et al., 1997). These experimental data were used to calibrate the correlation between the permeability and hydrate saturation given by equation (2.7).

$$k_{red} = (1 - S_h)^{n_h}$$
$$k = k_{red} k_{abs} \tag{2.7}$$

The permeability reduction factor, k_{red} in the hydrate region is only a function of the hydrate saturation, s_h, and a hydrate exponent, n_h. The hydrate exponent typically varies from 3 to 5 based on the hydrate saturation. An exponent of 3 was used for this study based on the experimental results (Kumar et al., 2010, Masuda et al., 1997).

10) Relative permeability is a function of saturation. The relative permeability is expressed by a Corey-type model as shown in equation (2.8).

$$k_{rj} = k_{rj}^{o} \left(\frac{S_j - S_{jr}}{1 - S_{wr} - \sum_{j=l,g} S_{jr}} \right)^{nj} \quad \text{for } j = l, g \tag{2.8}$$

S_{jr} is the residual saturation of phase j, k_{rj}^{o} is the end-point relative permeability of phase j, n_j is the phase exponent and S_{wr} is the residual water saturation. The water relative permeability is zero since its saturation is assumed to be residual water saturation.

2.2.5 Initial and Boundary Conditions

Equations (2.1) and (2.3) together comprise a pair of nonlinear second-order partial differential equations. The initial conditions of pressure, temperature and saturations must be specified in the domain of interest. At least two conditions (one in terms of pressure and one in terms of enthalpy/temperature or in terms of mass and energy flux) are required at the boundaries. The mass flux at the lateral boundaries was specified as zero to represent a no-flow boundary. Mass fluxes across the vertical boundaries are specified in terms of Darcy flux as shown in the equation (2.2). The energy fluxes across the vertical boundaries are written in terms of the incoming mass flux multiplied by the fluid mass enthalpy. The energy fluxes across the lateral boundaries are considered to be conductive fluxes. This is modeled with a Vinsome and Westerveld type heat loss function (Vinsome and Westerveld, 1980).

2.3 Phase Behavior and Fluid Properties

The mass and energy conservation equation along with Darcy's law was used to estimate the changes in total mass and total internal energy. The Span-Wagner technical EOS for CO_2 (Span and Wagner, 2003) was used to calculate fugacities and fluid properties. The Van der Waals - Platteeuw model for hydrate formation (Pedersen, 2014) is used to identify hydrate formation conditions.

The Span-Wagner multi-parameter technical equation of state is used to compute the thermodynamic properties of each fluid phase (Span and Wagner, 2003). This EOS is a reduced form (12 parameters) of Span-Wagner EOS for CO_2 (56 parameters) used in the NIST database (NIST, 2015). Although computationally intensive, this EOS was considered to be the most accurate in all fluid regions encountered in this study (Böttcher

et al, 2012). This equation of state is explicit in the Helmholtz free energy, a, with density and temperature as independent variables. The dimensionless form of Helmholtz energy based SW-EOS is shown in equation (2.9).

$$P(\delta,\tau) = \rho RT\left(1+\delta\alpha_{\delta}^{\ r}\right)$$

where (2.9)

$$\tau = \frac{T_c}{T},\ \delta = \frac{\rho}{\rho_c},\ \alpha = \frac{a(\rho,T)}{RT}$$

where ρ is the density, δ is the reduced density, τ is the reduced temperature and $\alpha_{\delta}^{\ r}$ is the derivative of the real part of dimensionless Helmholtz energy with respect reduced density. The values for the critical properties and other relevant parameters are shown in Table 2.1.

Table 2.1: Critical property values and other relevant constants used in the EOS

Critical Pressure, Pc, MPa	7.3773
Critical Temperature, Tc, K	304.1282
Acentric factor	0.2250
Universal gas constant, R, J/mol/K	8.3140
Molecular weight, Mw, g/mol	44.0098
Critical density, ρ_c, kg/m^3	467.6000

The dimensionless Helmholtz energy term is shown in equation (2.10). α^0 is the ideal part and α^r is the real part of the dimensionless Helmholtz energy. The expansion for the ideal part of dimensionless Helmholtz energy is shown in equation (2.11) and the corresponding values for a_i and θ_i are given in Table 2.2. The expansion for the real part of dimensionless Helmholtz energy is shown in equation (2.12) and the corresponding values for n_i are given in Table 2.3.

$$\alpha(\delta,\tau) = \alpha^{o}(\delta,\tau) + \alpha^{r}(\delta,\tau) \tag{2.10}$$

$$\alpha^{o}(\delta,\tau) = \ln(\delta) + a_1{}^{0} + a_2{}^{0}\tau + a_3{}^{0}\ln(\tau) + \sum_{i=4}^{8} a_i{}^{0}\ln\left[1-\exp\left(-\tau\theta_i{}^{o}\right)\right] \tag{2.11}$$

Table 2.2: Values for a_i and θ_i used in the ideal part of dimensionless Helmholtz energy

i	a_i	θ_i	i	a_i	θ_i
1	8.37304456		5	0.62105248	6.11190
2	-3.70454304		6	0.41195293	6.77708
3	2.50000000		7	1.04028922	11.32384
4	1.99427042	3.15163	8	0.08327678	27.08792

$$\alpha^{r}(\delta,\tau) = \sum_{i=1}^{5} n_i\delta^{d_i}\tau^{t_i} + \sum_{i=1}^{7} n_i\delta^{d_i}\tau^{t_i}\exp\left(-\delta^{p_i}\right)$$

$$\alpha^{r}(\delta,\tau) = \begin{bmatrix} +n_1\delta\tau^{0.250} + n_2\delta\tau^{1.250} + n_3\delta\tau^{1.500} \\ +n_4\delta^{3}\tau^{0.250} + n_5\delta^{7}\tau^{0.875} + n_6\delta\tau^{2.375}e^{-\delta} \\ +n_7\delta^{2}\tau^{2.000}e^{-\delta} + n_8\delta^{5}\tau^{2.125}e^{-\delta} + n_9\delta\tau^{3.500}e^{-\delta^2} \\ +n_{10}\delta\tau^{6.500}e^{-\delta^2} + n_{11}\delta^{4}\tau^{4.750}e^{-\delta^2} + n_{12}\delta^{2}\tau^{12.500}e^{-\delta^3} \end{bmatrix} \tag{2.12}$$

Table 2.3: The values for n_i used in the real part of dimensionless Helmholtz energy

i	n_i	i	n_i	i	n_i
1	8.9875108×10^{-1}	5	2.2053253×10^{-4}	9	$-3.6643143 \times 10^{-1}$
2	-2.1281985×10^{0}	6	4.1541823×10^{-1}	10	$-1.4407781 \times 10^{-3}$
3	$-6.8190320 \times 10^{-2}$	7	7.1335657×10^{-1}	11	$-8.9166707 \times 10^{-2}$
4	7.6355306×10^{-2}	8	3.0354234×10^{-4}	12	$-2.3699887 \times 10^{-2}$

The fugacity equation is shown in equation (2.13). The expansion for the derivative terms are also mentioned in this equation. Equations (2.9) through (2.13) are solved at equilibrium to identify the correct roots. Direct root solving method cannot be

used since several parameters are involved. Instead, an iterative Newton-Raphson method was used for the root finding approach. This method guarantees convergence as long as the root is in the pre-defined interval. The number of iterations increases in the near-critical region and close to the saturation conditions. The accuracy of this EOS came at the cost of computation time which was up to twenty times higher than for a cubic equation of state ((Böttcher et al., 2012).

$$\ln\left(\phi\left(\tau,\delta\right)\right) = \alpha^{r} + \delta\alpha_{\delta}{}^{r} - \ln\left(1+\delta\alpha_{\delta}{}^{r}\right)$$

where, (2.13)

$$\alpha_{\delta}{}^{o} = \left[\frac{\partial\alpha^{o}}{\partial\delta}\right]_{\tau}, \alpha_{\tau}{}^{o} = \left[\frac{\partial\alpha^{o}}{\partial\tau}\right]_{\delta}, \alpha_{\delta}{}^{r} = \left[\frac{\partial\alpha^{r}}{\partial\delta}\right]_{\tau}, \alpha_{\tau}{}^{r} = \left[\frac{\partial\alpha^{r}}{\partial\tau}\right]_{\delta}$$

Once the roots are identified, the corresponding enthalpy and internal energy are calculated with equations (2.14) and (2.15).

$$h\left(\delta,\tau\right) = RT\left[1+\tau\left(\alpha_{\tau}{}^{o} + \alpha_{\tau}{}^{r}\right) + \delta\alpha_{\delta}{}^{r}\right] \quad (2.14)$$

$$u\left(\delta,\tau\right) = RT\left[\tau\left(\alpha_{\tau}{}^{o} + \alpha_{\tau}{}^{r}\right)\right] \quad (2.15)$$

The CO_2 viscosity is estimated with a corresponding states model used in the NIST (Vesovic et al., 1990; Fenghour et al., 1998). The viscosity is decomposed as a function of pressure and density into three separate contributions as shown in equation (2.16). The critical enhancement of viscosity contribution in equation (2.16) is less than 1% and hence neglected in this calculation.

$$\mu(\rho,T) = \mu_o(T) + \Delta\mu(\rho,T) + \Delta\mu_c(\rho,T)$$

Where,

$\mu_o(T) =$ Viscosity in the zero – density limit (2.16)

$\Delta\mu(\rho,T) =$ Excess viscosity

$\Delta\mu_c(\rho,T) =$ Critical enhancement of viscosity

The expansion of viscosity in the zero-density limit and excess viscosity are shown in equation (2.17) and the corresponding values for a_i and d_{ij} are given in Table 2.4. The viscosity is calculated explicitly with equation (2.16) and (2.17), respectively.

$$\mu_o(T) = \frac{1.00697T^{1/2}}{G_\mu^*(T^*)}$$

$$\ln G_\mu^*(T^*) = \sum_{i=0}^{4} a_i (\ln T^*)^i$$

$$T^* = \frac{kT}{\varepsilon} \quad (2.17)$$

Where,

$\varepsilon / k = 251.196K$

$$\Delta\mu(\rho,T) = d_{11}\rho + d_{21}\rho^2 + \frac{d_{64}\rho^6}{T^{*3}} + d_{81}\rho^8 + \frac{d_{82}\rho^8}{T^*}$$

Table 2.4: The values for a_i and d_{ij} used in the viscosity estimation

i	a_i	ij	d_{ij}
0	2.351560×10^{-1}	11	0.4071119×10^{-2}
1	-4.912660×10^{-1}	21	0.7198037×10^{-4}
2	5.211155×10^{-2}	64	$0.2411697 \times 10^{-16}$
3	5.347906×10^{-2}	81	$0.2971072 \times 10^{-22}$
4	-1.537102×10^{-2}	82	$-0.1627888 \times 10^{-22}$

The hydrate saturation was calculated using the Van der Waals-Platteeuw method available in PVTSIM software (Pedersen, 2014). It is assumed that all the water available is converted to hydrates when the pressure-temperature condition for hydrate formation is attained. This is a reasonable assumption for low water saturations.

2.4 NUMERICAL FORMULATION

This section describes the numerical solution of the equations described in the mathematical model. Numerical solution method used is based on the methods employed in the geothermal reservoir simulators (Faust and Mercer, 1979a, 1979b). The techniques used are finite difference approximation for the differential equations, inexact newton method to treat nonlinearities and iterative method to solve the residual equations implicitly.

2.4.1 Grid Notation

The technique used to solve equations (2.1) and (2.3) are based on the finite-difference scheme which uses block-centered grid with allowance for variable spacing. For this method, the vertical extent of the porous medium is subdivided into rectangular grid blocks as shown in Figure 2.2. The fluid and reservoir properties are assumed uniform within the gridblock.

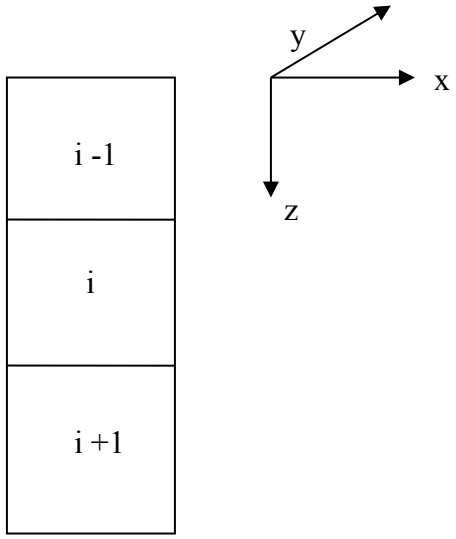

Figure 2.2: Schematic grid system representation

The difference function, f, evaluated in space at opposite gridfaces is denoted in equation (2.18). The temporal difference function, f, calculated between the new time level and the old time level is denoted in equation (2.19).

$$\Delta_z f = f_{i+1/2} - f_{i-1/2} \tag{2.18}$$

$$\Delta_t f = f^{n+1} - f^{n} \tag{2.19}$$

2.4.2 Accumulation Terms

The accumulation terms in the mass and energy conservation equations are discretized with forward difference in time. They are shown in equation (2.20) where Δt is the time increment, n is the old time step and n+1 is the new time step.

$$V_b \frac{\partial(\varphi \rho_t)}{\partial t} = V_b \varphi \frac{\rho_t^{n+1} - \rho_t^n}{t^{n+1} - t^n} = V_b \varphi \frac{\rho_t^{n+1} - \rho_t^n}{\Delta t}$$
$$V_b \frac{\partial(U_t)}{\partial t} = V_b \frac{U_t^{n+1} - U_t^n}{t^{n+1} - t^n} = V_b \frac{U_t^{n+1} - U_t^n}{\Delta t} \tag{2.20}$$

2.4.3 Transmissibility Terms

The inter-block transmissibility for phase j is evaluated at gridface as shown in equation (2.21) where ΔD is the length increment in the flow direction.

$$T_{g,i+1/2} = \left(\frac{kA_f k_{rg} \rho_g}{\Delta D \mu_g} \right)_{i+1/2}$$
$$T_{l,i+1/2} = \left(\frac{kA_f k_{rj} \rho_g}{\Delta D \mu_g} \right)_{i+1/2} \tag{2.21}$$
$$T_{h,i+1/2} = \left(h_{g,i+1/2} - gD_{i+1/2} \right) T_{g,i+1/2} + \left(h_{l,i+1/2} - gD_{i+1/2} \right) T_{l,i+1/2}$$

The inter-block transmissibility terms are divided into two parts. The first part ($kA_f/\Delta D$) is a function of space and the second part ($\rho k_r/\mu$) is a nonlinear function of pressure and/or energy. The space dependent part is computed using a harmonic average as shown in equation (2.22).

$$\left(\frac{kA_f}{\Delta D} \right)_{i+1/2} = \frac{2A_{f_{i+1}} k_i k_{i+1} A_{f_i}}{\Delta D_{i+1} k_i A_{f_i} + \Delta D_i k_{i+1} A_{f_{i+1}}} \tag{2.22}$$

The nonlinear part of the transmissibility terms is assigned the upstream value based on single-point upstream weighting. The enthalpy contribution is also determined based on the upstream node. The upstream node is determined by the larger phase potential node when they are compared between (i) and (i+1). The phase potential was

shown in equation (2.23) where D is the depth at block center and P is the pressure of phase j. The difference form of phase potential is written as shown in equation (2.24).

$$\nabla\phi_j = \nabla P_j - \rho_j g \nabla D \tag{2.23}$$

$$\Delta\phi_{i+1/2,j} = \left(P_{i+1} - P_i\right) - \rho_{i+1/2,j} g \left(D_{i+1} - D_i\right) \tag{2.24}$$

2.4.4 Heat-Loss Terms

Vinsome and Westerveld heat-loss function is used to compute the heat losses through lateral boundaries (Vinsome and Westerveld, 1980). This is a semi-analytical model used to determine heat-transfer to/from an infinite medium by conduction. This is commonly used to account for heat loss to overburden and underburden in thermal simulations. The temperature at the base or cap rock is assumed to be a function of time and distance. The temperature at any time, at a distance far from the flow boundary is given by equation (2.25).

$$T(z,t) - T_{ini} = \left(T_{res} - T_{ini} + pz + qz^2\right)\exp\left(-\frac{z}{d}\right) \tag{2.25}$$

where z is the distance into cap rocks with the interface between the reservoir and caprock is at z=0. T_{ini} is the temperature at the boundary at t = 0, t is time and T_{res} is the temperature in the reservoir/fault block. d is the diffusion length defined as shown in equation (2.26).

$$d = \frac{\sqrt{\alpha t}}{2} \tag{2.26}$$

where α is the thermal diffusivity of the caprock. The coefficients p and q are fitting parameters computed with the boundary conditions, heat loss equation and the energy conservation equation in the overburden. At the interface between the reservoir and over/underburden (z=0), the temperature is constrained by the balance equation shown in equation (2.27). This equation ensures the energy within the over/underburden is conserved.

$$\left(\rho C_p\right)_{burden}\frac{\partial T}{\partial t}=\left(K_c\right)_{burden}\frac{\partial^2 T}{\partial z^2} \tag{2.27}$$

The heat loss flux and the fitting parameters p and q are written in finite difference notation as shown in equations (2.28), (2.29) and (2.30), respectively.

$$q_{l_i}{}^{n+1}=K_c\left(\frac{T_i{}^{n+1}-T_i{}^{o}}{d}-p\right) \tag{2.28}$$

$$p=\frac{\dfrac{\alpha\Delta t\left(T_i{}^{n+1}-T_i{}^{o}\right)}{d}+I^n-\dfrac{d^3\left(T_i{}^{n+1}-T_i{}^{n}\right)}{\alpha\Delta t}}{3d^2+\alpha\Delta t} \tag{2.29}$$

$$q=\frac{2pd-\left(T_i{}^{n+1}-T_i{}^{o}\right)+\dfrac{d^2\left(T_i{}^{n+1}-T_i{}^{n}\right)}{\alpha\Delta t}}{2d^2} \tag{2.30}$$

$$I^n=\left(T_i{}^{n}-T_i{}^{o}\right)d^n+p^n\left(d^n\right)^2+2q^n\left(d^n\right)^3 \tag{2.31}$$

where the superscript n denotes the previous time step, o is the initial time step, n+1 is the current time step and K_c is the thermal conductivity of the caprock. Variables without specified time-step are calculated at the current time step. Equations (2.29), (2.30) and (2.31) are solved simultaneously to obtain the heat loss flux. Heat loss of finite volume

which has a surface area A_{hl} that contacted the surrounding rock is computed with equation (2.32).

$$V_b Q_{loss} = A_{hl} q_l \tag{2.32}$$

2.4.5 Residual Equation

The conservation equations are written as a set of implicit finite difference equations. The final residual equations for mass and energy are shown in equation (2.33) and equation (2.34), respectively.

$$\begin{aligned} R_m = {} & \frac{\varphi V_b}{\Delta t}\left(\rho_t{}^{n+1} - \rho_t{}^{n}\right) - \Delta\left[\left(T_g + T_l\right)^{n+1}\Delta P^{n+1}\right] \\ & + \Delta\left[\left(T_g\rho_g + T_l\rho_l\right)^{n+1} g\Delta D\right] = 0 \end{aligned} \tag{2.33}$$

$$\begin{aligned} R_e = {} & \frac{V_b}{\Delta t}\left(U_t{}^{n+1} - U_t{}^{n}\right) - \Delta\left[\left(T_h\right)^{n+1}\Delta P^{n+1}\right] \\ & + \Delta\left[\left(T_g\rho_g\left(h_g - gD\right) + T_l\rho_l\left(h_l - gD\right)\right)^{n+1} g\Delta D\right] + V_b Ql_{oss}{}^{n+1} = 0 \end{aligned} \tag{2.34}$$

The accumulation, transmissibility and the heat loss terms are substituted into the residual equations. The difference operator Δ for the transmissibility term is defined for the vertical direction as shown in equation (2.35).

$$\begin{aligned} \Delta_z\left[T_g{}^{n+1}\left(\Delta P^{n+1} - \rho_g g\Delta D\right)\right] = {} & T_{g,i+1/2}{}^{n+1}\left(P_{i+1}{}^{n+1} - P_i{}^{n+1}\right) \\ & - T_{g,i+1/2}{}^{n+1}\rho_{g,i+1/2} g\Delta D_{i+1/2} - T_{g,i-1/2}{}^{n+1}\left(P_i{}^{n+1} - P_{i-1}{}^{n+1}\right) \\ & + T_{g,i-1/2}{}^{n+1}\rho_{g,i-1/2} g\Delta D_{i+1/2} \end{aligned} \tag{2.35}$$

2.4.6 Solution Method

The residual equations (2.33) and (2.34) are solved simultaneously for the unknown pressure and total energy in each gridblock for each time step. The equations are solved implicitly to account for the nonlinearities in the transmissibility terms. Iterative scheme is used for the accumulation terms to solve the difference equation until a specified tolerance limit was attained. As a first step, the mass balance and the energy balance difference equations are expanded for the grid representation shown in Figure 2.2 as shown in equations (2.36) and (2.37), respectively. The flow occurs in the direction from i+1 to i to i-1.

Expanding mass difference equation,

$$\varphi\left[\frac{\rho_{t,i}^{\,n+1}-\rho_{t,i}^{\,n}}{\Delta t}\right]-\frac{1}{\Delta D^2}\left[\begin{array}{l}\left(\dfrac{\rho_g kk_{rg}}{\mu_g}+\dfrac{\rho_l kk_{rl}}{\mu_l}\right)_{i+1/2}^{n+1}\left(P_{i+1}-P_i\right)^{n+1}\\ -g\Delta D\left(\dfrac{k\rho_g{}^2k_{rg}}{\mu_g}+\dfrac{k\rho_l{}^2k_{rl}}{\mu_l}\right)_{i+1/2}^{n+1}\\ -\left(\dfrac{\rho_g kk_{rg}}{\mu_g}+\dfrac{\rho_l kk_{rl}}{\mu_l}\right)_{i-1/2}^{n+1}\left(P_i-P_{i-1}\right)^{n+1}\\ +g\Delta D\left(\dfrac{k\rho_g{}^2k_{rg}}{\mu_g}+\dfrac{k\rho_l{}^2k_{rl}}{\mu_l}\right)_{i-1/2}^{n+1}\end{array}\right]=0 \qquad (2.36)$$

Expanding energy difference equation,

$$H_j = h_j - gD$$

$$\left[\frac{U_{t,i}^{n+1} - U_{t,i}^{n}}{\Delta t}\right] - \frac{1}{\Delta D^2}\left[\begin{array}{l}\left(\frac{\rho_g k k_{rg} H_g}{\mu_g} + \frac{\rho_l k k_{rl} H_l}{\mu_l}\right)_{i+1/2}^{n+1}\left(P_{i+1} - P_i\right)^{n+1} \\ -g\Delta D\left(\frac{k\rho_g{}^2 k_{rg} H_g}{\mu_g} + \frac{k\rho_l{}^2 k_{rl} H_l}{\mu_l}\right)_{i+1/2}^{n+1}\end{array}\right] \qquad (2.37)$$

$$+\frac{1}{\Delta D^2}\left[\begin{array}{l}\left(\frac{\rho_g k k_{rg} H_g}{\mu_g} + \frac{\rho_l k k_{rl} H_l}{\mu_l}\right)_{i-1/2}^{n+1}\left(P_i - P_{i-1}\right)^{n+1} \\ -g\Delta D\left(\frac{k\rho_g{}^2 k_{rg} H_g}{\mu_g} + \frac{k\rho_l{}^2 k_{rl} H_l}{\mu_l}\right)_{i-1/2}^{n+1}\end{array}\right] + Q_{loss,i}^{n+1} = 0$$

The mass balance difference equation shown in equation (2.36) is rearranged in terms of the pressure P_{i-1} as shown in equation (2.38).

$$P_{i-1} = P_i - \frac{1}{\left(\frac{\rho_g k k_{rg}}{\mu_g} + \frac{\rho_l k k_{rl}}{\mu_l}\right)_{i-1/2}^{n+1}}\left[\begin{array}{l}\left(\frac{\rho_g k k_{rg}}{\mu_g} + \frac{\rho_l k k_{rl}}{\mu_l}\right)_{i+1/2}^{n+1}\left(P_{i+1} - P_i\right)^{n+1} \\ -g\Delta D\left(\frac{k\rho_g{}^2 k_{rg}}{\mu_g} + \frac{k\rho_l{}^2 k_{rl}}{\mu_l}\right)_{i+1/2}^{n+1} \\ +g\Delta D\left(\frac{k\rho_g{}^2 k_{rg}}{\mu_g} + \frac{k\rho_l{}^2 k_{rl}}{\mu_l}\right)_{i-1/2}^{n+1} \\ -\varphi\Delta D^2\left[\frac{\rho_t{}^{n+1} - \rho_t{}^{n}}{\Delta t}\right]\end{array}\right] \qquad (2.38)$$

This pressure (P_{i-1}) in equation (2.38) is substituted into the energy balance difference equation (2.37). The final difference equations led to a system of equations that is solved at every iteration level. Each horizontal cross-section was solved directly

using a secant method, for a given initial guess for pressure. Subsequently new temperature, mole fractions and pressures are estimated. The convergence was checked with the maximum pressure change and maximum permeability change between iterations as shown in equation (2.39) and equation (2.40) respectively.

$$P_{tol} = \sum_i \left| P_i^{m+1} - P_i^{m} \right| \tag{2.39}$$

$$k_{tol} = \sum_i \left| k_i^{l+1} - k_i^{l} \right| \tag{2.40}$$

The superscript refers to the iteration level. The convergence criterion for P_{tol} was 0.01 Pa and k_{tol} was 10^{-5} md. The pressure convergence is usually reached within 15 iterations and the permeability convergence is reached within 5 iterations in the event of hydrate formation. Flowchart of the solution procedure is shown in Figure 2.3.

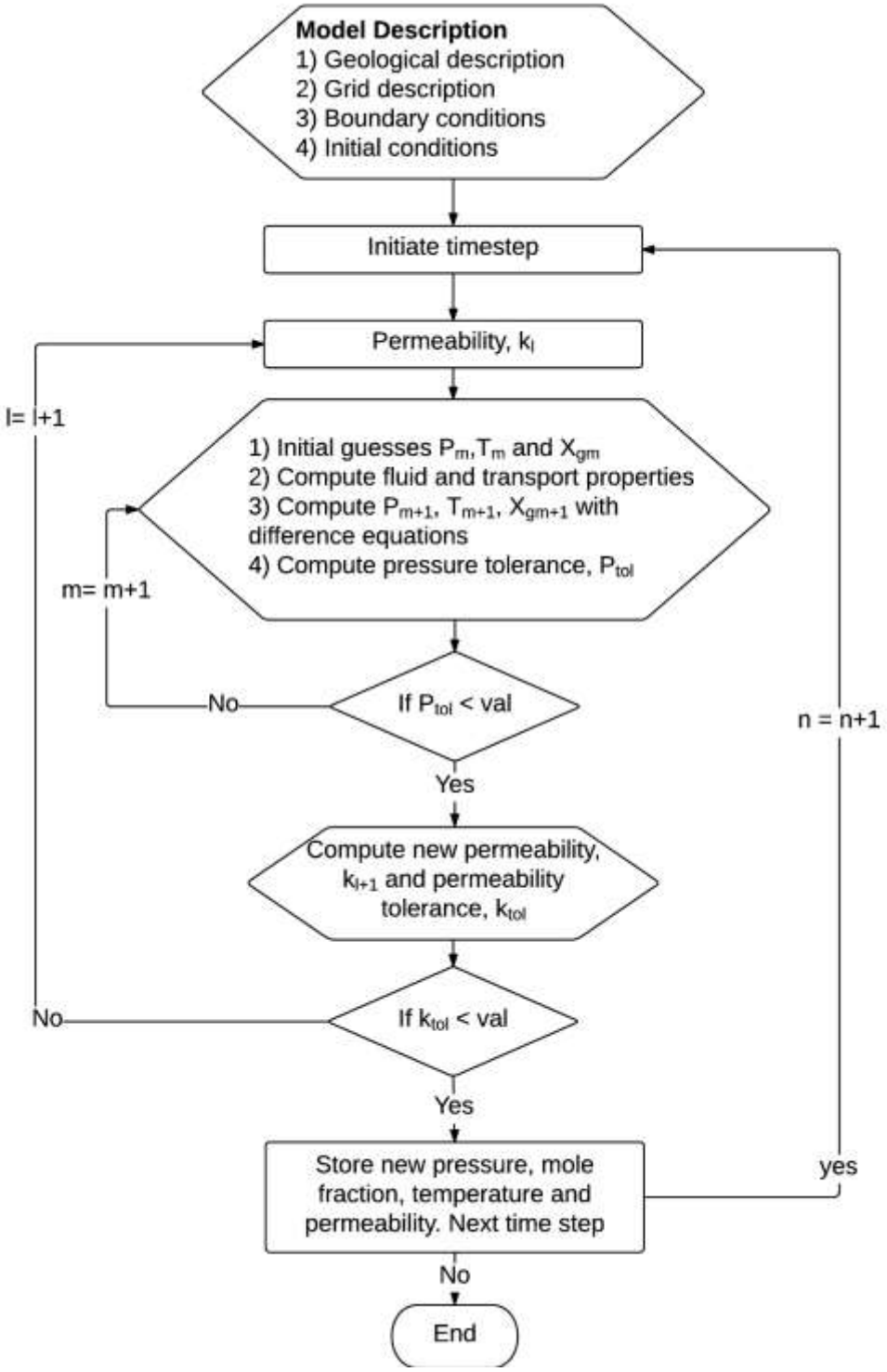

Figure 2.3: Numerical model solution flowchart

2.5 MODEL VALIDATION

The purpose of this section is to validate the numerical model with experimental data, analytical solutions and numerical models. In the first example, the equation of state is validated with experimental data and NIST database. In the second example, the result from the numerical model is compared with commercial simulator CMG-GEM (GEM, 2014) to validate the ability to model vertical flow of CO_2. In the third example, a comparison is made with Lauwerier's analytical solution to validate the results of heat convection within the fault and heat conduction losses to the surroundings (Lauwerier, 1955).

2.5.1 Equation of State Comparison

The Span-Wagner Technical Equation of State (SWEOS) (Span and Wagner, 2003) is validated with data from NIST (NIST, 2015) for CO_2. Result from Peng-Robinson equation of state (PREOS) (Peng and Robinson, 1976) is also provided for comparison. The density of CO_2 as a function of depth is shown in Figure 2.4. The pressure was calculated with hydrostatic gradient and the temperature with the geothermal gradient. The density for the saturated region (gas-liquid coexistence) is shown in Figure 2.5.The results from the SWEOS, NIST and PREOS are shown in these Figures. There was good agreement in the results between SWEOS and NIST. Predicted densities from PREOS were accurate only for densities <420 kg/m^3. Experimental data (Wendland et al., 1999; Ng and Robinson., 1985; Adisasmito et al., 1991; Fan and Guo, 1999) for CO_2 hydrates was used to tune the hydrate model in PVTSIM (Pedersen, 2014). The obtained match with a binary interaction parameter of -0.136 is shown in Figure 2.6.

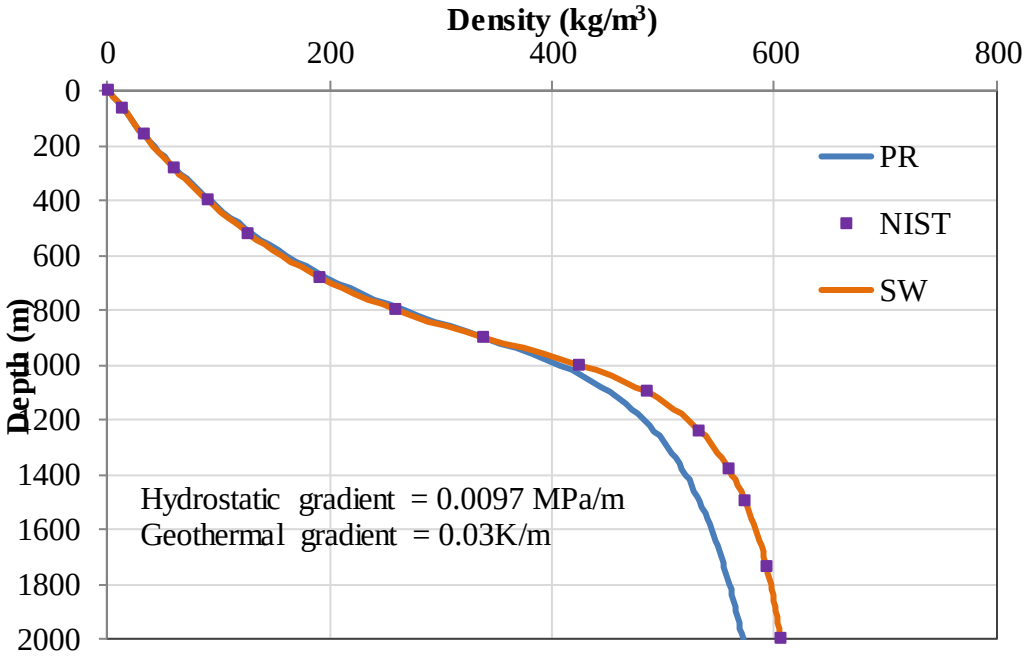

Figure 2.4: Comparison of density profile as a function of depth between three EOSes.

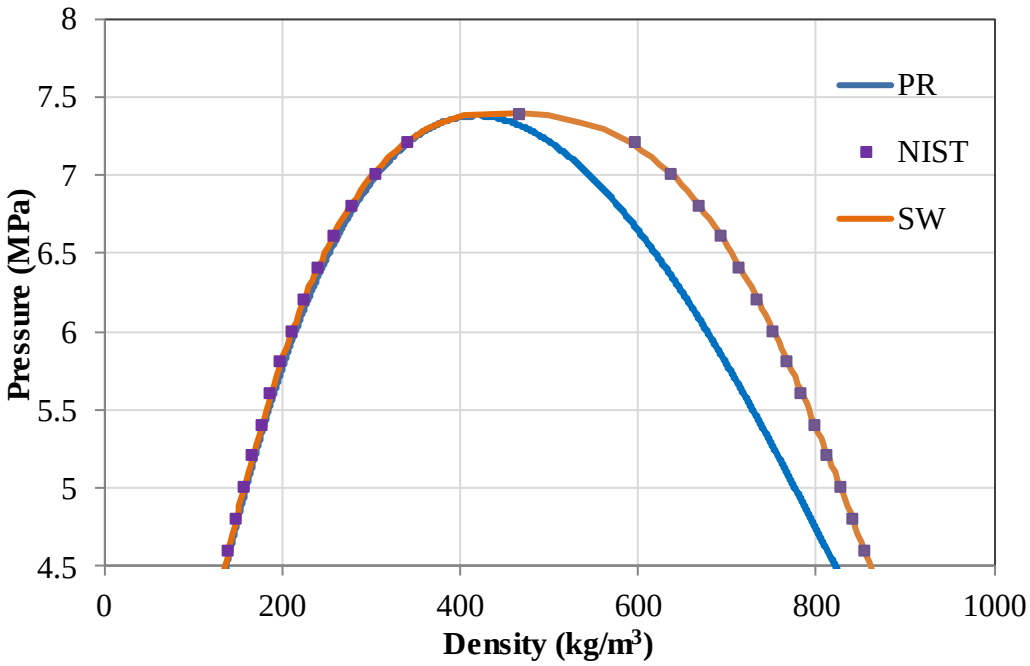

Figure 2.5: Comparison of density in the two phase region of CO_2 between three EOSes.

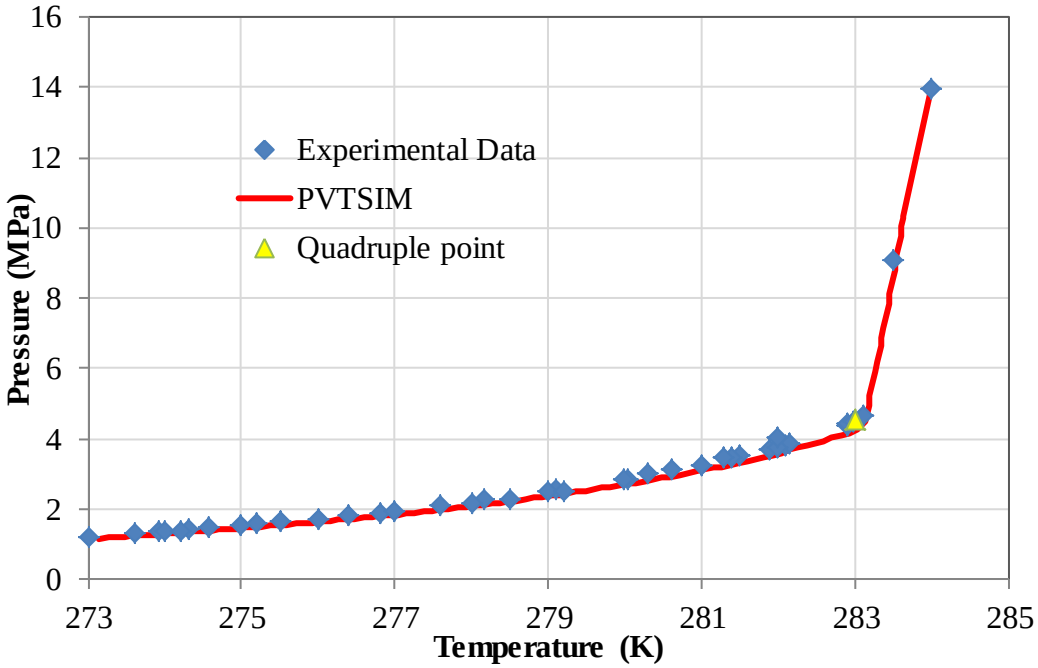

Figure 2.6: Prediction of equilibrium pressure of CO_2 hydrate in the CO_2-H_2O system from PVTSIM compared with compiled experimental data.

2.5.2 CMG Comparison

The numerical solution using the new model developed in this work was compared with the numerical solution using the CMG-GEM compositional EOS reservoir simulator. The numerical solutions for one-dimensional vertical flow of CO_2 with variable temperature are compared using identical fault properties. The energy balance was not included. The fluid properties were estimated using PREOS (Peng and Robinson, 1976) in CMG and SWEOS (Span and Wagner, 2003) in the new numerical model. Viscosity was calculated with the corresponding states model in CMG (Pedersen et al., 1984) and the numerical model (Vesovic et al., 1990; Fenghour et al., 1998). The pertinent input data are provided in Table 2.5. The problem was simulated with 70 gridblocks in CMG and 71 gridblocks in the new numerical model with a constant time

step of 1 day. As seen from Figure 2.7, the pressure profiles at 100 days are very close. The difference between the profiles is due to the difference in fluid properties estimated with different equation of states and viscosity models.

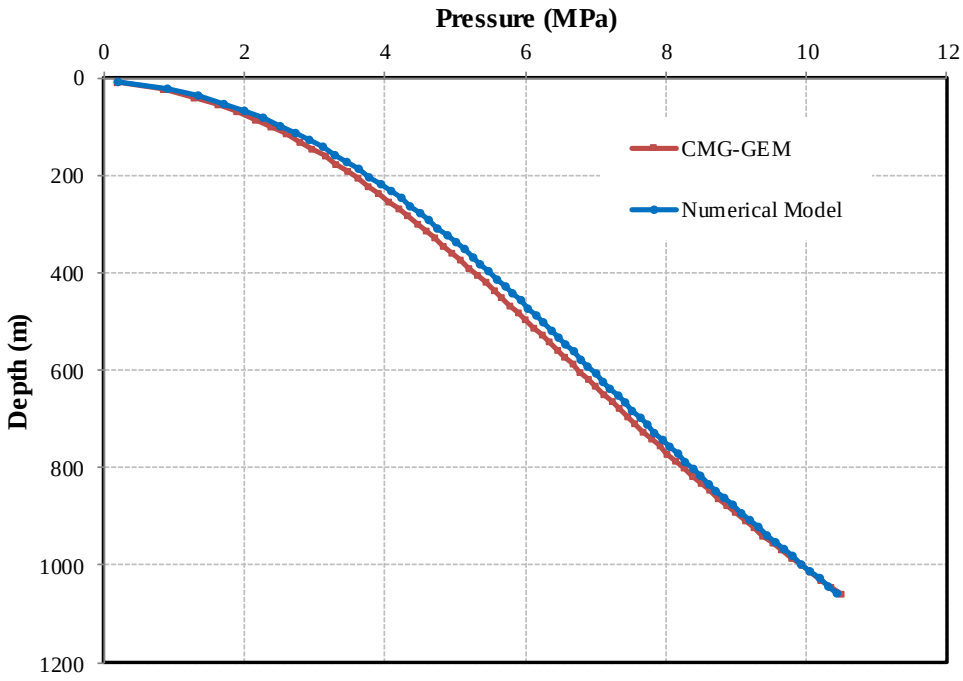

Figure 2.7: Comparison of pressure profile as a function of depth at 100 days for CMG and the numerical model.

Table 2.5: Input data for CMG simulation comparison

Parameters	**CMG**	**Numerical Model**
Number of gridblocks (nx, ny, nz)	(1,1,70)	(1,1,71)
Dimensions of gridblocks, Δx (m)	0.1	0.1
Dimensions of gridblocks, Δy (m)	10	10
Dimensions of gridblocks, Δz (m)	15.25	15
Length of the fault (m)	1067	1065
Time step size, Δt (day)	1	1
Initial Conditions		
Surface temperature (K)	289.15	289.15
Geothermal gradient (K/m)	0.03	0.03

Residual water saturation	0.2	0.2
Initial water saturation	0.2	0.2
Initial gas saturation	0.8	0.8
Reservoir Properties		
Permeability, md	1000	1000
Porosity	0.3	0.3
Boundary conditions		
Bottom hole incoming pressure (MPa)	10.4983	10.4983
Bottom hole outgoing pressure (MPa)	0.1552	0.1552
Relative permeability constants		
Gas phase end point	0.7	0.7
Gas phase exponent	4	4

2.5.3 Lauwerier's Problem Comparison

The analytical solution obtained by Lauwerier is used to validate the implementation of the energy balance and heat losses model. This problem describes the displacement of cold fluid by hot fluid in a horizontal thin permeable medium. The assumptions, equations and the final solution were discussed in detail in other reports (Lauwerier, 1955; Brantferger, 1990; Varavei, 2009). The final result was compared with the numerical model. The input data are shown in Table 2.6. The analytical and numerical temperature profiles shown in Figure 2.8 agree considerably well.

Table 2.6: Input data for Lauwerier's problem

Thickness (m)	2
Length (m)	200
Width (m)	50
Permeability, k (md)	5
Porosity, φ	0.2
Fluid Density, ρ_f (kg/m^3)	1050
Fluid heat capacity, C_f (kJ/kg/K)	4.2
Fluid velocity, v_f (m/s)	0.0001
Thermal conductivity, λ_s (kJ/s/m/K)	1.196
Rock density, ρ_r (kg/m^3)	2400
Rock heat capacity, C_r (kJ/kg/K)	0.4186

Injection temperature, T_{inj} (K)	533
Initial temperature, T_{ini} (K)	255

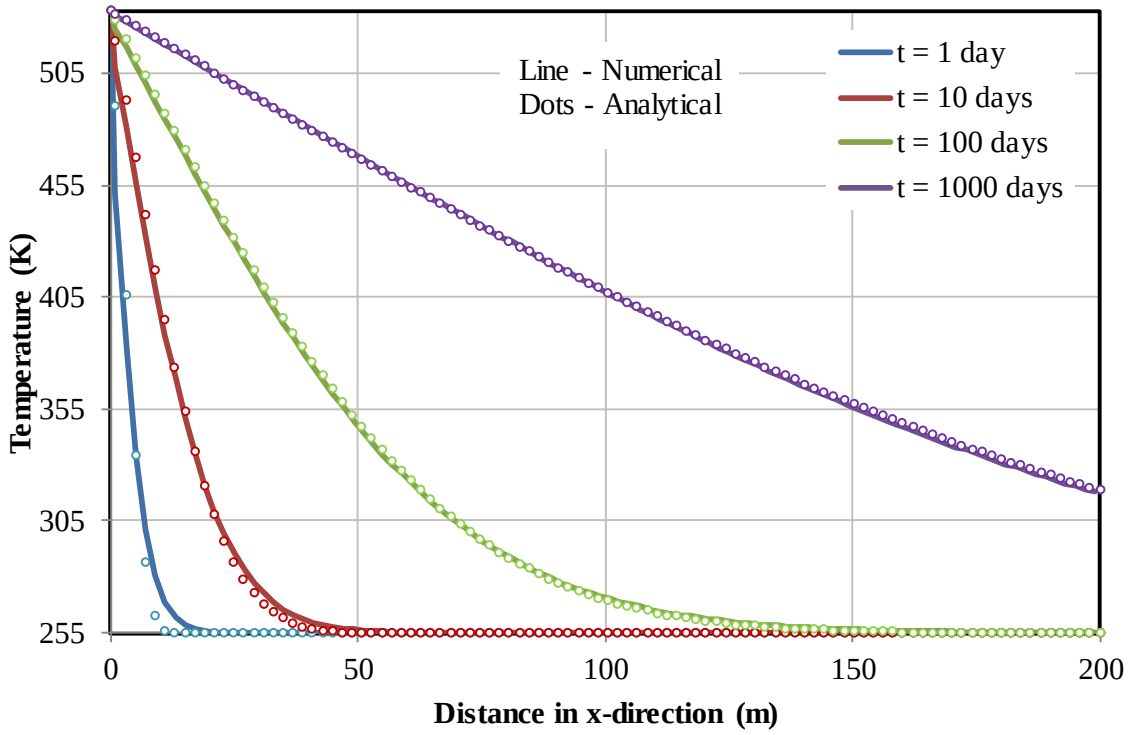

Figure 2.8: Comparison of heat convection and heat losses with Lauwerier's solution.

Chapter 3: Numerical Simulation of CO_2 Leakage Scenarios

This chapter presents the results obtained from the numerical simulation of leakage through faults/fractures. A brief introduction about the numerical modeling of leakage is presented. An example result for a typical fault leakage scenario is discussed next. The coupled nature of thermal and multiphase flow aspects will be investigated in this discussion. The factors affecting these phase changes were identified with the help of a sensitivity analysis on permeability, effective width, and overpressure.

3.1 INTRODUCTION

One of the main concerns for large-scale long-term geological storage is that CO_2 might leak towards the surface, away from the storage formation. The significance for these concerns is due to the adverse environmental impacts associated with it. Examples of some environmental hazards are contamination of groundwater, detrimental effects on subsurface ecosystems and asphyxiating release close to the surface among many others (Jones et al., 2015). Likelihood of leakage will depend whether the injected CO_2 encounter discontinuities in the caprock of the storage formation. Faults, fracture, abandoned wells and leaky injection wells provide a pathway for the CO_2 to leak through the caprock discontinuities. At the onset of leakage, the environmental consequences depend on the leakage mass flux. This provides a motivation to analyze and quantify leakage along such pathways.

The leakage pathways may exist prior to injection or be reactivated during injection either by geo-mechanical failures or by seismic activity (Rutqvist et al, 20070). Faults have higher permeability and consequently higher leakage mass flux compared with other leakage pathways. In addition, they can potentially conduct the CO_2 all the

way back to the surface as observed in natural analogues (Lewicki et al, 2007). Therefore, the study reported in this chapter focused on leakage through faults.

Depending on the structural nature of the pathway, CO_2 can reach all the way to the surface. Some of the CO_2 will leak off into intersecting permeable formations/ secondary traps encountered during upward migration depending on the geological properties of these formations (Chang et al., 2008). The pressure and temperature change as CO_2 migrates upwards with the possibility for multiphase coexistence (Pruess, 2004). The multiphase flow reduces the leakage mass flux. The leakage mass flux depends on the geometry (fault length, width, etc.), petrophysical properties (permeability, porosity, initial saturations, relative permeability etc.), initial conditions (pressure, temperature, etc.), boundary conditions (source, sink terms, etc.) of the fault and the thermal properties of the surroundings. Thus, the dynamic behavior of CO_2 leakage involves multiphase flow coupled with heat transport in a heterogeneous porous media.

Most previous attempts to numerically simulate this dynamic behavior of leakage were performed using the TOUGH2 simulator (Pruess, 2004, 2005, 2008, 2011a, 2011b). The TOUGH2 simulator (Pruess et al., 1999) is a three-dimensional, non-isothermal multi-component multi-phase numerical simulator for flow in porous media. TOUGH2 can be used to simulate fluid and heat flow including both latent and sensible heat, and gas-liquid phase transitions. Quasi-periodic variations in leakage rates from a large fault-zone once the temperature decreased enough for the gas to condense were reported. Uncertainty quantification study with NUFT simulator was performed to the estimate the effect of fault permeability, reservoir permeability and overpressure on the leakage mass flux (Lu et al., 2012). This study considered the non-isothermal effects but neglected the multiphase coexistence aspects.

Leakage mass flux results from the numerical model described in Chapter 2 are presented in this chapter. The goal of this model is to present the leakage mass flux taking CO_2 multiphase flow conditions into account and identify key controlling factors. During storage, presence of leakage pathways will not be known a priori. It is important to quantify the leakage to understand potential consequences. The sensitivity of the estimated flux to geological parameters provides insights into the preferred rock types for storage and the rock properties that need to be measured during site selection. The model can also provide insights into the operating conditions needed to minimize leakage and key pressure-temperature signals that might aid identification of leakage during monitoring (Jenkins et al., 2015). The model could also be used to analyse existing leakage and provide insights into remediation strategies required to plug the leak.

3.2 FAULT LEAKAGE SCENARIO RESULTS

An example result for a typical CO_2 fault-leakage scenario is discussed in this section. Specifically, the coupled effect of the thermal and multiphase flow aspects of leakage is illustrated. The leakage scenario considered for this example corresponds to CO_2 leakage through a vertical fault connected to the top of a storage reservoir. The storage reservoir is assumed to be at a depth of 1000 m. Thick and wide plume of CO_2 is assumed to have reached the top of the reservoir at the beginning of leakage simulation. The reservoir is represented as a continuous source of CO_2 at constant temperature and pressure at the fault inlet (bottom boundary) and is not explicitly modelled in this example.

An idealized representation of the vertical fault as shown in Chapter 1 is used for this leakage scenario. Homogenous vertical fault from the surface to a depth of 1000 m

with a permeability of 1000 mD, effective width of 0.1 m and breadth of 10 m is considered. The geological description of the fault is given in Table 3.1 and the schematic representation of the fault is shown in Figure 3.1. The fault wall rocks are assumed to be impermeable. Thus, there is no fluid flow across the later boundaries although there is heat exchanged through them. The surface temperature is assumed to be at 290.15 K (17 °C) and the surface pressure is assumed to be 0.10135 MPa (14.7 psi). This temperature and pressure act as the boundary condition at the top of fault. The initial temperature and pressure along the fault is calculated with an assumed geothermal gradient of 30°C/km and hydrostatic pressure gradient of 9.8 MPa/km as shown in Figure 3.2. The storage reservoir is over-pressurized due to the injection and storage ($\Delta P_s = P_{reservoir}-P_{hydrostatic}$). Overpressure corresponding to 400 psi is assumed for this scenario. The temperature at the bottom of the fault is 320.15K and the pressure is 12.56 MPa (1823.5 psi). The fault is assumed to be at residual water saturation. This will allow for the maximum possible flux during leakage. Corey-type function is used to estimate relative permeability of the liquid and gas CO_2 phases as shown in Figure 3.3 and the values used are given in Table 3.1.

The fault is discretized into 100 layers. The simulation time is 9 years. The CPU time for this simulation was 21 hours. For this particular combination of initial conditions and permeability, the first major conclusion is that there is strong cooling effect as the CO_2 leaked. Because of this cooling, CO_2 liquid condensed and subsequently evaporated with the heat from the rock and surroundings. The second major conclusion is that this interaction between phase changes and heat transfer led to cyclic variations in leakage mass flux and other parameters such as temperature, saturations etc. Description of this behavior is presented below.

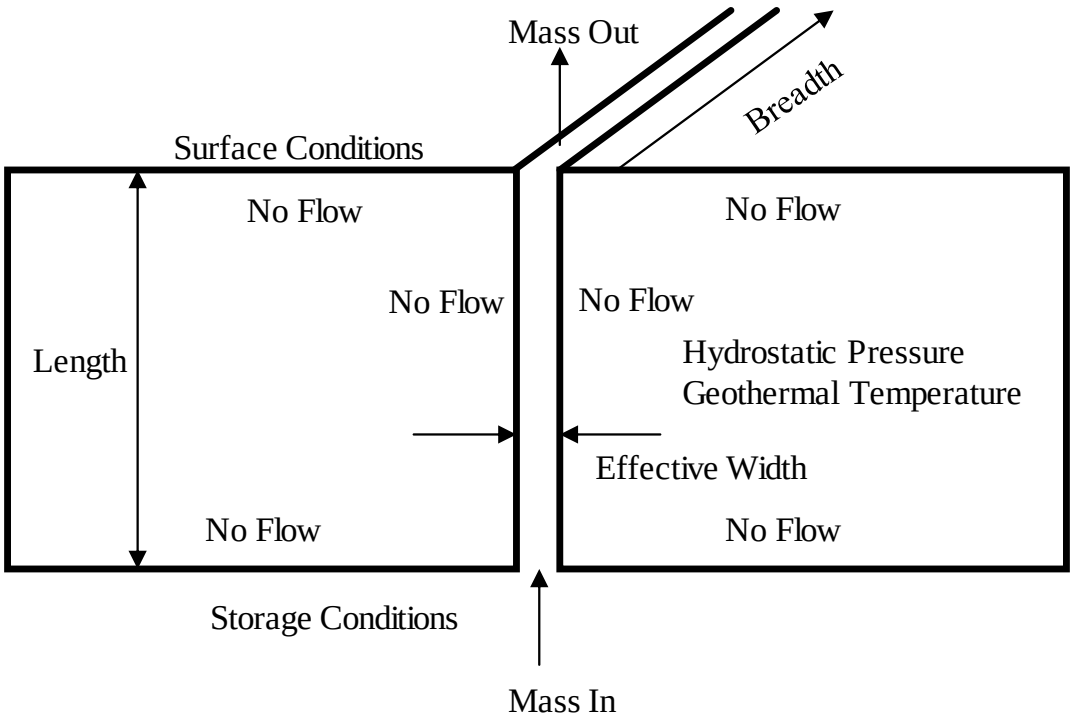

Figure 3.1: Schematic representation of the fault-leakage scenario used for example simulation

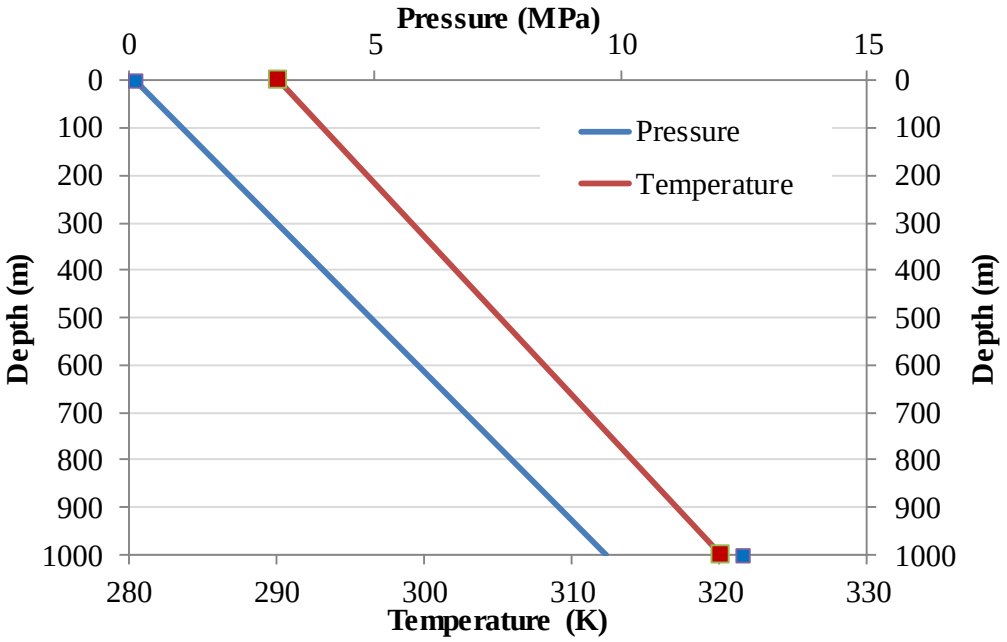

Figure 3.2: Initial pressures in the fault and initial temperatures in the fault and the surroundings as function of depth. The boundary conditions at the top and bottom of the fault is shown as box marker.

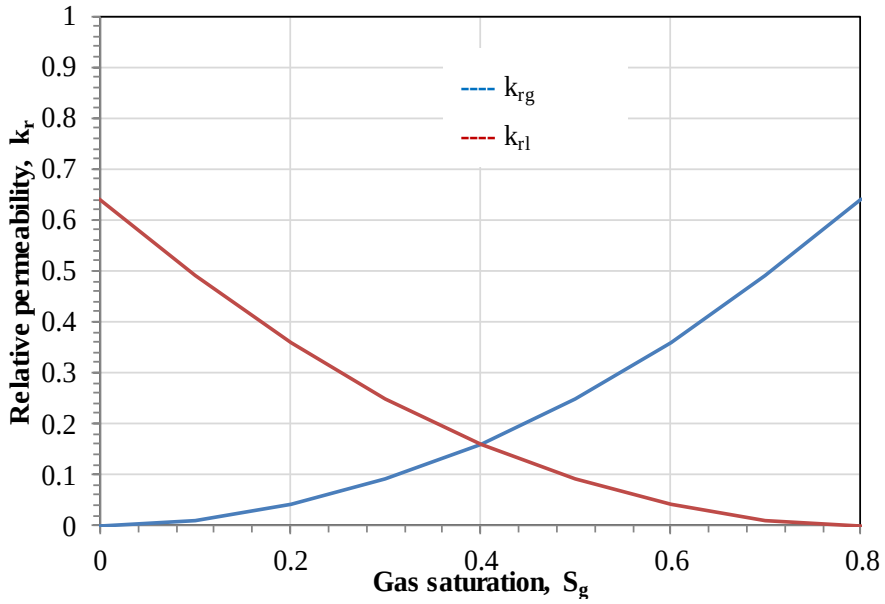

Figure 3.3: Corey type functions for gas phase CO_2 and liquid phase CO_2 relative permeability

Table 3.1 Parameters used in the fault leakage scenario

Parameters	**Values**
Geological Description	
Fault porosity, φ	0.3
Fault effective width (m)	0.1
Fault breadth (m)	10.0
Fault length (m)	1000
Permeability, k (md)	1000
Thermal Properties	
Thermal conductivity, λ (W/m/K)	2.5
Rock density, ρ_r (kg/m^3)	2650.0
Isobaric heat capacity of rock, C_r (kJ/kg/K)	0.9
Initial Conditions	
Surface temperature, T_{surf} (K)	290.15
Geothermal gradient (K/m)	0.03
Temperature at the bottom of fault, T_b (K)	320.15
Pressure at surface, P_{surf} (MPa) (psi)	0.10135 (14.7)
Pressure at the bottom of fault, P_b (MPa) (psi)	9.815 (1423.5)
Initial water saturation, S_w	0.2
Overpressure at the bottom of the fault, ΔP_s (MPa) (psi)	2.758 (400)
Relative permeability	
Residual gas saturation, S_{gr}	0.0
Residual water saturation, S_{wr}	0.2
Residual Liquid saturation, S_{lr}	0.0
Gas end point relative permeability, k_{rg}^o	0.64
Liquid end point relative permeability, k_{rl}^o	0.64
Liquid relative permeability exponent, n_l	2.0
Gas relative permeability exponent, n_g	2.0
Hydrate exponent for permeability reduction, n_h	3

Figure 3.4 and Figure 3.5 shows the pressure and temperature in the fault respectively, for three specific times before the gas-liquid co-existence along with the initial conditions in the fault. The leaking CO_2 transitioned into gas phase near its critical pressure at 760 m depth and remained as a gas phase until it reached the surface at t = 0 years in the absence of any overpressure at the fault inlet. This transition depth moved upwards to 530 m at 0.27 years as shown in Figure 3.4. This was primarily due to the overpressure at the fault inlet. The pressure increased at all depths compared to the hydrostatic pressure as shown in Figure 3.4. As shown in Figure 3.5, the first instance of gas-liquid coexistence occurred at 0.27 years when the temperature at 530 m decreased enough to reach the saturation condition for the pressure at that depth.

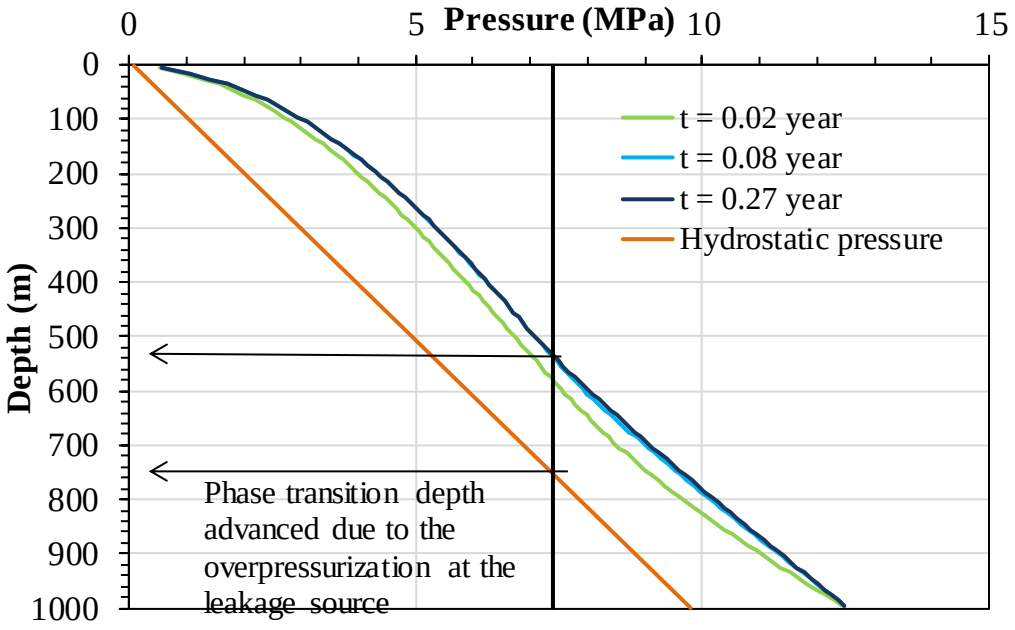

Figure 3.4: The pressure in the fault as a function of depth for three early times along with the hydrostatic pressure at that corresponding depth.

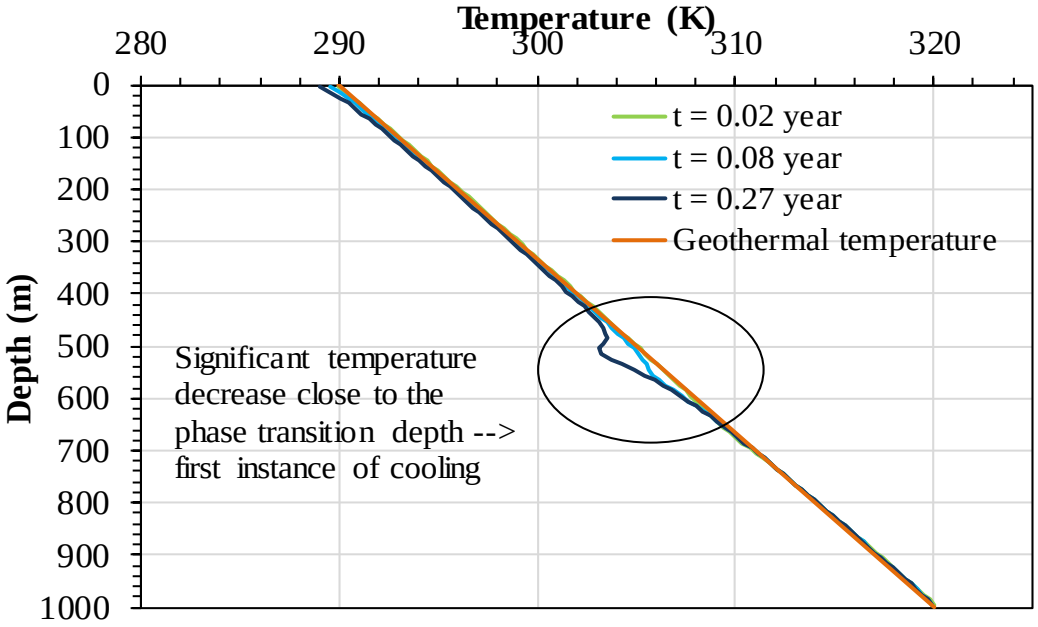

Figure 3.5: The temperature in the fault as a function of depth for three early times along with the geothermal temperature at that corresponding depth.

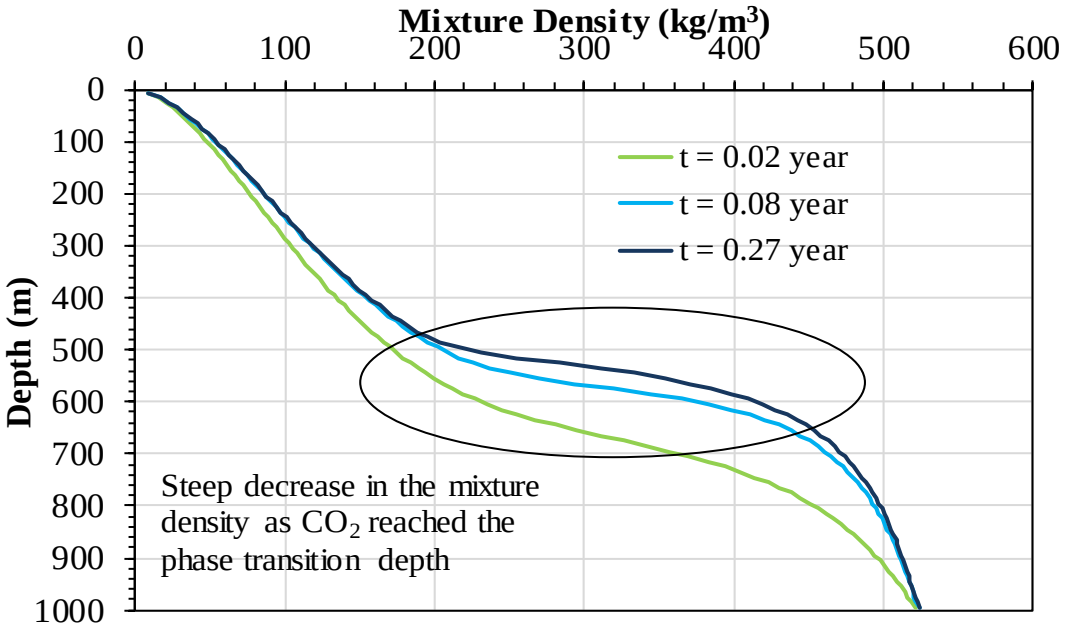

Figure 3.6: CO_2 mixture densities in the fault as a function of depth for 3 early times.

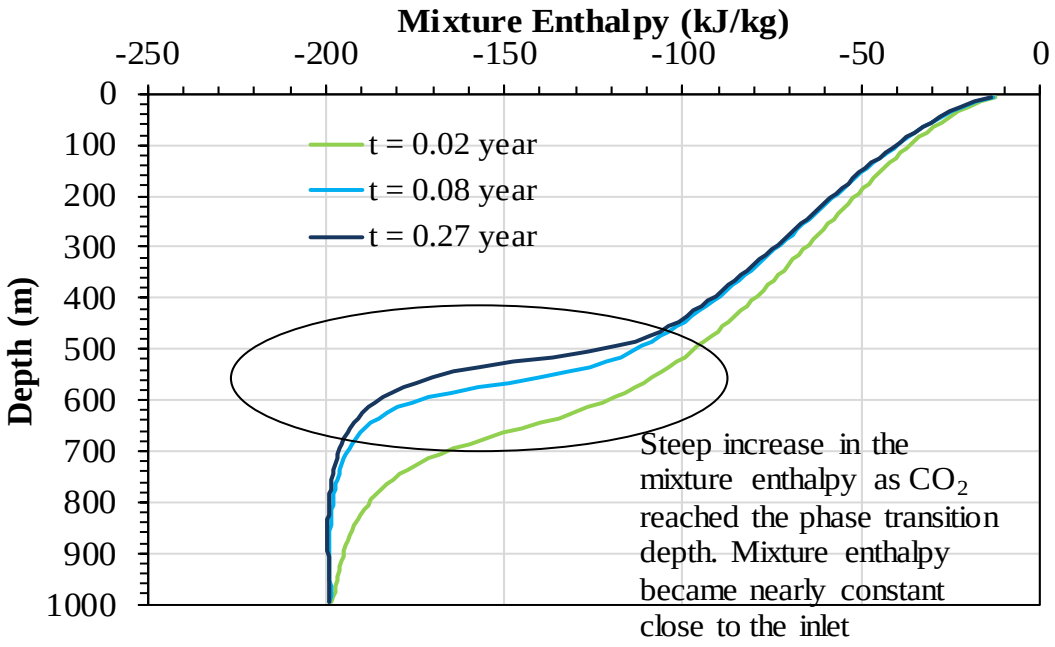

Figure 3.7: CO_2 mixture enthalpy in the fault as a function of depth for 3 early times.

The mixture density ($\rho_g S_g+\rho_l S_l$) increased at all depths with the increase in pressure in the fault as shown in Figure 3.6. The mixture enthalpy ($[\rho_g S_g(h_g-gz)+\rho_l S_l(h_l-gz)]/(\rho_g S_g+\rho_l S_l)$] increased from the fault inlet towards the surface as shown in Figure 3.7. The mixture enthalpy at the leakage source was low due to the overpressure at fault inlet. The leaking CO_2 underwent decompression between 500 m and 700 m as noted by the large decrease in mixture density and large increase in mixture enthalpy. The mixture enthalpy in the fault decreased at all depths with the increase with time as shown in Figure 3.7. CO_2 gained heat from the surroundings rocks at the immediate vicinity to increase the mixture enthalpy. After some time, the surroundings rocks cooled, which advanced the phase transition depths and caused the temperature between these depths to decrease as shown in Figure 3.5. The gas-liquid coexistence condition occurred at 530 m depth at 0.27 years. The mixture enthalpy reached near constant value from the fault inlet

until 700 m depth as shown in Figure 3.7. Similar decompressive expansion cooling was also observed at shallower depths (<100m) as shown in Figure 3.5 where the CO_2 gas expanded as denoted by the pressure decline in Figure 3.4.

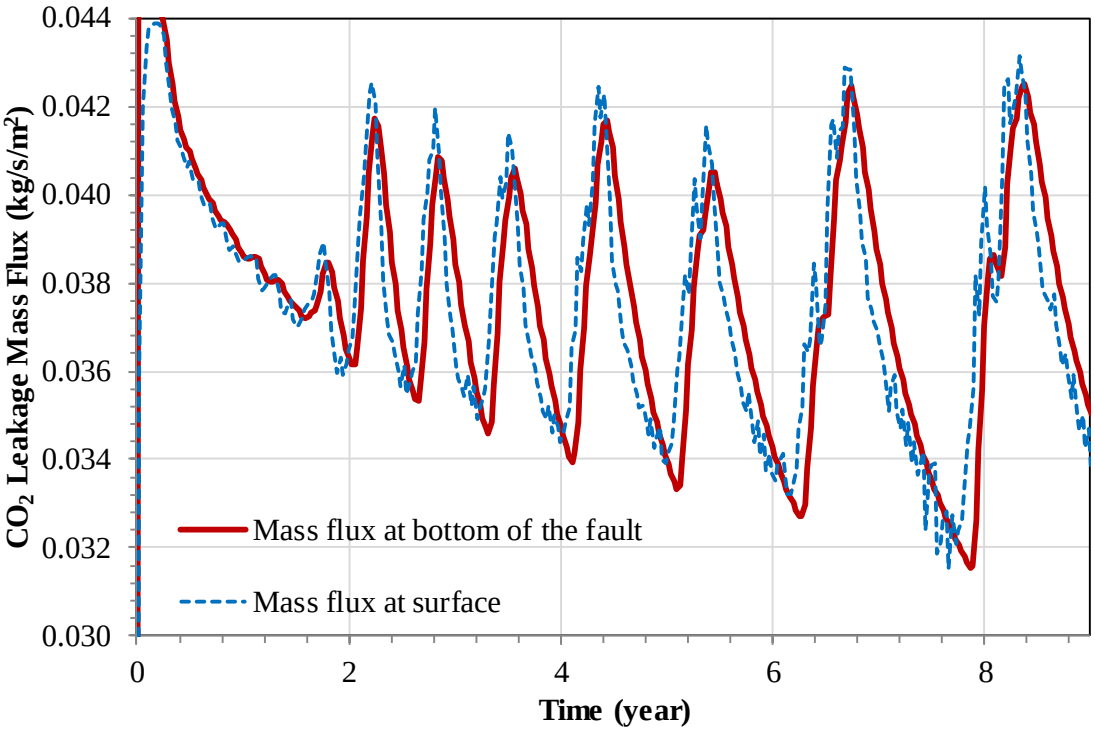

Figure 3.8: The cyclic nature of CO_2 leakage mass fluxes at the bottom and top of the fault as a function of time.

The leakage mass flux exhibited cyclic behaviour after the onset of of CO_2 gas-liquid coexistence as shown in Figure 3.8. At 0.27 years, the temperature at the transition depth declined enough to reach CO_2 saturation conditions which led to condensation of liquid CO_2 along with the already present gas CO_2 phase. The gas relative permeability decreased, the liquid relative permeability increased and the overall mobility decreased in this short two phase region. This decreased the leakage mass flux and the convective energy flux in the fault. Conductive heat from the immediate vicinity of this two phase

region evaporated most to all of the liquid phase. This evaporation increased the gas relative permeability, decreased the liquid relative permeability, increased the overall mobility and increased the leakage mass flux. This fluctuation in phase changes (gas to gas-liquid to gas) caused the fluxes to cycle after 0.5 years as shown in Figure 3.8, which led to cyclic variations in temperature, gas saturations and pressure, as shown in Figures 3.9, 3.10 and 3.11, respectively.

With each successive cycle, the heat to evaporate the liquid phase came from farther away from the fault thus increasing the time period of the cycles. The length of the two phase region increased at each time period which increased the amplitude of the cycles. The amplitude and time period of the cycles were small at early times and increased with each successive cycle. The two phase region of gas and liquid CO_2 is at its thickest at the trough of each cycle, as shown in Figure 3.10 and the temperature at the top of this region is at its lowest as shown in Figure 3.9. The two-phase region shrank and the respective temperatures increased at the crest of each cycle. The maximum temperature decrease and thereby the strongest cooling effect was observed at the top of the two-phase gas-liquid region where it transitioned into single phase gas region as shown in Figures 3.9 and 3.10, respectively.

The temperature at the top of the two-phase region decreased enough to reach hydrate formation conditions at 7.7 years as shown in Figures 3.12 and 3.14, respectively. Formed hydrates reduced the permeability by 49 % in the hydrate regions. This increased the amplitude of the cycles and decreased the flux. The saturation profiles of this particular cycle along with the corresponding T-P profile are shown in Figure 3.13. The T-P profile tracked the saturation curve when the two phase region was at its thickest at the trough of the cycle. The T-P profile moved slightly away from the saturation curve when the two-phase region shrank at the crest of the cycle. During hydrate formation, the

T-P profile tracked the saturation curves beyond the hydrate formation curve when it returned to the trough of the cycle.

The flux at the top of the fault reached a maximum value of 0.044 kg/s/m^2 when all the regions in fault contained only single phase. Formed hydrates reduced the permeability by 49% in the hydrate regions. Although the permeability reduced, it affected only the depths at which hydrates were present and did not have significant effect on the leakage mass flux. The flux will decrease more with the increase in water saturation and increase in the length of hydrate regions. The flux at the top of the fault at the first instance of hydrate formation was 0.032 kg/s/m^2 which indicated a decrease of 28% from the maximum value due to multiphase coexistence and hydrate formation.

The leakage mass flux through a fault of 1000 md permeability were calculated to be 0.044 kg/s/m^2 or 1,387,584 kg/yr/m^2 (maximum) and 0.032 kg/s/m^2 or 1,009,152 kg/yr/m^2 (multiphase coexistence and hydrates). Leakage mass flux is expressed independent of the area. Taking the area (0.1*10 m^2) into account, the leakage rate is approximately 1387 tonnes/yr and 1009 tonnes/yr. In the context of long term risk assessment, this leakage rate for 100 years would yield 0.138 and 0.1 million tonnes of escaped CO_2, approximated to 0.7% and 0.5% for a typical 20 million tonnes of stored CO_2, well below the 1% target. This result is sensitive to the flow area of the fault and attenuation to intersecting permeable layers. Observations from natural analogues suggest that the cross-sectional area of the leaking CO_2 increases near the surface. Thus the near-surface fluxes of CO_2 would be much smaller than our calculated fluxes along the faults.

For comparison, the leakage mass flux from natural analogues discussed in Chapter 1 range between 1.25 x 10^{-3} and 5.78 x 10^{-5} kg/s/m^2 and the CO_2 background flux at earth's surface is up to 2 x 10^{-7} kg/s/m^2 (Allis et al., 2005). The computed fluxes are well above the values mentioned here but the leakage area of the natural analogues is

large with a maximum of 500,000 m^2 (Lewicki et al., 2007). The intention here is to set the calculated fluxes in context with naturally occurring fluxes and not to comment on whether the values are large or small enough to neglect compared to naturally occurring fluxes. This context provides the confidence that the leaks can be identified during monitoring.

Additional insights in the system behaviour with respect to the pressure and temperature signals during leakage are obtained when the pressure and temperature profile evolution shown in Figures 3.9, 3.11 and 3.12 are examined. The pressure increased at every depth when compared to the hydrostatic pressure of that corresponding depth and there is significant temperature decrease in the multiphase regions between 200-600m and close to the surface. The maximum temperature decrease at each time occurred at the top of the two phase region with close to 15 K decrease occurred at the hydrate formation depth as shown in Figure 3.12. There is associated temperature decrease farther away from the fault in these depths since heat was taken from these regions to evaporate liquids and melt hydrates. Hence, observation wells, monitoring stations, pressure and temperature monitoring of these regions can help at quick identification of leakage.

For this combination of initial conditions and permeability, there is strong cooling effect in the fault and the CO_2 leakage mass flux exhibited cyclic behavior after the onset of CO_2 gas-liquid coexistence. The cyclical behavior is due to the coupled effects of heat transfer with the surroundings, thermodynamic characteristics of the leaking CO_2 and multiphase aspects of flow during leakage. Several factors such as the geometric properties of the fault, boundary conditions at the source, permeability of the fault among others will have major effect on the extent of this cyclic behavior. They ae investigated in the following sections.

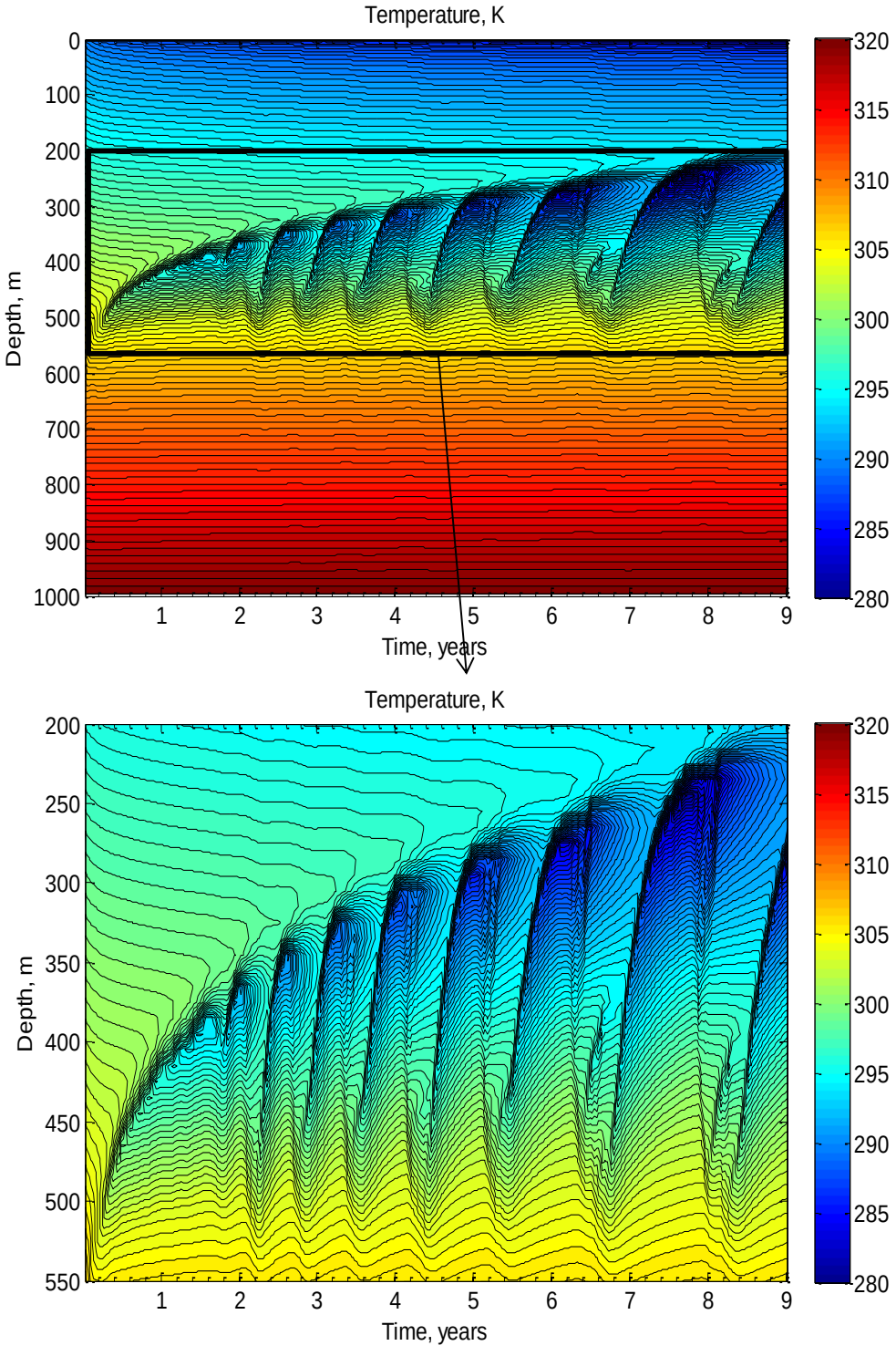

Figure 3.9: Temperature profile evolution with time.

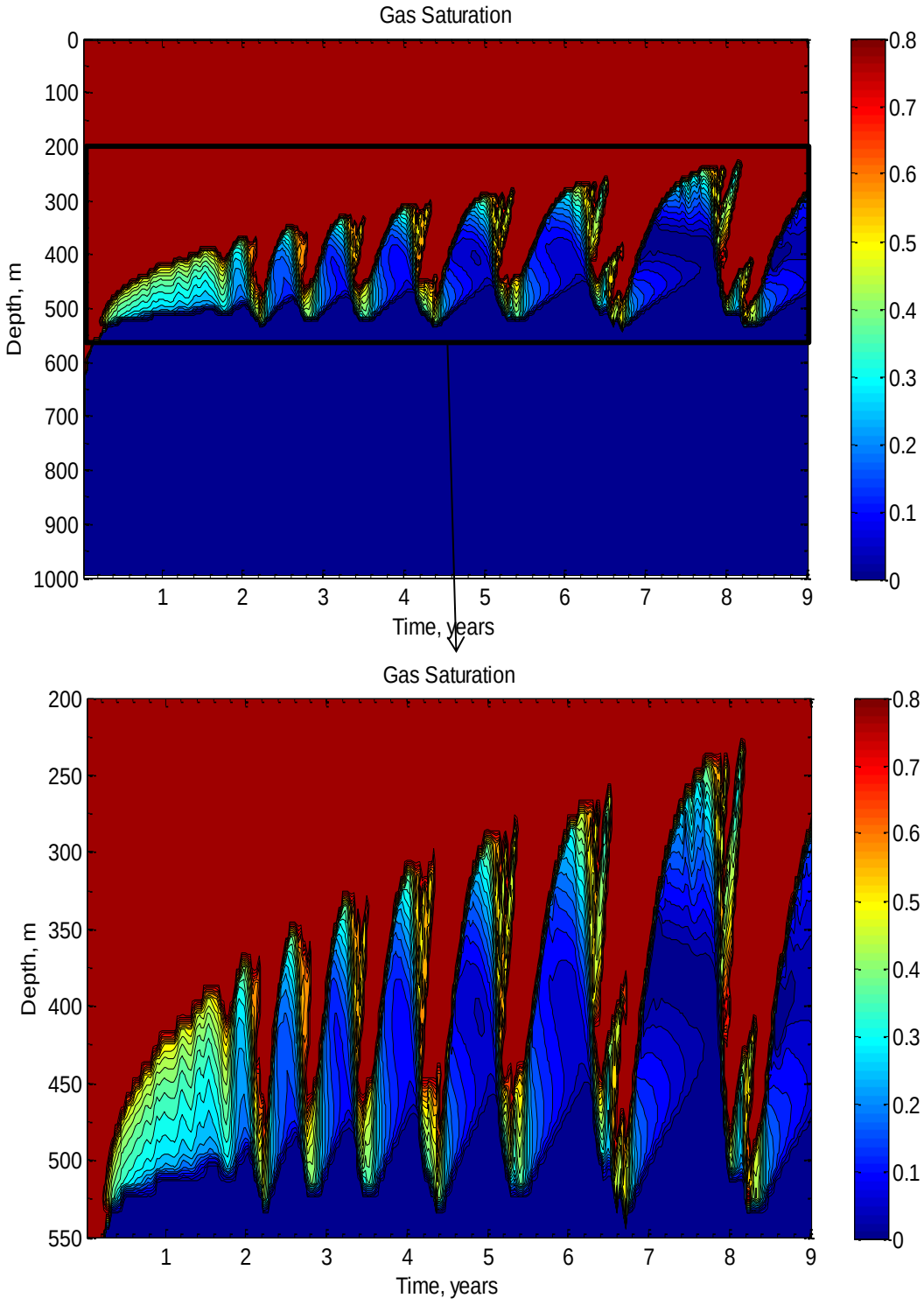

Figure 3.10: Gas saturation profile evolution with time.

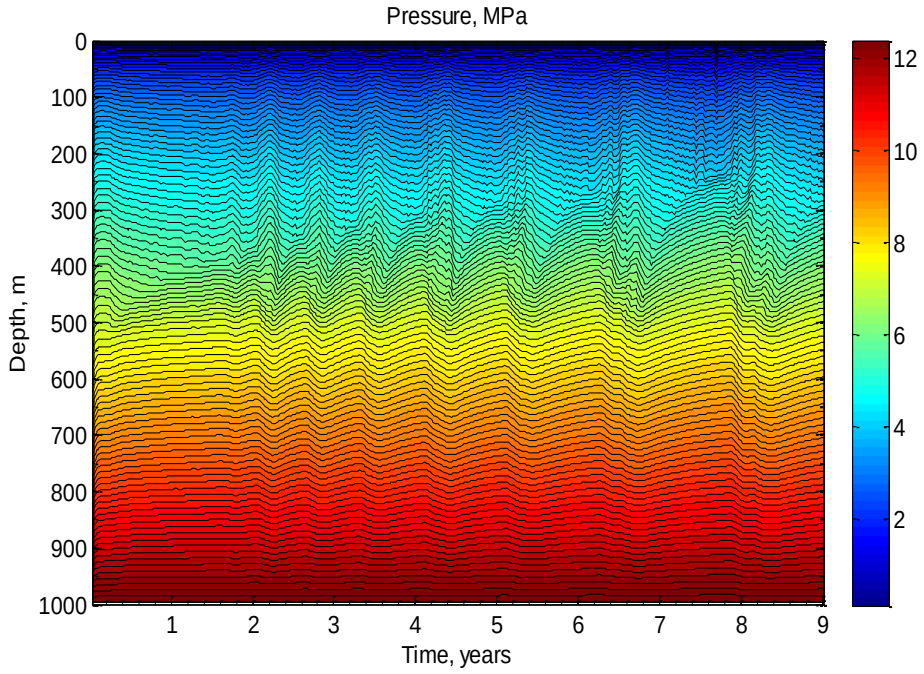

Figure 3.11: Pressure profile evolution with time.

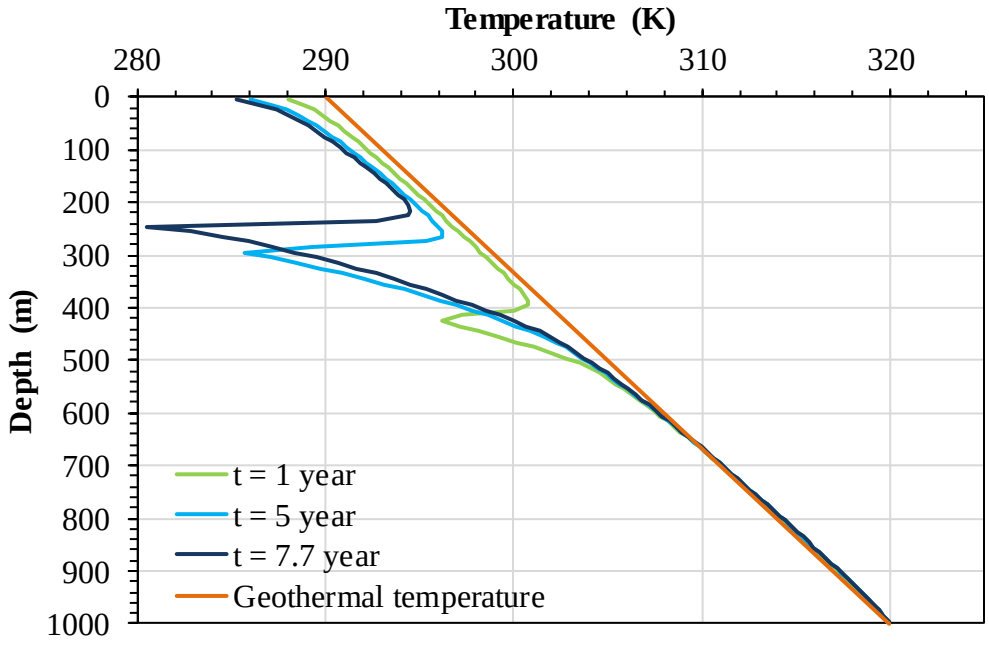

Figure 3.12: temperature in the fault as a function of depth for three different times.

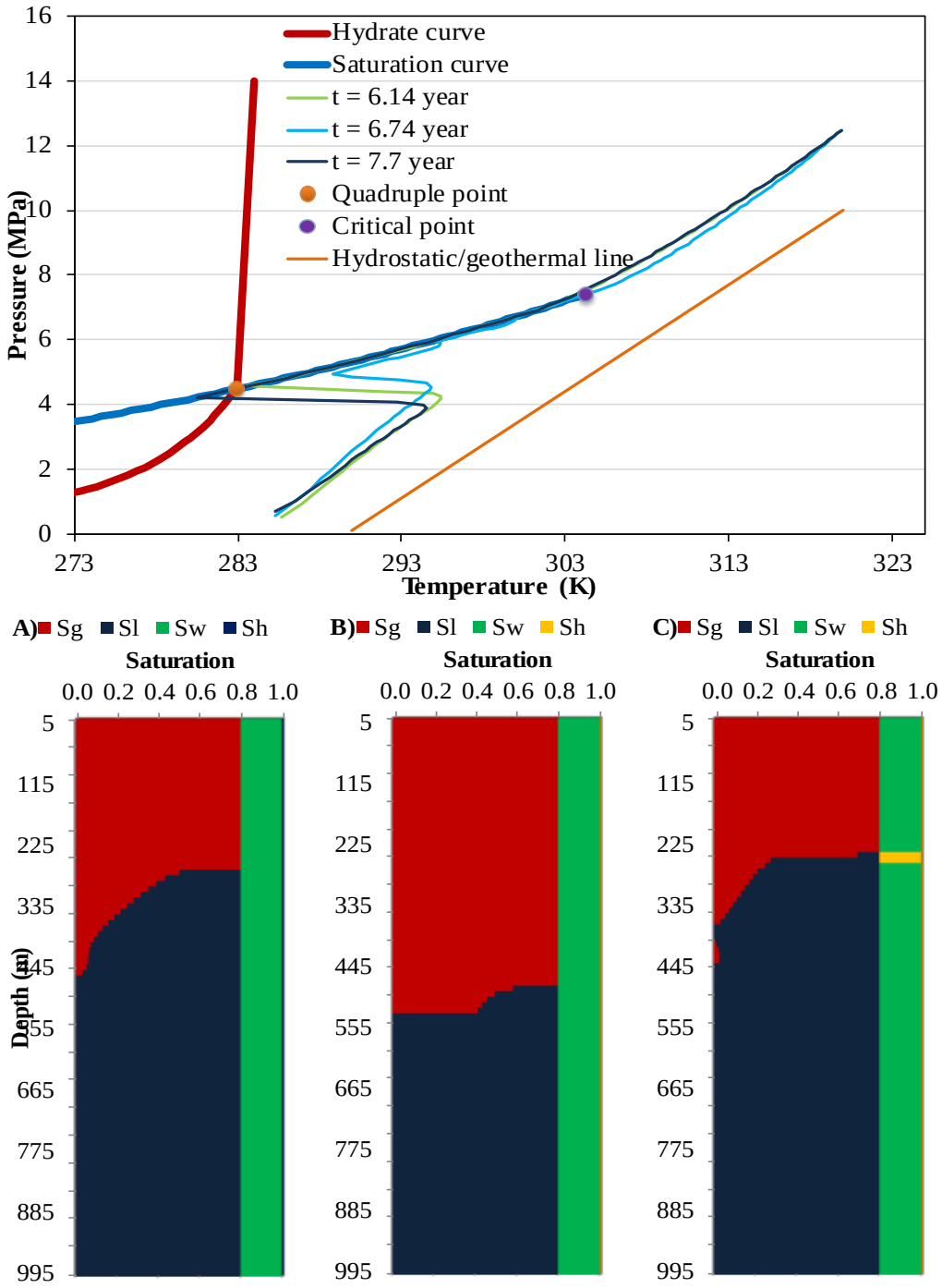

Figure 3.13: a) Pressure-Temperature profiles at three different times. The phase diagram is similar to Figure 3.13, b) the saturation profile in the fault for three different times.

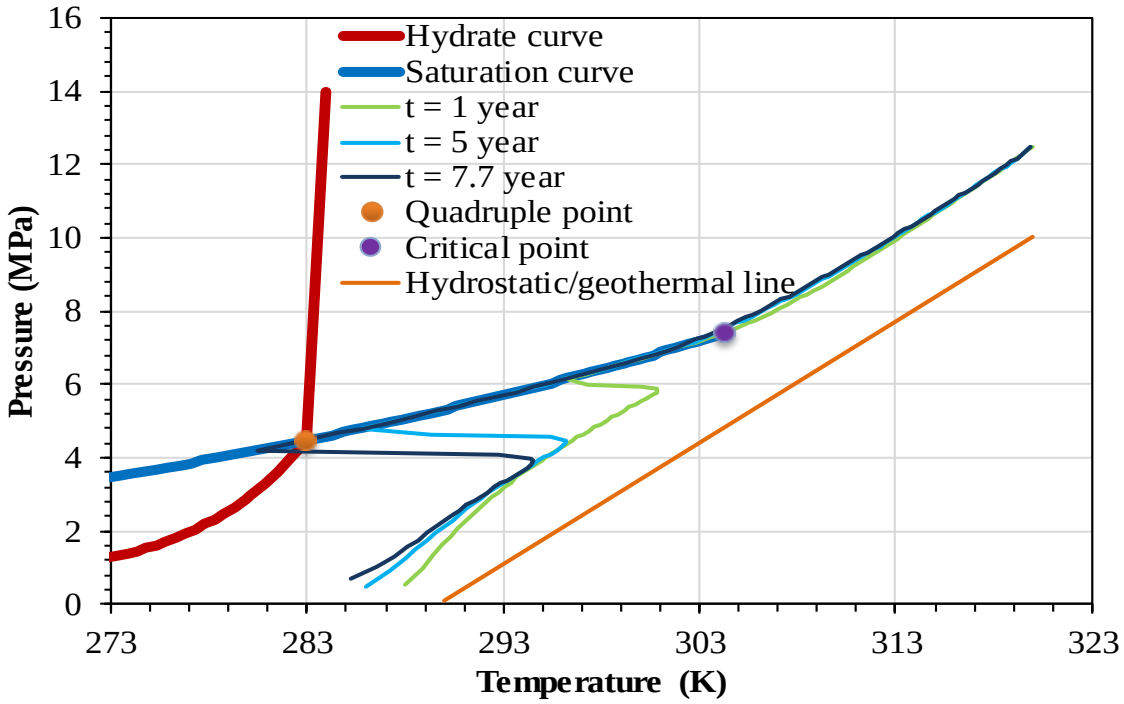

Figure 3.14: Pressure-Temperature profiles at three different times. The blue curve is the CO_2 saturation curve and the red curve is the hydrate formation curve. Orange circle is the quadruple point of the CO_2-H_2O mixture and the purple circle is the critical point of CO_2. The orange line is the pressure-temperature line calculated with hydrostatic and geothermal gradient.

3.3 Influence of Storage Reservoir Pressure Conditions on Leakage

The pressure in the reservoir increases during injection assuming no production or leakage. This pressure increase is called overpressure. Besides providing a driving force, the overpressure will also affect the cyclic nature of leakage. Calculations are performed for a wide variety of overpressure scenarios keeping all other parameters same as the example fault-leakage scenario. The goal of this analysis is to quantify the effect of overpressure on leakage mass flux, the cyclical nature of leakage and the time taken for the first instance of gas-liquid coexistence and hydrate formation.

3.3.1 Constant Reservoir Overpressure

Numerical simulations were performed for overpressures from 10 to 400 psi at the base of the fault and the results are discussed in this section. The overpressure is kept constant throughout the course of the simulation. The maximum leakage mass flux at any time in the fault and the leakage mass flux at the first instance of hydrate formation are shown in Figure 3.14. Leakage mass fluxes increased with increase in overpressure with nearly 29% increase at overpressure of 400 psi when compared with 10 psi overpressure scenario. The mass flux decreased 30% for all overpressure cases at the first instance of hydrate formation due to multiphase coexistence and hydrates. Hence, the overpressure at the fault inlet does not have significant impact on the magnitude of leakage mass flux. Besides the concerns about unintended fracturing, a higher rate of injection increases overpressure and consequently the leakage mass flux. It is preferable to inject slower and longer than faster and shorter when concerned about the minimization of leakage mass flux. Thus, reservoir pressure management plays an active role in minimizing leakage mass flux.

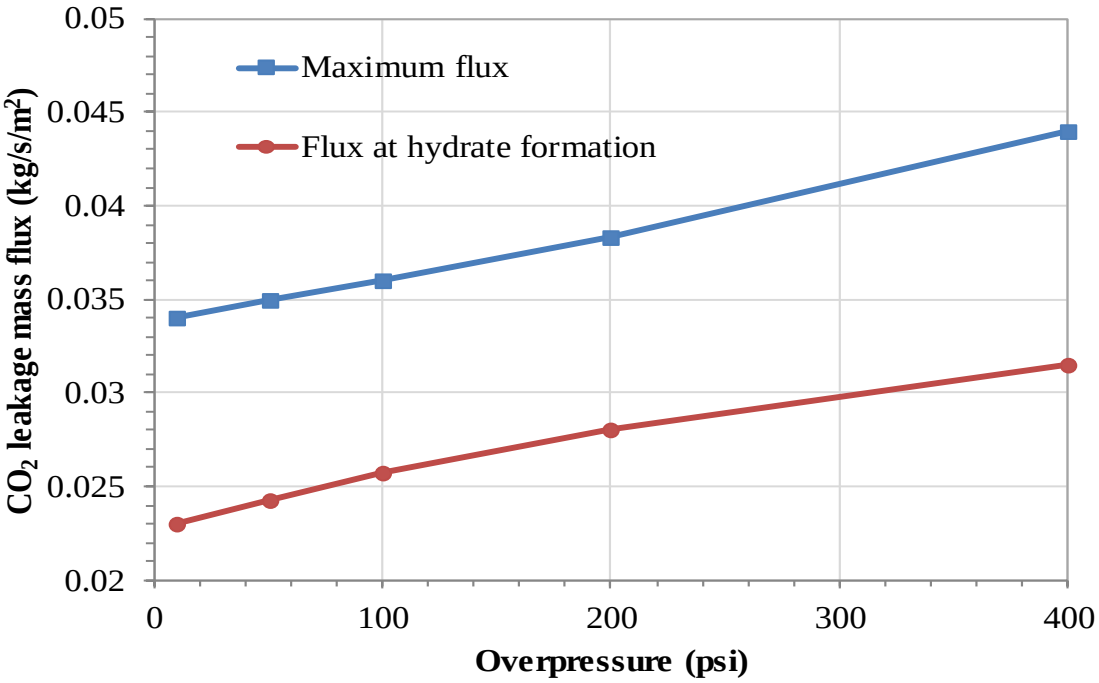

Figure 3.14: The maximum flux and flux at hydrate formation as a function of overpressure for 5 overpressure scenarios.

Figure 3.15 through 3.18 shows the leakage mass flux at the bottom and top of the fault for all the overpressure scenarios. Although at different timescales, the leakage mass fluxes exhibited cyclic behavior for all the overpressure scenarios as illustrated in Figures 3.15 through 3.18. The amplitude and time period of each flux cycle increased with each successive cycle for all the overpressure scenarios similar to the example leakage scenario. The leakage mass fluxes had a period of constant discharge until the first instance of multiphase coexistence. This period of constant discharge decreased with the increase in overpressure. The number of cycles the fluxes underwent increased and the time period of the cycles decreased with the increase in the overpressure. The strongest cooling effect is observed at the top of the two-phase gas-liquid region where it

transitioned into single phase gas region and at regions close to the surface at late times as shown by the temperature profile evolution with time in Figures 3.19 through 3.22.

Although the leakage mass flux did not have a significant increase with increase in overpressure, the time taken for the first instance of gas-liquid coexistence and the first instance of hydrate formation decreased exponentially with an increase in overpressure as shown in Figure 3.23. This could be explained with the help of the mixture density and mixture enthalpy for overpressure scenarios at the time of first instance of gas-liquid coexistence as shown in Figures 3.24 and 3.25, respectively. The mixture density increased and the mixture enthalpy decreased at the fault inlet with the increase in overpressure. The magnitude of mixture enthalpy gain near the phase transition depth increased with increase in overpressure. Hence, more heat was taken from the surrounding rocks at higher overpressures, which led to significant cooling, enough to reach gas-liquid coexistence at early times. With the decrease in overpressure, the magnitude of the enthalpy gain decreased, which shrank the temperature decrease and increased the time taken to attain gas-liquid coexistence.

Figures 3.26 and 3.27, respectively, show the pressure and temperature in the fault for overpressure scenarios at the time of first instance of gas-liquid coexistence. The pressure in the fault increased with increase in overpressure and the temperature in the fault decreased significantly at late times for low overpressures. Although the leakage mass flux was higher for higher overpressures, the increased pressures and larger temperature decrease will increase the likelihood of early detection of leaks. With the increase in time, the temperature in the fault decreased significantly enough to reach hydrate formation conditions as shown in Figure 3.28. The T-P profile in the fault at the first instance of hydrate formation was shown in Figure 3.29. The depth of first instance of hydrate formation advanced higher with the increase in overpressure.

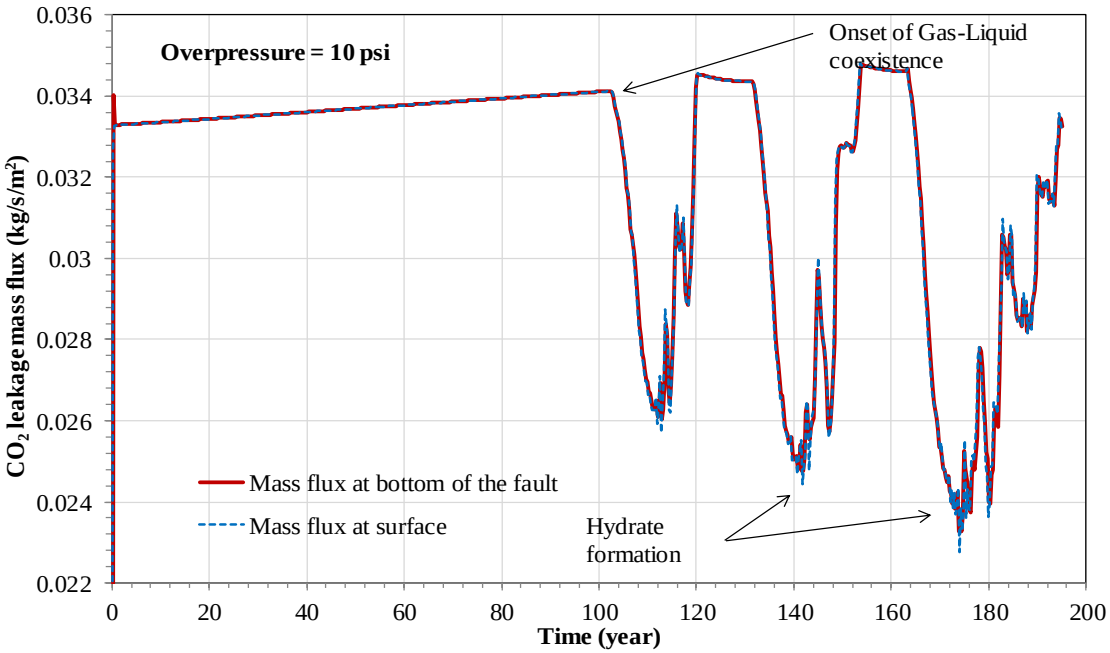

Figure 3.15: The CO_2 leakage mass fluxes at the bottom and top of the fault as a function of time for ΔPs = 10 psi.

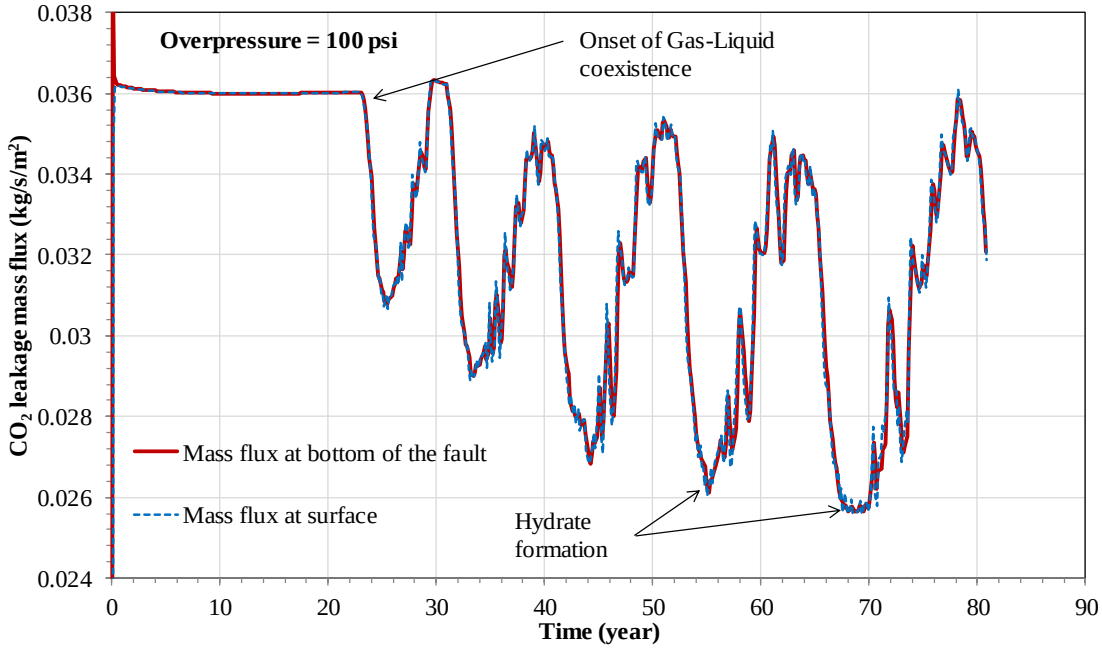

Figure 3.16: The CO_2 leakage mass fluxes at the bottom and top of the fault as a function of time for ΔPs = 100 psi.

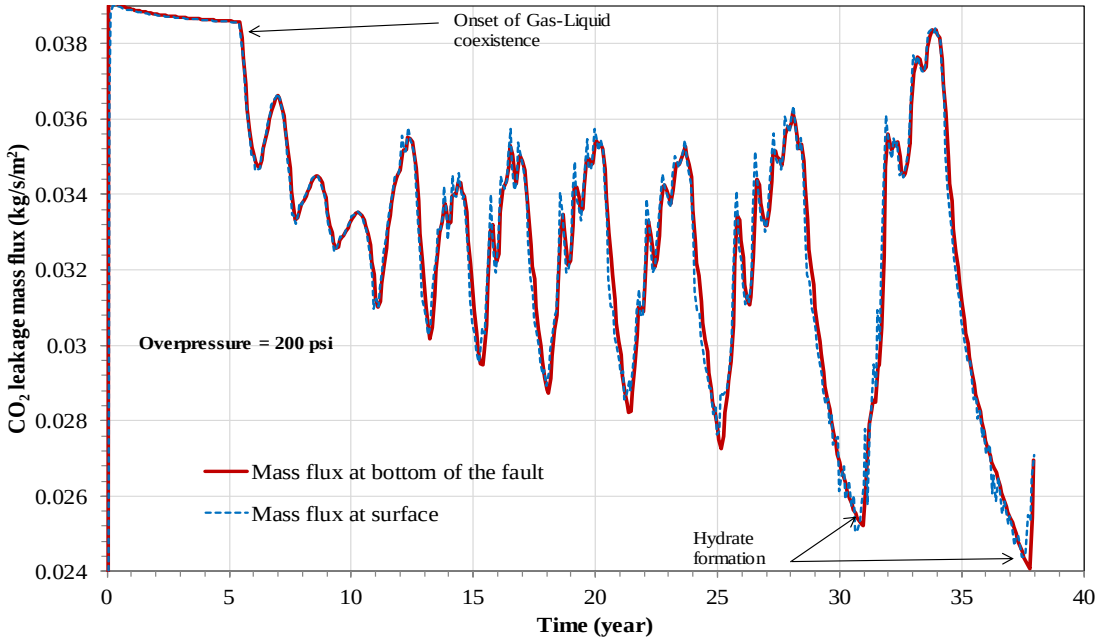

Figure 3.17: The CO_2 leakage mass fluxes at the bottom and top of the fault as a function of time for ΔP_s = 200 psi.

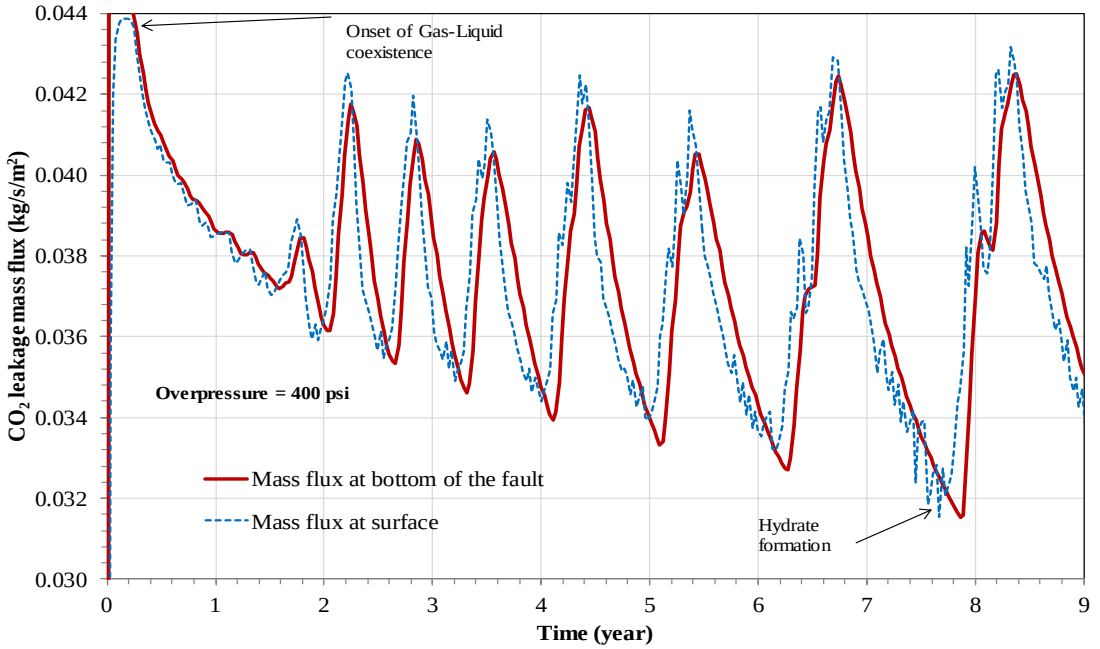

Figure 3.18: The CO_2 leakage mass fluxes at the bottom and top of the fault as a function of time for ΔP_s = 400 psi.

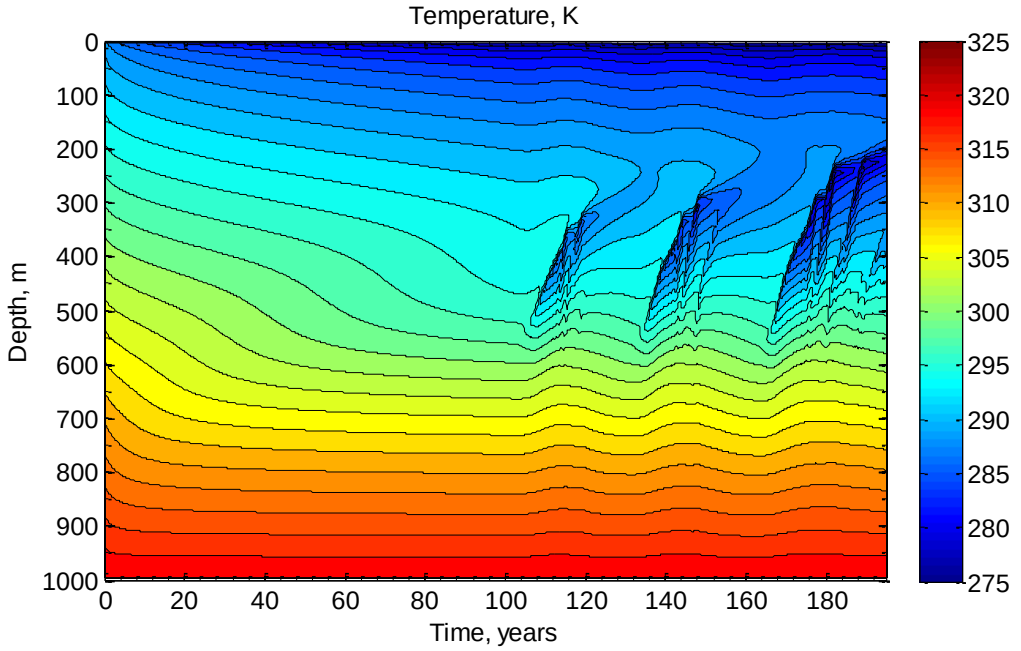

Figure 3.19: Temperature profile evolution for overpressure = 10 psi.

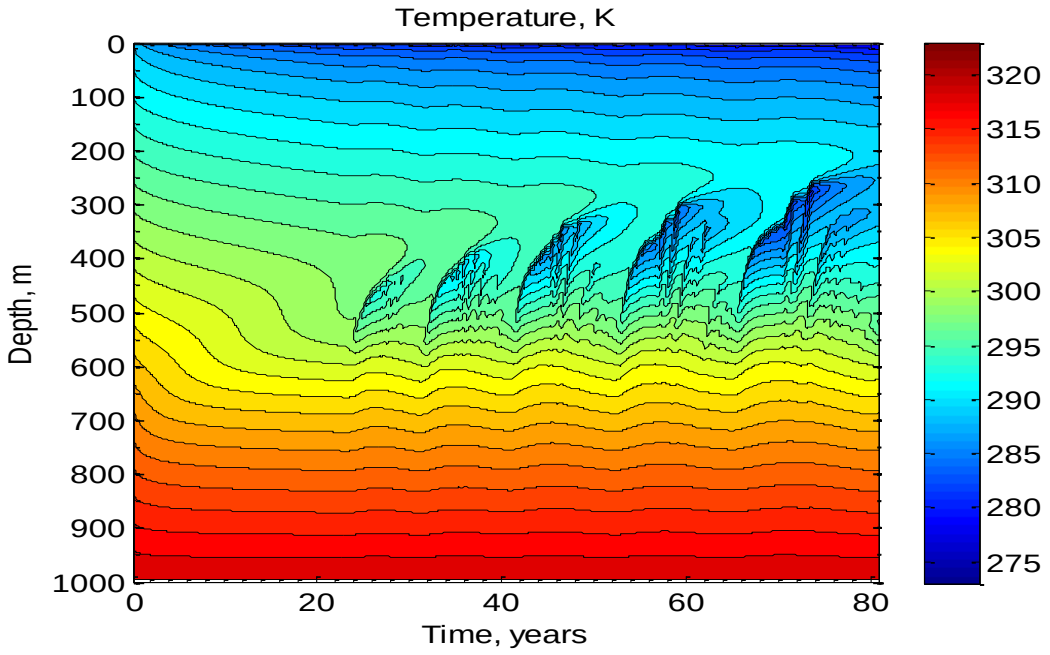

Figure 3.20: Temperature profile evolution for overpressure = 100 psi.

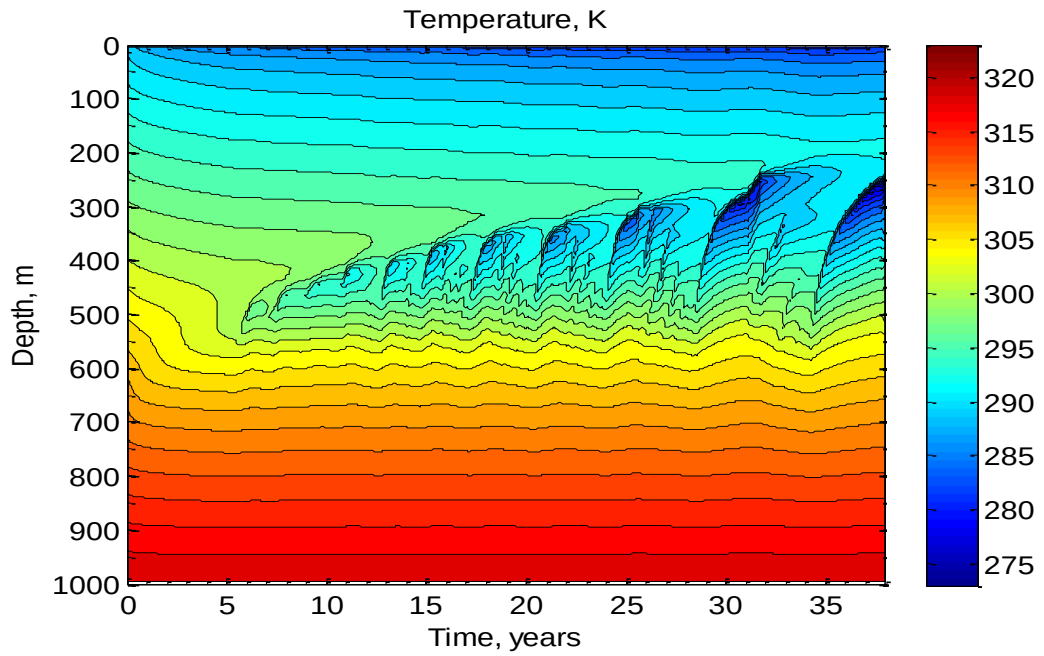

Figure 3.21: Temperature profile evolution for overpressure = 200 psi.

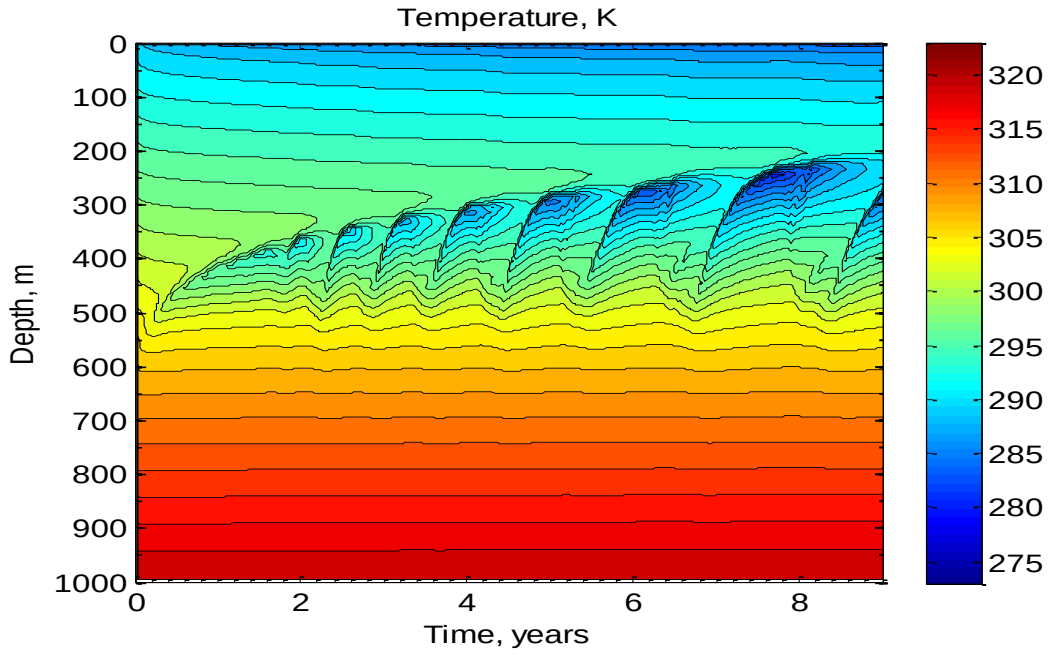

Figure 3.22: Temperature profile evolution for overpressure = 400 psi.

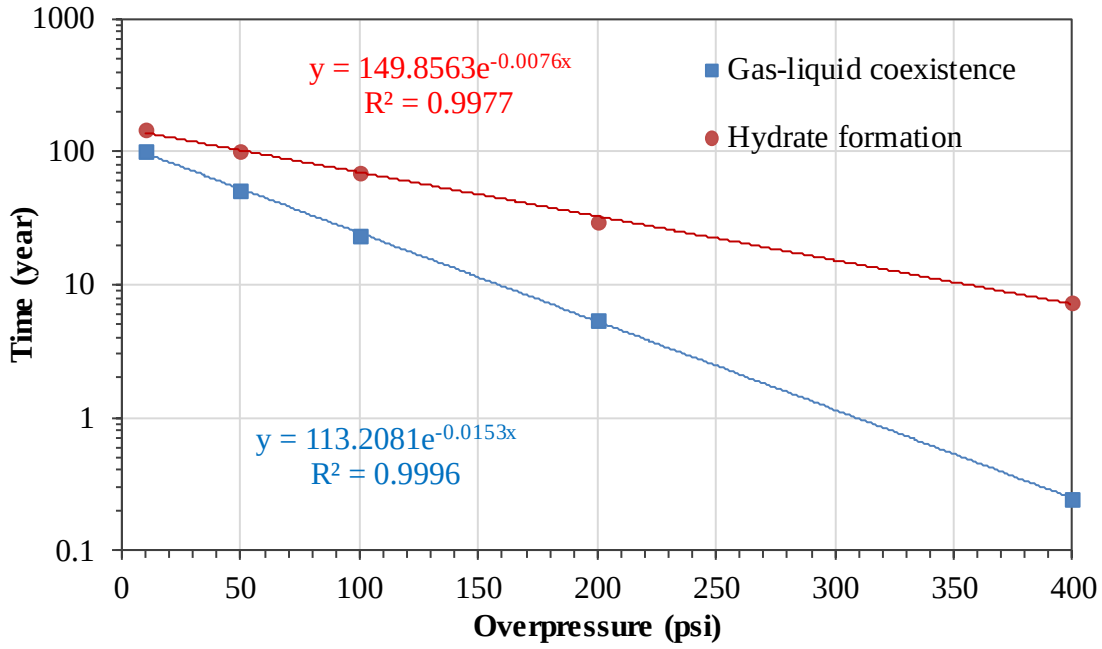

Figure 3.23: Time taken for the first instance of gas-liquid coexistence and hydrate formation as a function of overpressure for different overpressure scenarios.

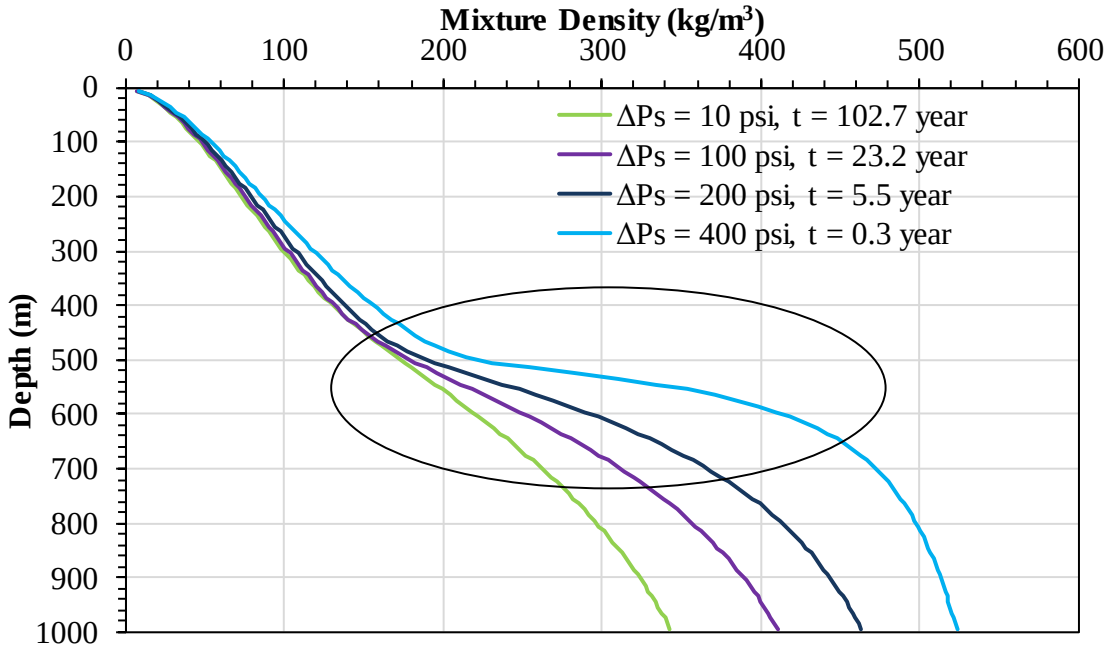

Figure 3.24: CO_2 mixture density in the fault as a function of depth for different overpressure scenarios.

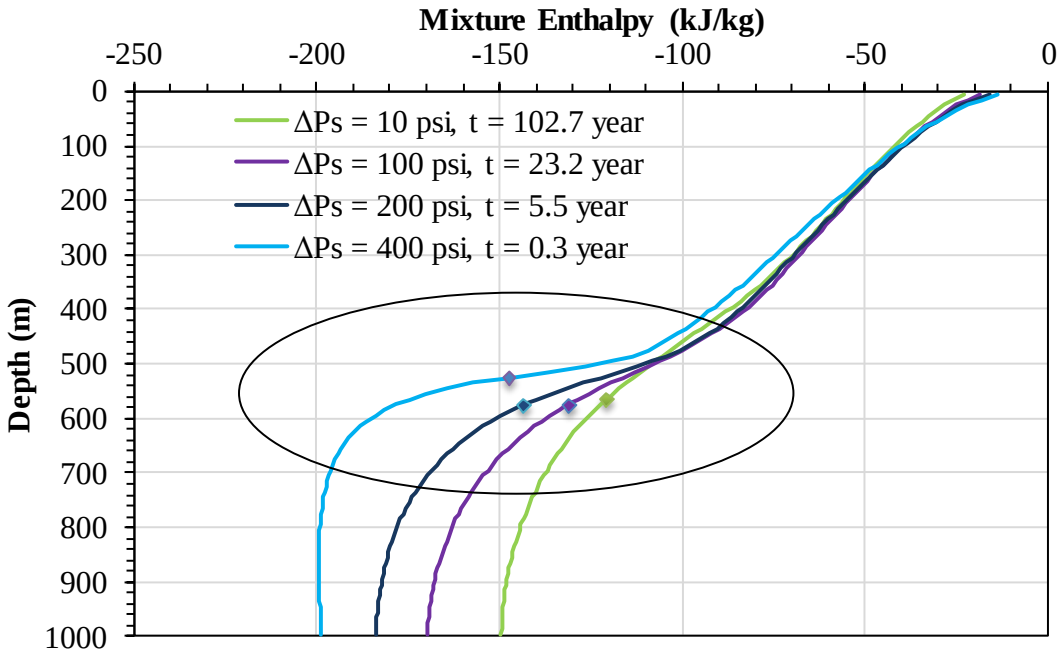

Figure 3.25: CO_2 mixture enthalpy in the fault as a function of depth for different overpressure scenarios.

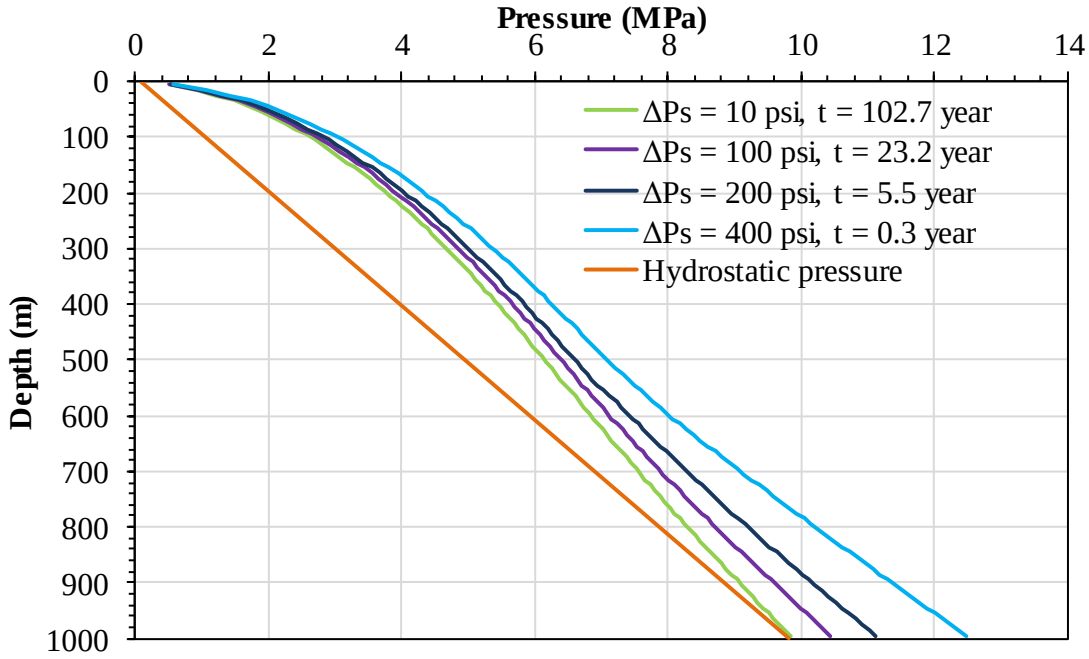

Figure 3.26: Pressure in the fault at the first instance of gas-liquid coexistence for different overpressure scenarios.

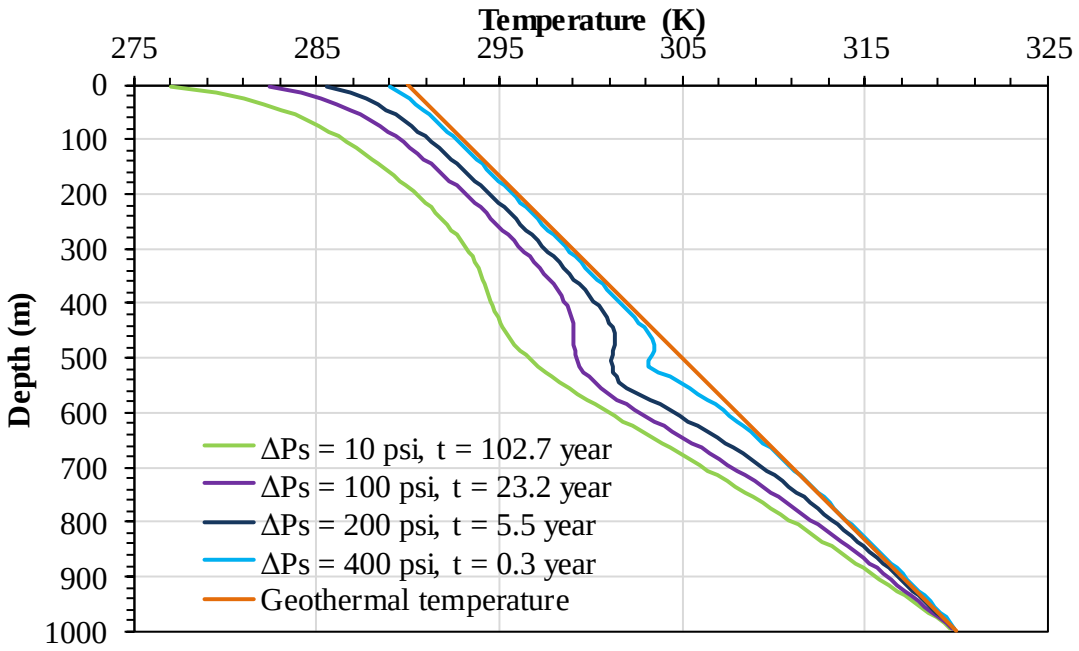

Figure 3.27: Temperature in the fault at the first instance of gas-liquid coexistence for different overpressure scenarios.

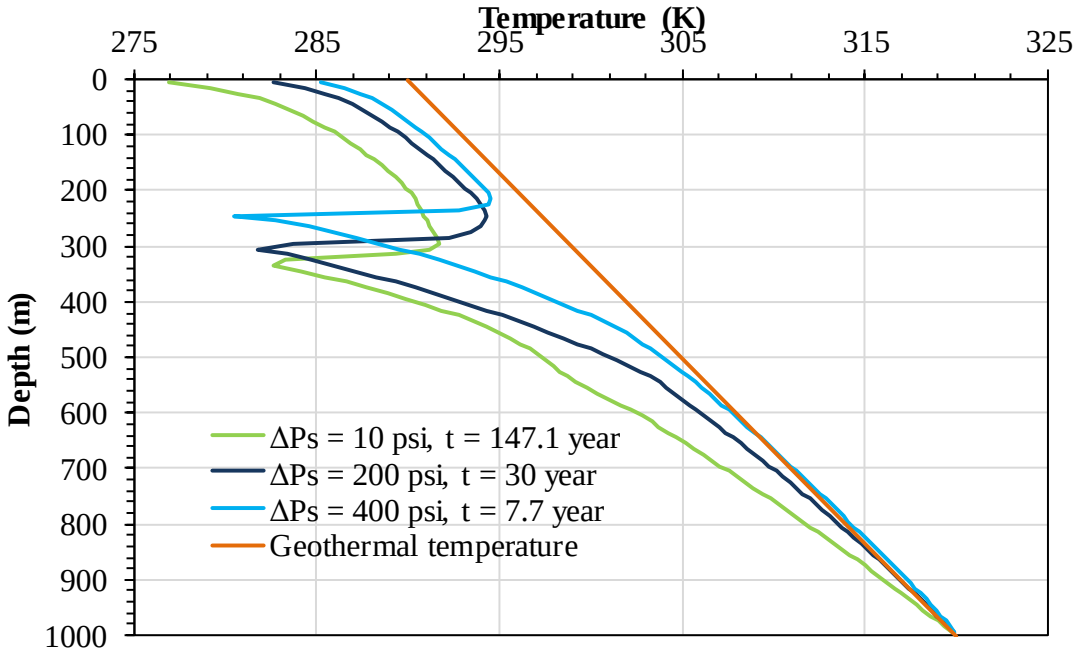

Figure 3.28: Temperature in the fault at the first instance of hydrate formation for different overpressure scenarios.

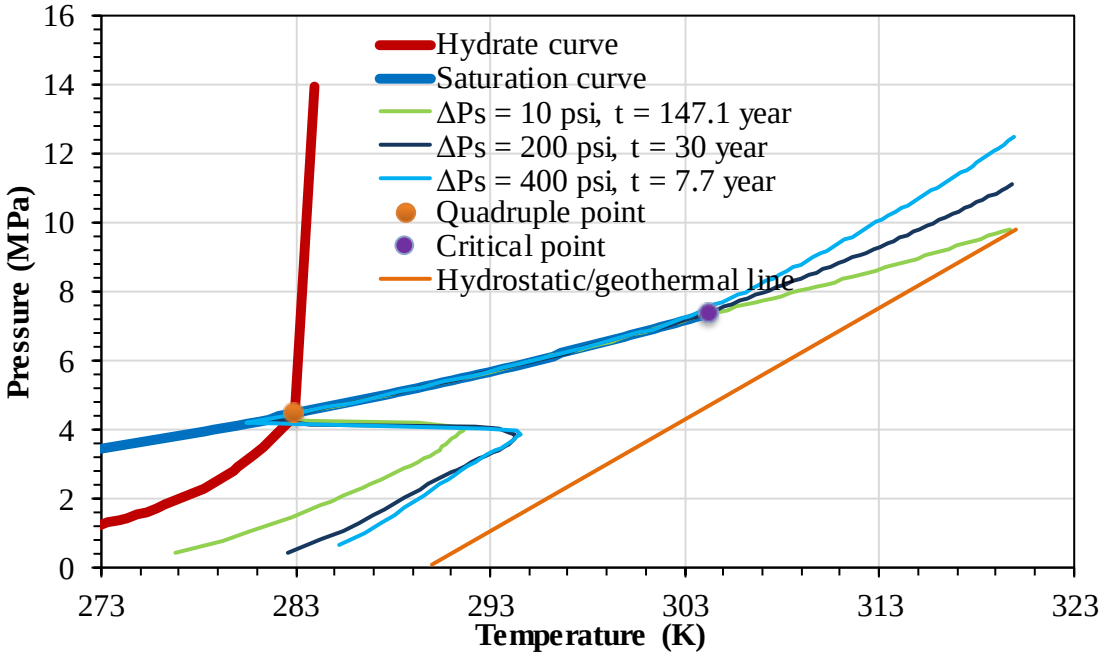

Figure 3.29: The Pressure-Temperature profile at three different overpressure scenarios. The blue curve is the CO_2 saturation curve and the red curve is the hydrate formation curve.

3.3.2 Time Varying Reservoir Overpressure

The overpressure at the base of the fault was kept constant for all the above scenarios. Although this analysis yielded several important observations with respect to its effect on leakage, the overpressure in the reservoir will change with the injection schedule in real-world scenarios. During injection, the reservoir is overpressured and reach a maximum pressure until the end of injection. Post injection, the pressure in the reservoir gradually declined towards the initial pressure at late times. A similar situation was used to estimate its effect on leakage. Figure 3.30 shows the reservoir pressure as function of time for this simulation. At t = 0 years, the reservoir is assumed to be at hydrostatic pressure. During the injection phase (0-5 years), the pressure reached a

maximum value in 1 year and it was maintained at this maximum pressure till the end of injection. The pressure gradually declined towards the initial pressure at late times.

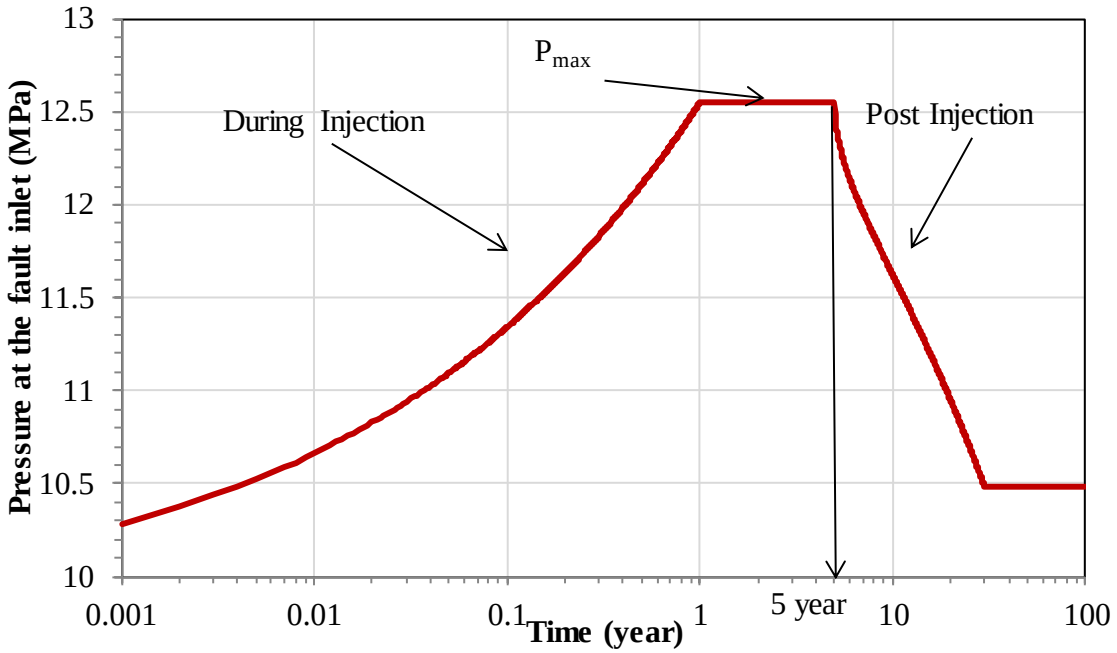

Figure 3.30: Pressure at the fault inlet as a function of time

The leakage mass flux at the bottom and top of the fault is shown in Figure 3.31. The flux showed similar cyclic behavior to the example leakage scenario with an overpressure of 400 psi during the injection phase (5 years). The first instance of gas-liquid coexistence was observed around 0.6 years. The length of the two phase region and the extent of cooling increased once the inlet pressure reached the maximum value 1 year and injection stoppage at 5 years as shown by the corresponding T-P line in Figure 3.32. The decline in the inlet pressure post-injection had a significant effect on the cyclic behavior of the fluxes. The amplitude decreased and the time period increased with successive cycles until 11 years. The flux became monotonic at 30 years. The entire fault was in single phase conditions as shown by the T-P line in Figure 3.32. The second onset

of gas-liquid coexistence occurred at 38 years. The flux exhibited different cyclic behavior with larger time periods than one exhibited at early times. The first instance of hydrate formation occurred at 67 years as shown by the T-P line in Figure 3.32. The time period and the amplitude of the fluxes increased further post hydrate formation.

The cooling effect was quickest and the fluxes cycled with shorter time period during the injection phase due to the higher pressure in the fault inlet. Hence multiphase coexistence effects on the flux were greatest during the injection phase. The flux at the crest of the cycle, trough of the cycle and the maximum flux decreased with the decrease in inlet pressure.

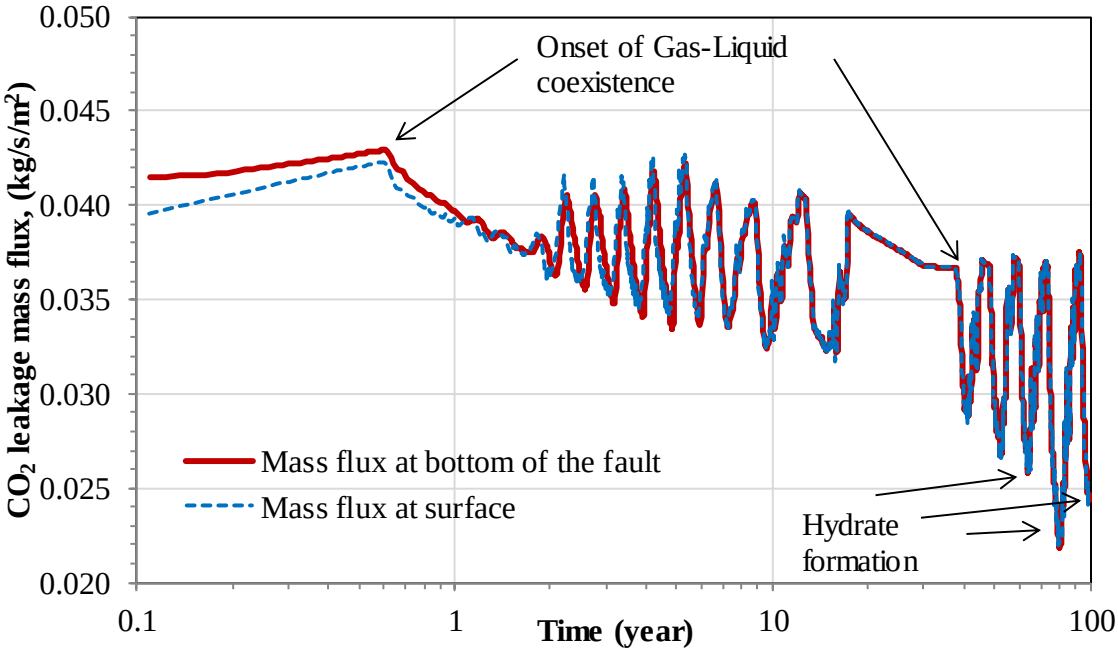

Figure 3.31: CO_2 leakage mass fluxes as a function of time.

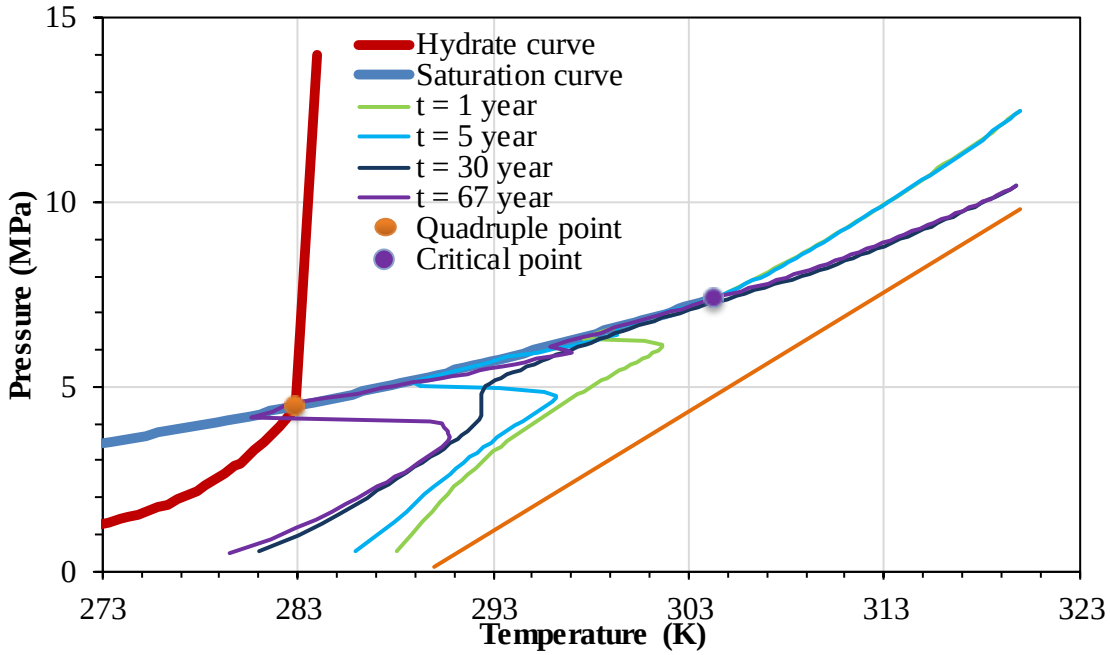

Figure 3.32: The Pressure-Temperature profiles at four different times. The blue curve is the CO_2 saturation curve and the red curve is the hydrate formation curve.

3.4 Influence of Fault Permeability and Fault Thickness on Leakage

3.4.1 Constant Fault Permeability

Permeability has a first order effect on leakage mass flux. A sensitivity study was performed to estimate its effect on leakage mass flux and the time taken to reach multiphase coexistence for two different overpressures. All other parameters were kept the same as the fault leakage scenario. Figures 3.33 and 3.36, respectively, show the maximum flux at any time in the fault and the flux at the first instance of hydrate formation for overpressure of 100 psi and 400 psi. Figures 3.35 and 3.38, respectively, show the time taken for the first instance of gas-liquid coexistence and the first instance of hydrate formation for overpressure of 100 psi and 400 psi. Figures 3.34 and 3.37,

respectively, show the comparison of leakage mass flux from natural analogues with the estimated flux for overpressure of 100 psi and 400 psi.

For an order of magnitude increase in permeability, the leakage mass flux increased by a factor of 10. The leakage mass flux increased in a linear fashion with the increase in fault permeability as shown in Figures 3.34 and 3.37. The variation in permeability was not found to affect the fluid properties. The cooling effect and the cyclic nature of leakage were severely diminished at low permeability faults as indicated by the time taken to reach multiphase conditions. The convective energy flux in the fault increased with increase in permeability. Hence the multiphase coexistence conditions were reached faster. The time taken to reach multiphase coexistence conditions decreased in a power law fashion with the increase in permeability. At low overpressures (100 psi) as shown in Figure 3.35, the time taken to reach gas-liquid coexistence is greater than 100 years for fault permeability lesser than 500 md. The hydrate formation takes greater than 300 years for the fault permeability lesser than 500 md. Therefore the effects of multiphase coexistence conditions are less significant and can be neglected for low permeability faults. Hence, the fault permeability has the largest effect on leakage mass flux and the cooling behavior.

For comparison, the leakage mass fluxes from natural analogues discussed in Chapter 1 are shown in Figures 3.34 and 3.37. The computed fluxes are well above the values mentioned here but the leakage area of the natural analogues was larger than this fault leakage scenario. The intention here is to set the calculated fluxes in context with naturally occurring fluxes and not to comment on whether the values are large or small enough to neglect compared to naturally occurring fluxes. This context provides the confidence that the leaks can be identified during monitoring even for low permeability faults.

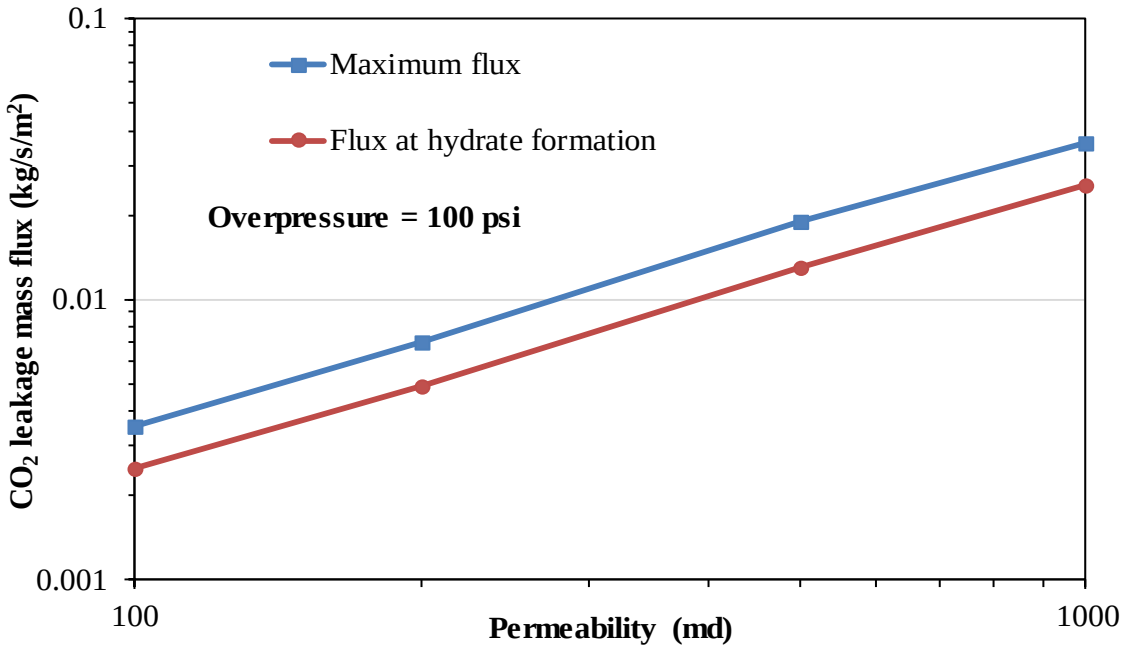

Figure 3.33: The maximum flux and flux at hydrate formation as a function of permeability at overpressure = 100 psi.

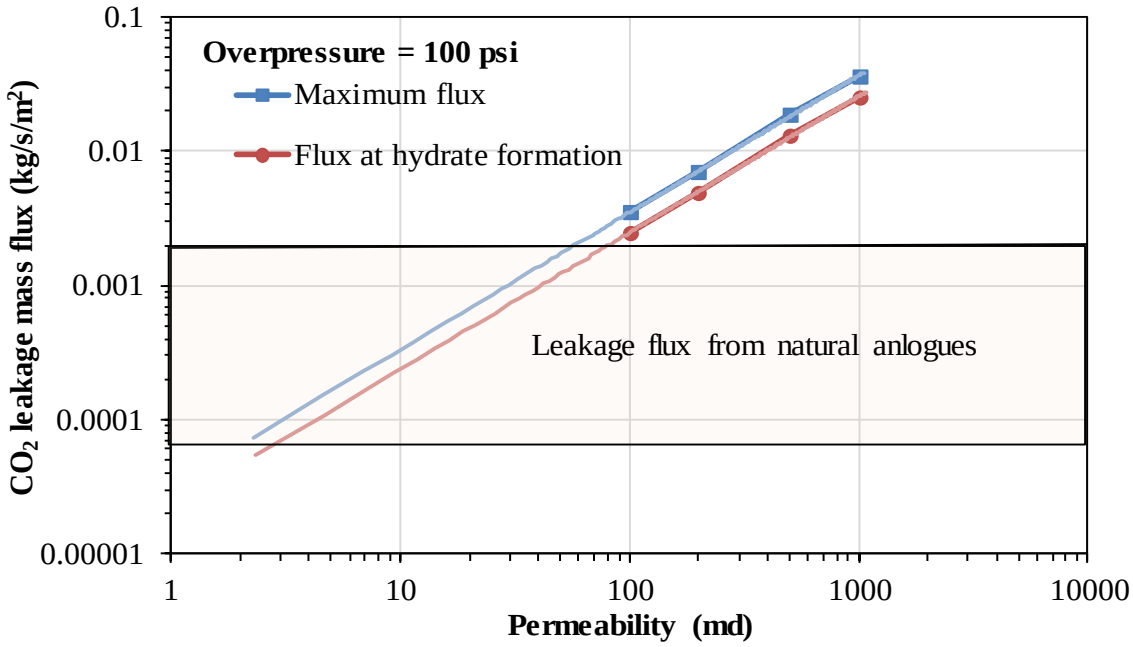

Figure 3.34: The estimated fluxes as a function of permeability at overpressure = 100 psi compared with flux from natural analogues.

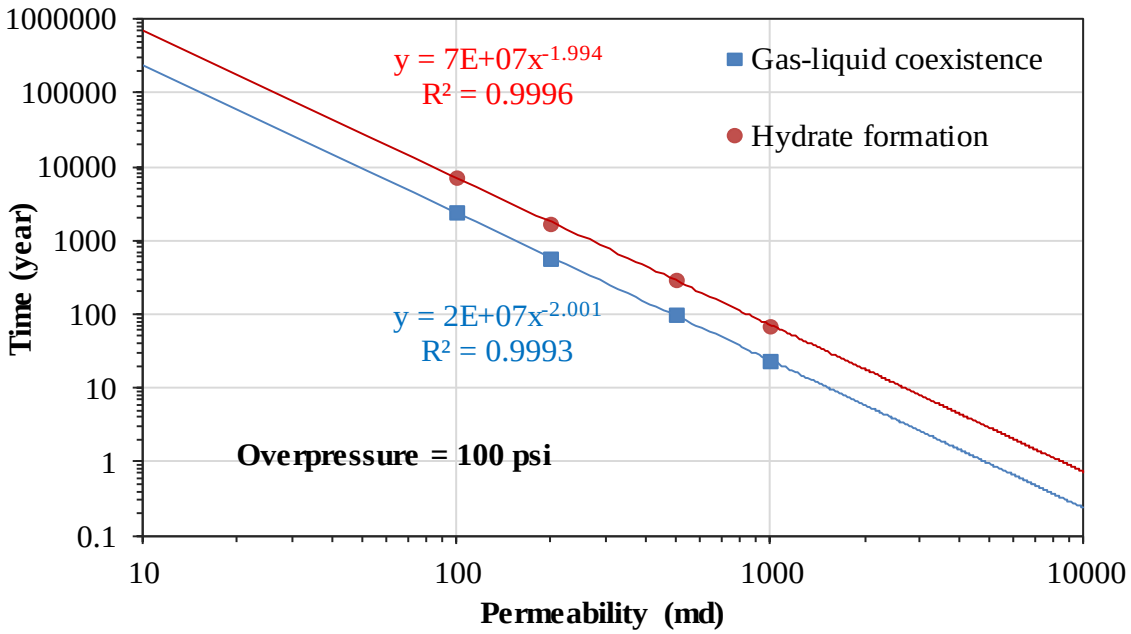

Figure 3.35: Time taken for the first instance of gas-liquid coexistence and hydrate formation as a function of permeability for overpressure = 100 psi.

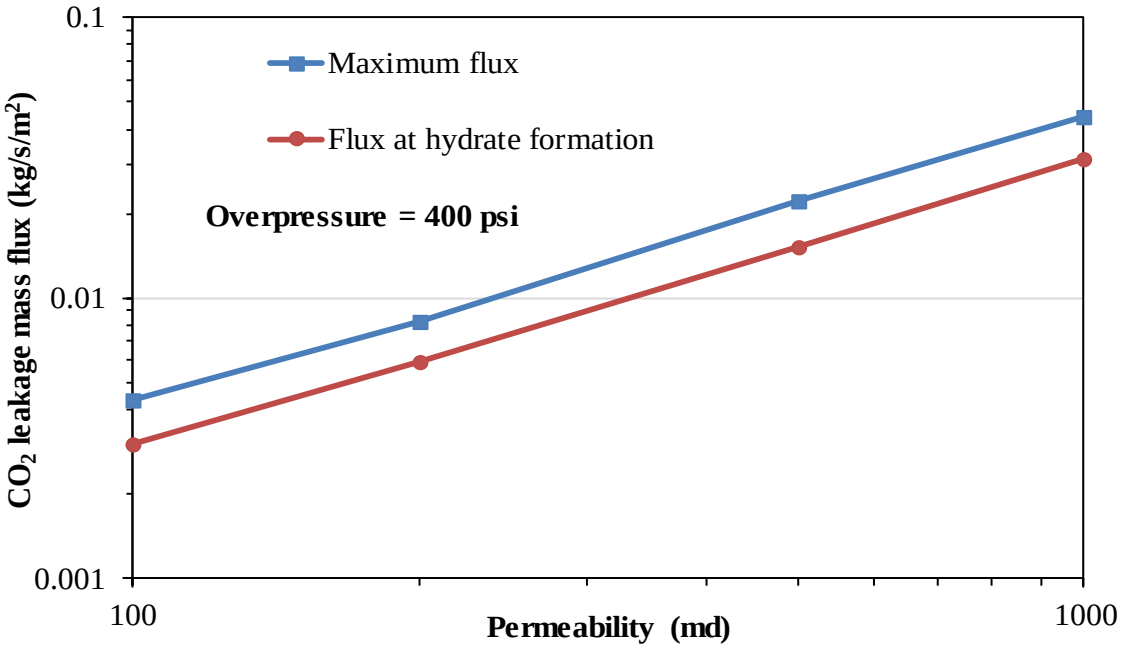

Figure 3.36: The maximum flux and flux at hydrate formation as a function of permeability at overpressure = 400 psi.

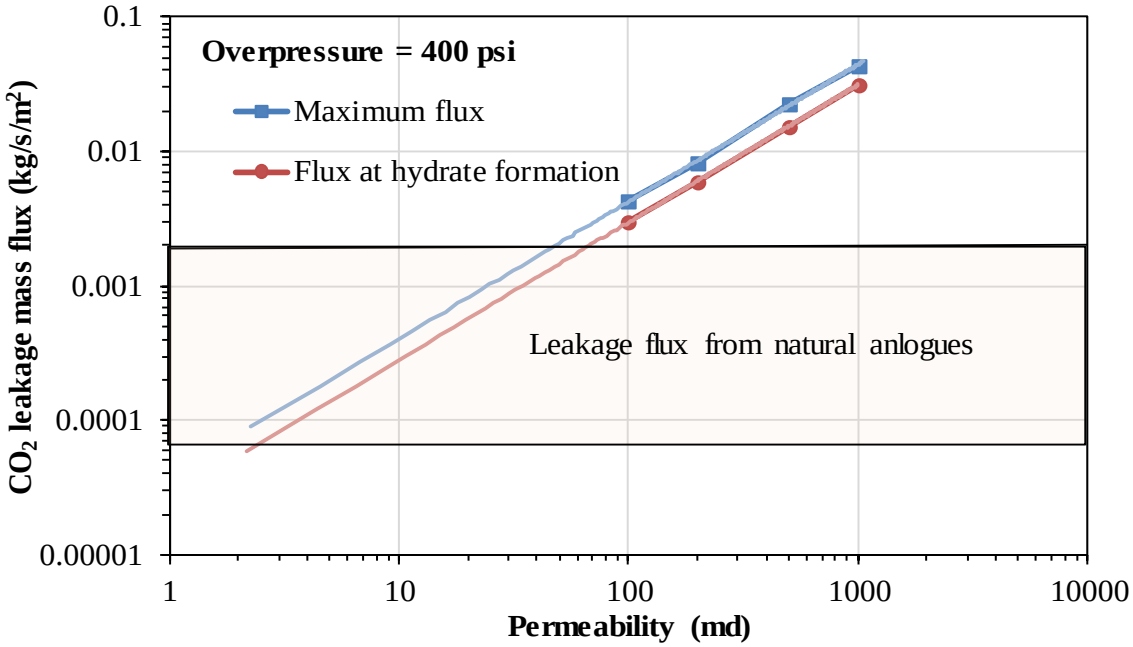

Figure 3.37: The estimated fluxes as a function of permeability at overpressure = 200 psi compared with flux from natural analogues.

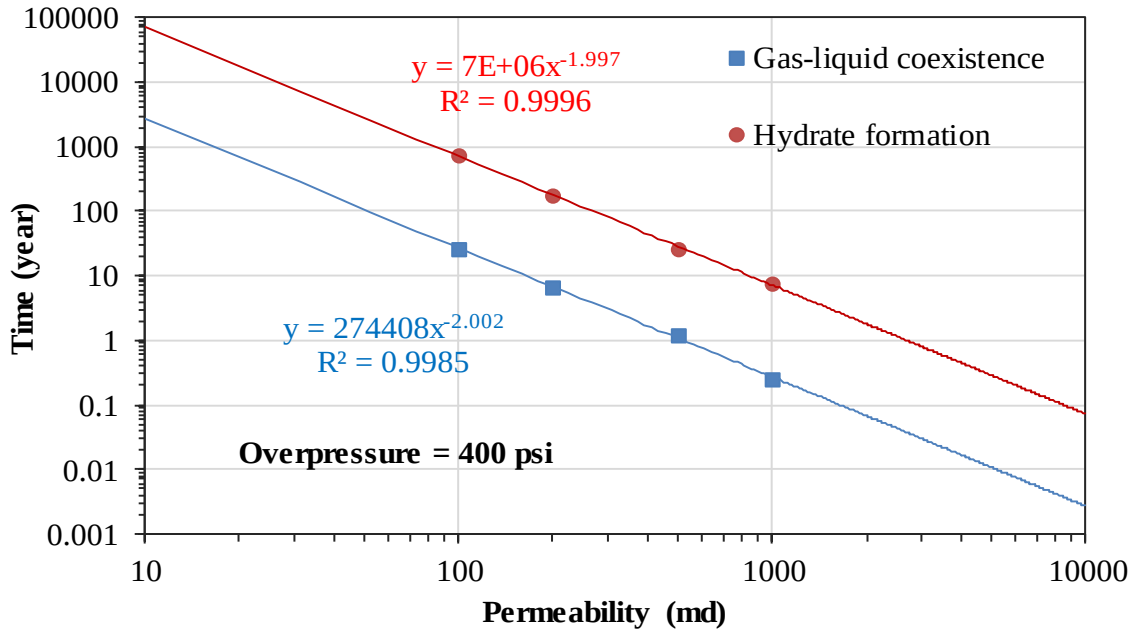

Figure 3.38: Time taken for the first instance of gas-liquid coexistence and hydrate formation as a function of permeability for overpressure = 100 psi.

3.4.2 Variable Fault Permeability

The permeability of the fault was kept constant for all the above scenarios. Although this analysis yielded several important observations regarding its effect on leakage mass flux, the permeability will vary based on the geological characteristics of the fault in real-world scenarios. Leakage mass flux results for a heterogeneous fault are presented in this section. Figure 3.39 shows the permeability at different sections of the fault used for this analysis. The rest of the parameters were kept the same as the fault leakage scenario.

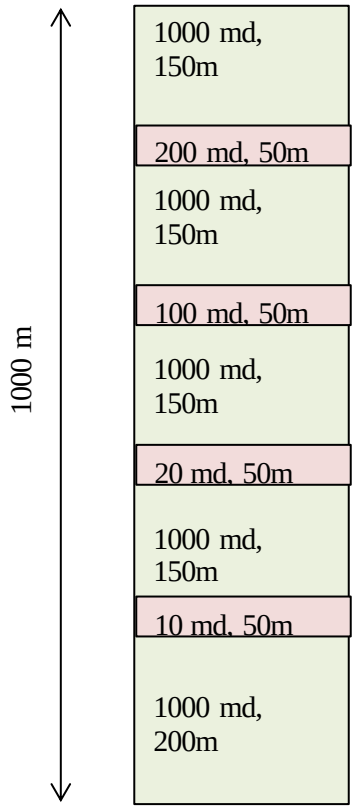

Figure 3.39: Geological representation of variable permeability fault.

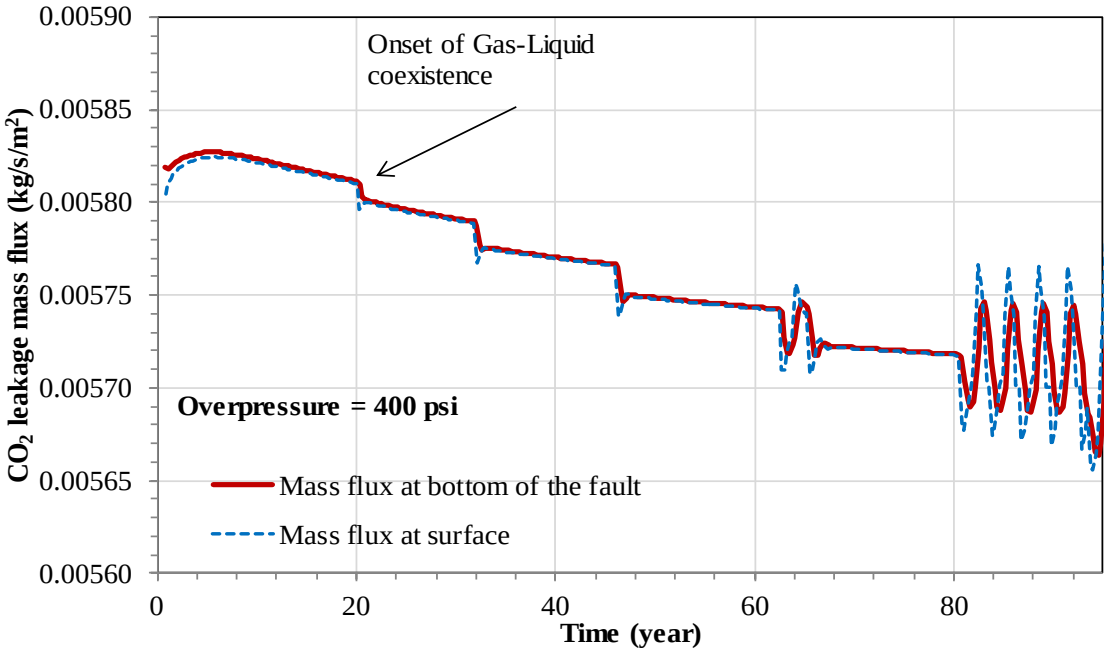

Figure 3.40: CO_2 leakage mass fluxes as a function of time for variable permeability case.

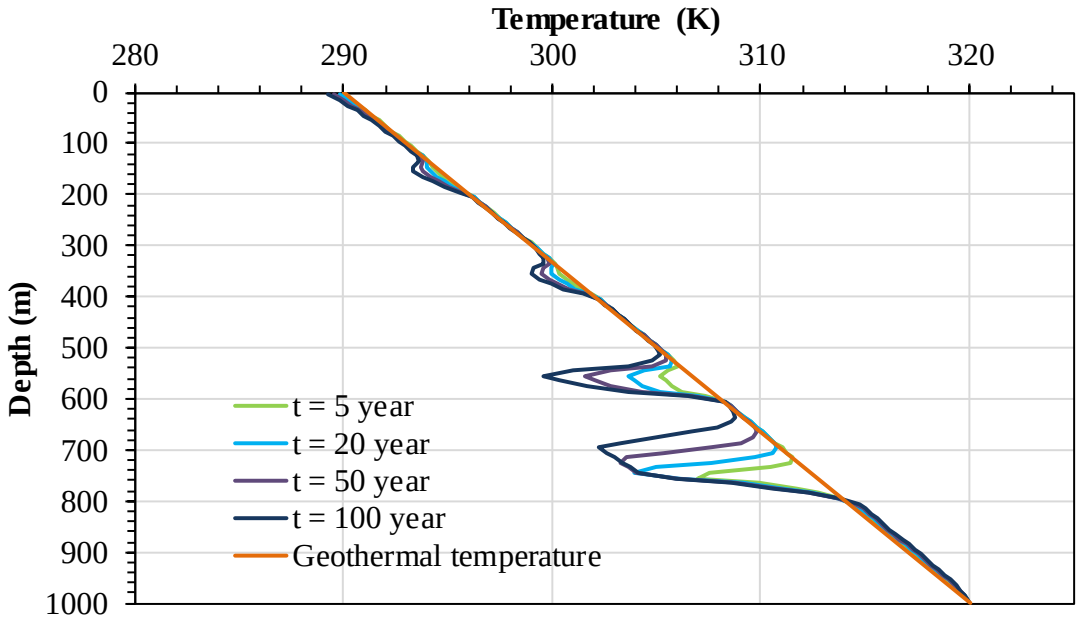

Figure 3.41: Temperature in the fault as a function of depth for 4 different times.

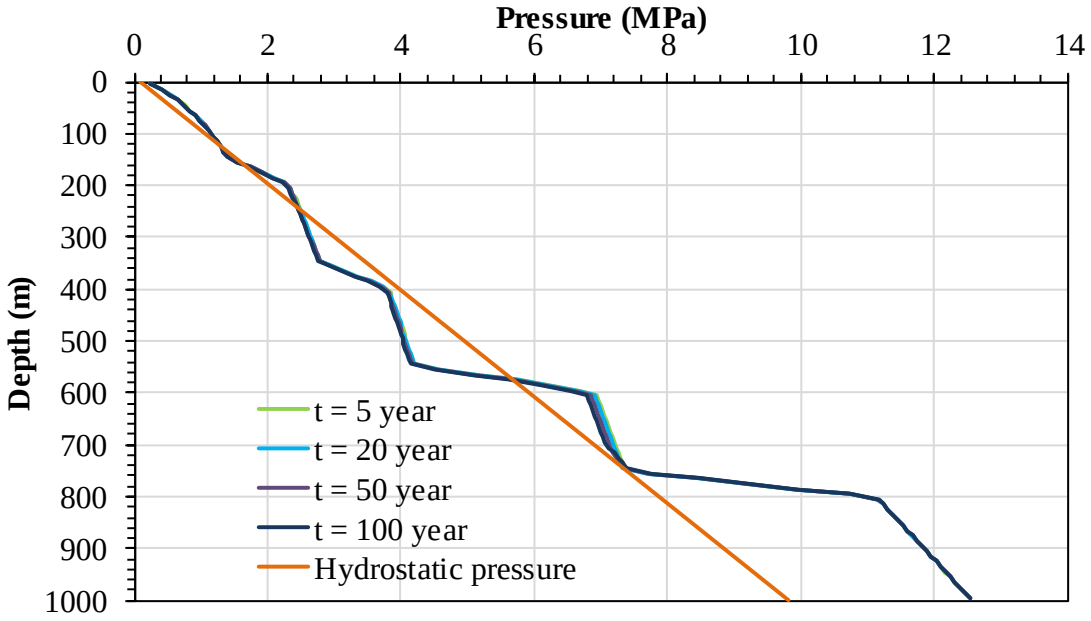

Figure 3.42: Pressure in the fault as a function of depth for 4 different times.

Figure 3.40 shows the leakage mass flux as a function of time for this heterogeneous case. Figures 3.41 and 3.42, respectively, show the temperature and pressure in the fault for 4 specific times. The pressure in the fault does not change much with time. The temperature dropped significantly in the low permeability layers. Joule-Thomson like cooling was observed as the CO_2 passed through the low permeability layers as evidenced by the pressure drop and the temperature decline in those layers.

The major conclusion is that low permeability layers have a significant impact on leakage mass flux as shown in Figure 3.40. The estimated leakage mass flux decreased by a factor of 8 compared to the flux calculated for a homogenous fault with a permeability of 1000 md. The computed mass fluxes are well above the fluxes from natural analogues but the leakage area of the natural analogues was larger than this fault leakage scenario. Thus, accounting for permeability variations is extremely important from a leakage mass flux estimation standpoint.

3.4.3 Fault Effective Width

Fault effective width has a strong effect on the cooling effect. A sensitivity study was performed to estimate its effect on leakage mass flux and the time taken to reach multiphase coexistence for a specific overpressure of 400 psi. All other parameters were kept the same as the fault leakage scenario. The leakage mass flux at the bottom and top of the fault for all the fault effective width values are shown in Figures 3.43 through 3.46. Figure 3.47 shows the time taken for the first instance of gas-liquid coexistence and the first instance of hydrate formation.

The maximum mass flux and the mass flux at first instance of hydrate formation were almost constant for all the effective width investigated in this study although the leakage rates changed due to the change in cross sectional area. The cyclic nature of leakage mass flux, time period and the amplitude of the cycles decreased as the fault effective width increased. The cyclic nature is primarily due to the oscillating balance between the convective energy flux in the fault and the conductive heat flux to the surrounding. Increase in fault effective width increased the convective energy flux in the fault and decreased the amplitude of the cycles. Although the cyclic nature was not exhibited, the cooling effect became stronger as the fault effective width increased as evidenced by the decrease in the time taken to multiphase coexistence conditions and hydrate formation conditions. The time taken for the first instance of multiphase coexistence and hydrate formation has a power law relationship which decreased in time with an increase in the fault effective width as shown in Figure 3.49.

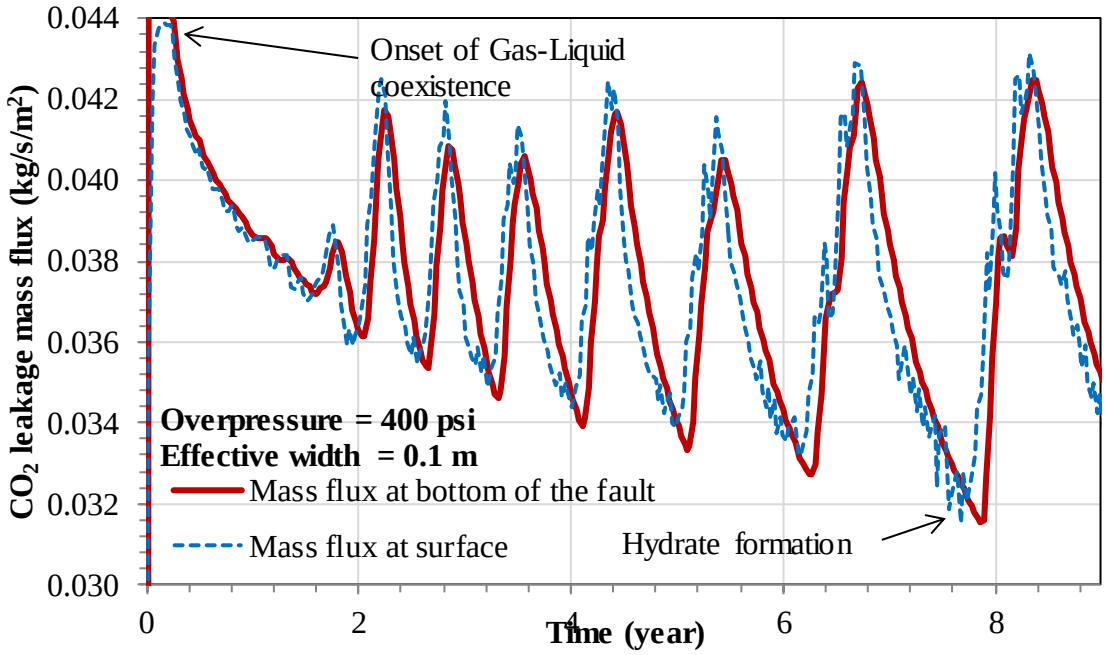

Figure 3.43: CO_2 leakage mass fluxes as a function of time for effective width = 0.1m.

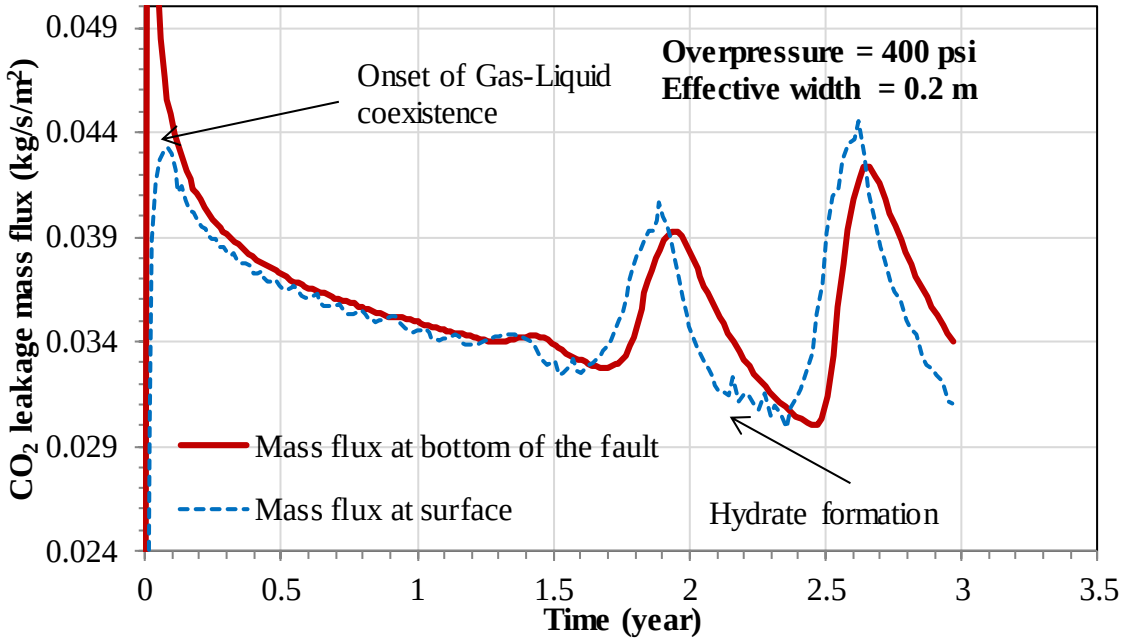

Figure 3.44: CO_2 leakage mass fluxes as a function of time for effective width = 0.2m.

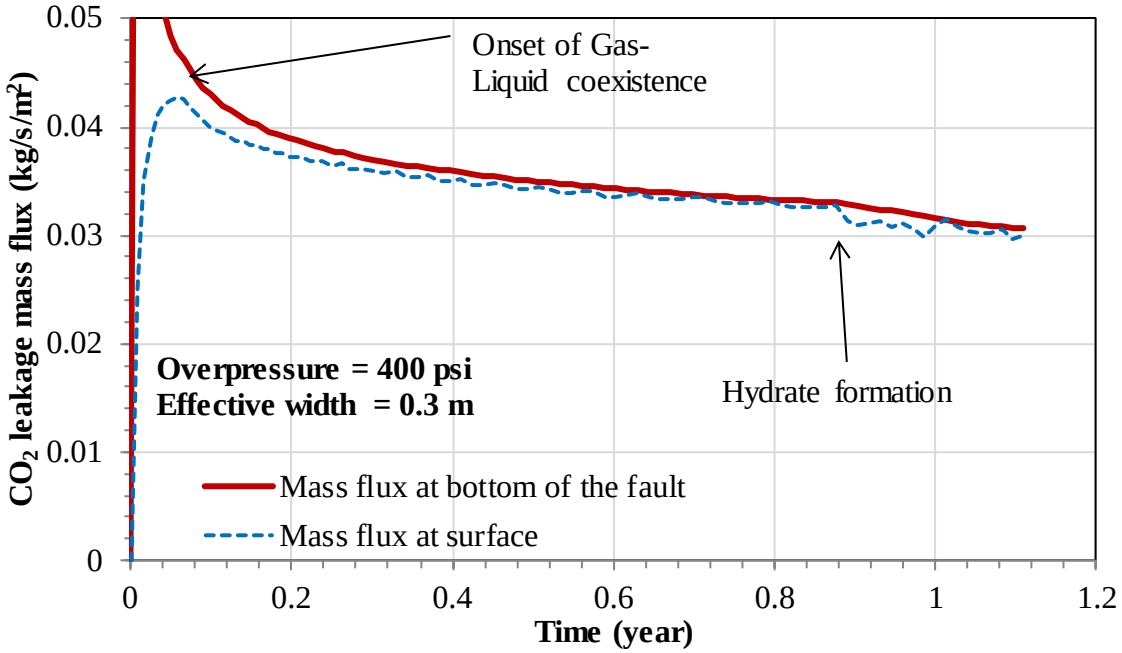

Figure 3.45: CO_2 leakage mass fluxes as a function of time for effective width = 0.3m.

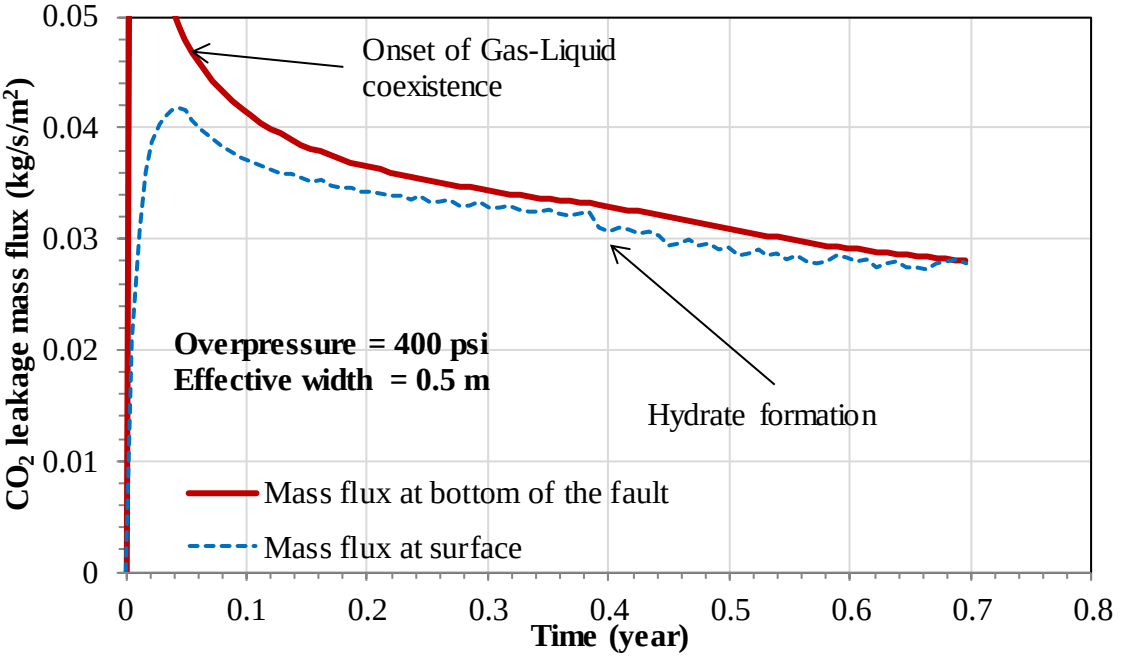

Figure 3.46: CO_2 leakage mass fluxes as a function of time for effective width = 0.5m.

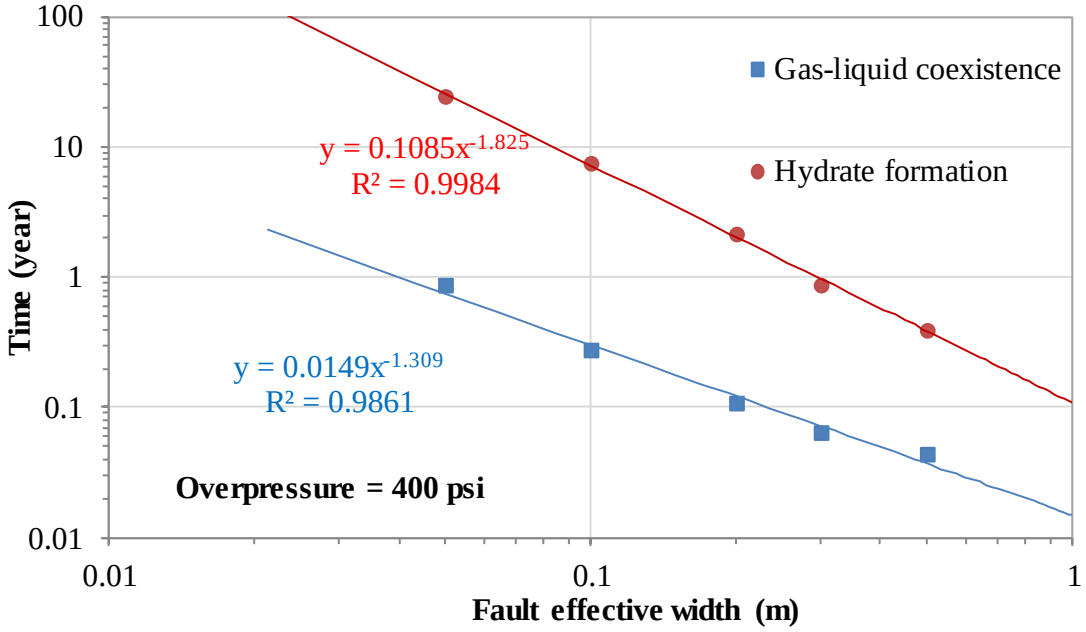

Figure 3.47: Time taken for the first instance of gas-liquid coexistence and first instance of hydrate formation as a function of fault effective width for overpressure = 400 psi.

3.5 Summary

A non-isothermal, quasi-1D numerical model was developed to estimate the leakage mass flux as a function of time. Mass flux was allowed only in the vertical direction. The conductive heat flux was accounted for in the direction perpendicular to flow. The model description, equations and solutions methods are discussed in Chapter 2. A highly idealized representation of a fault was used to capture the coupled effect of the thermal and multiphase flow aspects of leakage. Simulation results reveal how the fault properties combine with reservoir overpressure to affect CO_2 leakage.

For the particular conditions used to calculate the CO_2 leakage mass flux illustrated in Chapter 3, liquid-CO_2 condensation and CO_2-hydrate formation occurred

because of the decreasing temperature and pressure as CO_2 migrated up in the fault. Decompression near the critical pressure of CO_2 resulted in a strong cooling effect which reduced CO_2 temperature enough to reach gas-liquid coexistence conditions. The mobility of the CO_2 initially decreased when CO_2 condensation occurred based on the assumed relative permeability curves. Heat gain from the surrounding rock eventually evaporated the liquid CO_2 resulting in an increase in mobility and leakage mass flux. The CO_2 phase changes (gas to gas-liquid to gas) caused the leakage mass flux to cycle, which led to cyclic variations in temperature, gas saturation and pressure. The time period and the amplitude increased with each successive cycle. Eventually hydrates formed in part of the fault. The hydrates further reduced the CO_2 mobility and leakage mass flux in a cyclic manner. The pressure increased at every depth when compared to the hydrostatic pressure and there was a significant temperature decrease in the multiphase regions. The maximum temperature decrease at each time occurred at the top of the two phase region with close to a 15 K decrease at the hydrate formation depth.

The pressure in the storage reservoir increases upon CO_2 injection. This pressure increase is termed as overpressure. Leakage mass fluxes increased about 29% with an overpressure of 400 psi. The mass flux decreased 30% for all cases at the first instance of hydrate formation. The time taken for the first instance of gas-liquid coexistence and hydrate formation decreased exponentially with an increase in overpressure. At higher overpressures (> 400 psi), the multiphase coexistence conditions were reached in less than 1 year. Thus, the effect of overpressure on leakage should be considered when managing a storage reservoir.

The fault permeability has a first order effect on leakage. The leakage mass flux increased in a linear fashion and the time taken to reach multiphase conditions decreased in a power law fashion with an increase in permeability. The leakage mass flux increased

by a factor of 10 when the fault permeability was increased a factor of 10. The cooling effect and the cyclic nature of leakage are much less important for faults with low permeability. Condensation takes more than 100 years and hydrate formation takes more than 300 years for faults with a permeability less than 500 md. The time taken to reach multiphase flow conditions decreased in a power law fashion with the increase in fault effective width, but did not increase the leakage mass flux. Increase in fault effective width increased the convective energy flux in the fault and dominated the conductive heat flux to the surroundings and hence cooled faster.

Chapter 4: Steady-State Flow Model and Results

A simplified steady-state flow model is presented in this chapter. The modelling approach, transport equations and solution methods are discussed. The steady state model was used to analyze various leakage scenarios. The effects of reservoir pressure and temperature, depth, permeability, multiphase coexistence, and hydrate formation are quantified with a sensitivity analysis.

4.1 INTRODUCTION

Several researchers have developed analytical and semi-analytical models to estimate leakage mass fluxes (Celia et al, 2004, Nordbotten et al., 2005, Chang et al, 2008 and Tao, 2012) through faults and wellbores. The fluxes were estimated with an isothermal assumption mostly (non-isothermal assumptions was used in certain section of the fault by Tao, 2012) and issues related to the permeability of the leakage pathways and the pressure at the leakage source were well addressed. The non-isothermal nature of leakage throughout the fault and multiphase coexistence considerations (condensation, evaporation and hydrate formation) were not taken into account in the above mentioned models and provide a motivation for the current work. Thus a steady-state flow model was developed to estimate the leakage mass fluxes to account for the non-isothermal nature and multiphase coexistence. The model presented here can be used within the risk assessment framework for geological storage.

To account for the non-isothermal nature and multiphase flow effects on the leakage mass flux, two different limiting conditions were assumed for the steady state model:

1) The temperature of the CO_2 was assumed to be the same as the surroundings based on an assumed geothermal gradient. This is called the geothermal temperature case below.
2) The temperature of the CO_2 was calculated from the constant flowing total enthalpy specified at the leakage source (except after hydrate forms as discussed below). The sum of the enthalpy and potential energy is constant when there are no heat losses (adiabatic system). This is called the constant flowing total enthalpy case below.

These two conditions are upper and lower bounds for the leakage mass flux. The leakage mass flux will vary between these bounds due to multiphase flow considerations as discussed in the previous chapter.

Thorough risk assessment plays an important role in the site selection, operation, closure, and monitoring of storage projects (Pawar et al., 2015). The sensitivity of the estimated leakage mass flux to geological parameters can provide insights into the preferred rock types for storage and necessary rock properties that need to be measured prior to site selection. The model can also provide insights into the operating conditions at which leakage can be minimised and key pressure-temperature signals that aid quick identification during monitoring and verification stage post-injection (Jenkins et al., 2015). The model can also be used to analyse existing leakage. This will provide insights into remediation strategies required to plug the leak.

4.2 MODELING APPROACH

A leakage pathway is assumed to intersect the storage reservoir. The injected CO_2 is assumed to have reached the base of the leakage pathway and 100% CO_2 is assumed to

leak. Faults are chosen as the leakage pathway for this study because of their high permeability and higher leakage mass flux compared with other pathways (Tao, 2012). Analysis for other types of leakage pathways can be performed by altering the pathway properties in this model. The fault is assumed to be a 1-D vertical porous medium with specific geometry (effective width, breadth), rock properties (porosity, permeability) and rock-fluid properties (relative permeability, initial saturations). This enabled the application of Darcy's law to model flow through the fault. The complexities related to the geology of fault core and damaged zone surrounding it is simplified. Averaged values were used along the horizontal directions, but they can vary spatially with the depth. More complex fault characteristics related to in situ stress, stress-dependent properties and fault branching amongst other geo-mechanical considerations are not included in this model. The aqueous phase is assumed to at residual saturation. This assumption is intended to calculate the worst-case fluxes when leakages occur.

4.2.1 Geothermal Temperature Case

For this condition, the CO_2 is assumed to move slowly enough to equilibrate with the geothermal temperature of the surrounding formations. The effect of non-linear fluid properties on leakage can be quantified. There will be single phase regions in the fault. Mass balance is performed to calculate the steady state leakage mass flux.

4.2.2 Constant Flowing Total Enthalpy Case

For this condition, the CO_2 is assumed to move quickly enough to undergo decompressing flow without heat exchange. There will be substantial cooling in the fault with multiphase coexistence. For a distinct time, the key regions for such a flow are

shown in Figure 4.1. The goal is to calculate the maximum possible effect of the multiphase coexistence on leakage. The total enthalpy is constant when the system is adiabatic i.e. there is no heat exchange with the surroundings.

The corresponding temperature drop in the fault is termed as adiabatic temperature drop. Although this assumption is extreme, it is quite commonly used to model decompressive flows observed near magmatic intrusion, mantle convection and hydrothermal systems (Barton and Toulmin, 1961, Norton and knight, 1977, Mastin and Ghiorso, 2001, Ingberitsen and Hyaba, 1994 and Ganguly, 2005). The practical significance of such an assumption is that the adiabatic flow will act as a limiting case and the adiabatic temperature drop will act as the maximum possible temperature drop besides calculation simplicity. Surrounding heat will contribute to flow heating up in real world scenarios and the flow will deviate from the constant flowing total enthalpy assumption as discussed in the previous chapter.

The potential energy contribution (gD) should be taken into account since the flow is vertical (Dodson, 1971, Ramberg 1971). Change in potential energy contribution over vertical displacement balance the change in fluid enthalpy for steady-state vertical adiabatic flow. This will result in a constant (h_f-gD). Here, h_f refer to the flowing fluid enthalpy, (h_f-gD) refer to flowing total enthalpy and D is the depth in positive downwards direction. The fluid will gain potential energy at the expense of enthalpy for flow in the vertical direction (Hagoort, 2005 and Patterson et al., 2008). For example, there will be a gain in potential energy of 9.81 kJ/kg with an equivalent loss in fluid enthalpy for flow in a 1000m vertical fault.

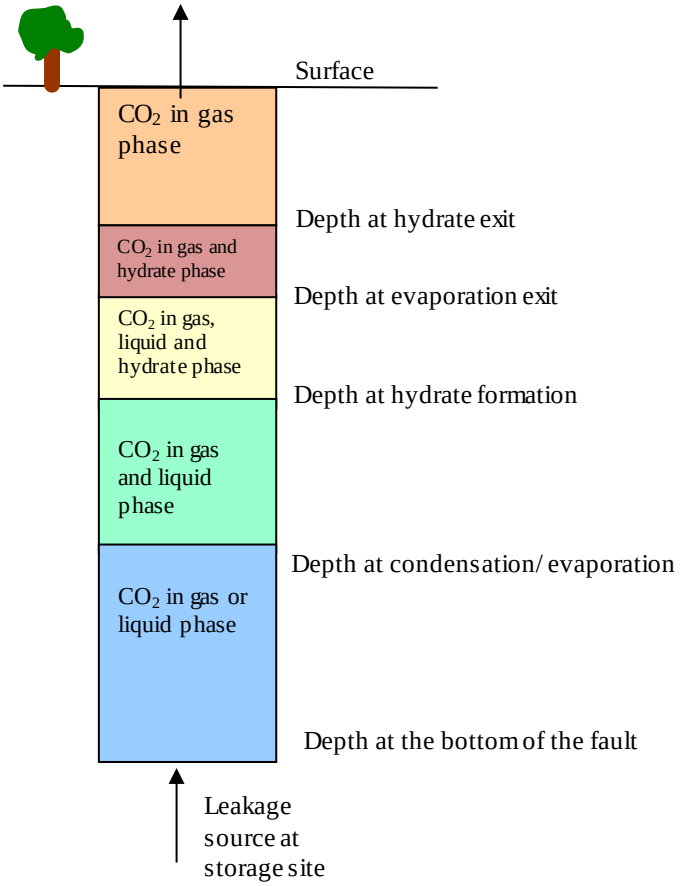

Figure 4.1: Schematic representations of key regions during CO_2 leakage. The key regions are characterized by the phases present in them. CO_2 is in supercritical conditions close to the leakage source as shown by the blue region. Leaked CO_2 was in saturated state in the green region. CO_2 will condense or evaporate to form two phases in this region. The condensation/evaporation depended on the P-T conditions at the entrance. CO_2-hydrates formed with adequate amount of water and amenable P-T conditions as shown by the yellow region. Below a certain pressure, the liquid CO_2 evaporated which resulted in a two-phase region with gas and hydrates as shown by the red region. The hydrates melted to form a single gas phase as shown by the orange region close to the exit.

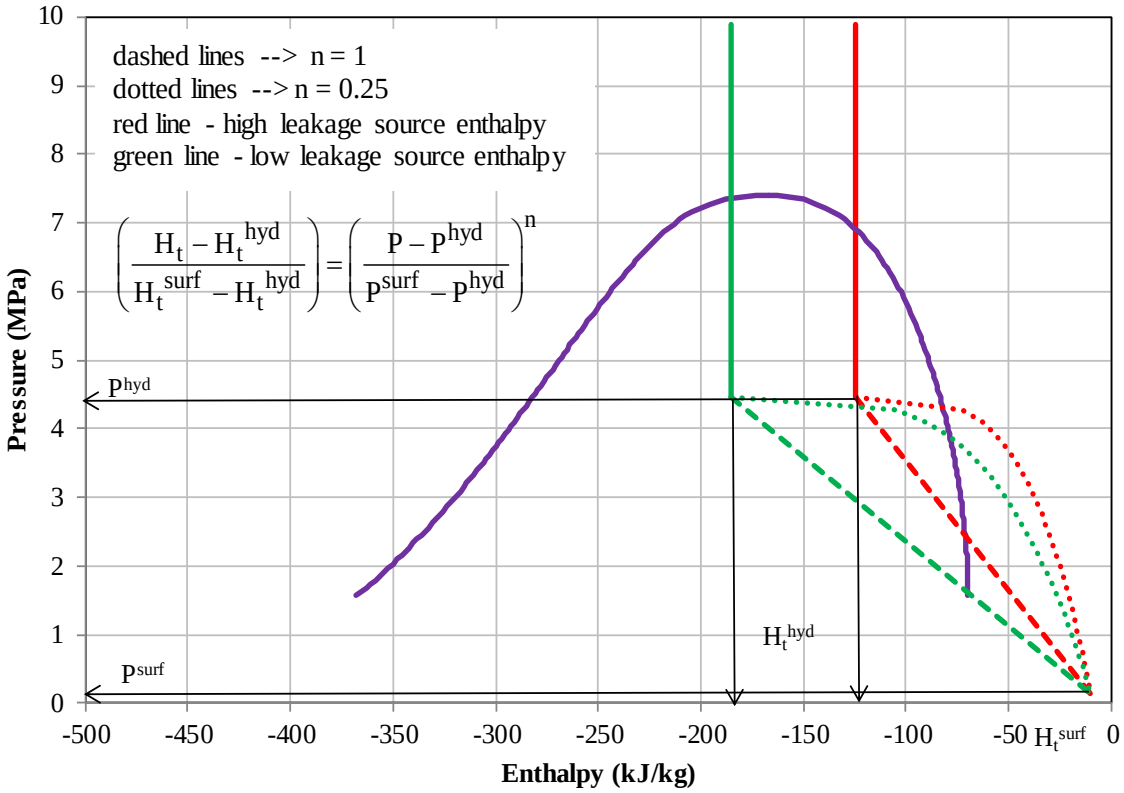

Figure 4.2: A representation of pressure-enthalpy scenario for two different leakage source enthalpies. The purple curve represents the saturation curve for CO_2. The red and green curves were the flowing total enthalpy as a function of pressure for the fault leakage scenarios. The solid line represented the flowing total enthalpy until hydrate formation. The dotted and dashed lines represented the flowing total enthalpy as a function of pressure post hydrate formation. The dashed line is for n = 1 and dotted line is for n = 0.25 where n is the power-law exponent as shown in the equation presented in the figure. n = 0.25 is used for this study.

The constant flowing total enthalpy case was used until hydrate formation occurred. The adiabatic temperature goes below 273K after hydrate formation. Although physically possible, this scenario is highly unlikely based on the unsteady state model presented in Chapter 3. Hence, the flowing total enthalpy is assumed to increase based on a pre-determined path as a function of pressure after hydrate formation. The enthalpy increase is determined by a power law relationship between pressure and the flowing

total enthalpy at hydrate formation pressure and surface pressure. A typical enthalpy profile is shown in Figure 4.2 along with the power law relationship. Although this assumption is crude, the approximated enthalpy is close enough to the numerical results shown in Chapter 3 and hence provides confidence with this approach.

The flowing total enthalpy is defined as function of pressure for all sections in the fault with the help of the constant flowing total enthalpy assumption and the post-hydrate power-law relationship assumption. The temperature, mole fractions and phase states can be calculated from this relationship. Span-Wagner technical EOS for CO_2 (Span and Wagner, 2003) is used for phase behavior and fluid properties estimation. The mass flux, pressures and depths described in Figure 4.1 are the unknowns. Mass balance is performed to calculate the unknowns.

4.3 STEADY-STATE FLOW MODEL DESCRIPTION

The steady-state flow model is presented in this section. Summary of the assumptions used to derive the mass balance are:

1) Steady state 1-D flow of CO_2 in a vertical fault.
2) Constant pressure and temperature at the bottom and top of the fault.
3) Multiphase Darcy's law is applied to flow in fault.
4) Capillary pressure is neglected.
5) Residual water saturation in fault after steady state flow of CO_2 reached.
6) Hydrates will only affect the permeability in the formed region.
7) The flowing total enthalpy is defined as function of pressure for all sections in the fault with the help of the constant flowing total enthalpy assumption and

the post-hydrate power law relationship assumption for the constant flowing total enthalpy case.

8) The temperature in the fault is assumed to have equilibrated with the geothermal temperature for the geothermal temperature case.

The overall mass balance constraint is shown in equation (4.1). Where m is the total mass rate and m_g and m_l are mass rates of gas and liquid respectively, and A is the area perpendicular to flow. The mass flux for each phase is written as shown in equation (4.2). Where k is the absolute permeability of the fault, subscripts l and g refers to the liquid and gas phase respectively, k_{rj} is the relative permeability of phase j, μ_j is the viscosity of phase j and ρ_j is the mass density of phase j.

$$\left(\frac{m_g}{A}\right)+\left(\frac{m_l}{A}\right)=\left(\frac{m}{A}\right)=\text{constant} \tag{4.1}$$

$$\left(\frac{m_g}{A}\right)=-\frac{\rho_g k k_{rg}}{\mu_g}\left(\frac{dP}{dD}-\rho_g g\right),\quad \left(\frac{m_l}{A}\right)=-\frac{\rho_l k k_{rl}}{\mu_l}\left(\frac{dP}{dD}-\rho_l g\right) \tag{4.2}$$

The multiphase flow effects are ignored for calculations in the geothermal case. CO_2 is assumed to establish a steady saturation. Temperature is given as a function of depth with the help of the geothermal gradient and the surface temperature. The mass flux and pressures are the unknowns that are solved for using the model. The mass balance equation (4.1) together with mass flux equation (4.2) is solved to obtain the leakage mass flux. The fault is discretized into blocks and the equations are solved iteratively until the mass balance constraint is honored.

The multiphase flow effects are taken into account for calculations in the flowing total enthalpy case. The flowing total enthalpy is defined as a function of pressure throughout the fault. The flowing enthalpy is identical to the enthalpy of the fluid in the

single phase regions. But the flowing enthalpy is dependent on the mobilities of the phases and the nature of relative permeability functions in the multi-phase regions. The flowing mass fraction of gas phase, X_{gflow}, in the two-phase region is shown in equation (4.3)

$$X_{gflow} = \frac{m_g}{m_g + m_l} \tag{4.3}$$

The flowing total enthalpy in the two phase region is written as shown in equation (4.4). Where h_f, h_g, h_l are the flowing enthalpy of fluid mixture, gas enthalpy and liquid enthalpy, respectively.

$$\begin{aligned} &X_{gflow}\left(h_g - gD\right) + \left(1 - X_{gflow}\right)\left(h_l - gD\right) = \left(h_f - gD\right) \\ &X_{gflow} = \frac{h_f - h_l}{h_g - h_l} \end{aligned} \tag{4.4}$$

The relative permeability and the saturations are solved for a known X_{gflow} in the two-phase region. Relative permeability is defined as a function of saturation. Saturation is related to fluid mass fraction (x) and molar volume (V) as shown in equation (4.5).

$$\begin{aligned} &S_g + S_l + S_w = 1 \rightarrow \text{Saturation constraint} \\ &x_g + x_l = 1 \rightarrow \text{Molefraction constraint} \\ &S_g = \left(1 - S_w\right)\frac{x_g V_g}{x_g V_g + x_l V_l}, \\ &S_l = \left(1 - S_w\right)\frac{x_l V_l}{x_g V_g + x_l V_l} \\ &k_{rj} = k_{rj}^{o}\left(\frac{S_j - S_{jr}}{1 - \sum_j S_{jr}}\right)^{n_j} \end{aligned} \tag{4.5}$$

Using X_{gflow}, the mass fractions are the unknowns that are solved for. Hydrate formation is assumed to affect the permeability alone. Several experiments have been reported showing the effect of CO_2-hydrates on rock permeability (Kumar et al., 2010, Masuda et al., 1997). These experimental data were used to calibrate the correlation between the permeability and hydrate saturation given by equation (4.6).

$$k_{red} = (1 - S_h)^{n_h}$$
$$k_{hyd} = k_{red} k \tag{4.6}$$

The permeability reduction factor, k_{red} in the hydrate region is only a function of the hydrate saturation, s_h, and a hydrate exponent, n_h. The hydrate exponent typically varies from 3 to 5 based on the hydrate saturation. An exponent of 3 was used for this study based on the experimental results (Kumar et al., 2010, Masuda et al., 1997). The hydrate saturation is calculated using the Van der Waals-Platteeuw method available in PVTSIM software (Pedersen, 2014). It is assumed that all the water available is converted to hydrates when the pressure-temperature condition for hydrate formation is attained. This is a reasonable assumption for low water saturations.

The mass balance constraint (4.1) together with Darcy flux equation (4.2) and flowing mass fraction equation (4.3) are solved to obtain the leakage mass flux. The fault is discretized into blocks and the equations are solved iteratively until the mass balance constraint is honored. Calculations for both situations are performed in SI units. Span-Wagner technical EOS for CO_2 (Span and Wagner, 2003) is employed for phase behavior and fluid properties estimation.

4.3 STEADY-STATE FLOW MODEL BASE CASE RESULTS

Detailed results for a base case of leakage from the steady-state flow model to illustrate the non-isothermal nature and multiphase coexistence are presented in this section. Calculations were performed for both the cases described in the previous section. These results are also compared with leakage mass flux calculated from an isothermal model. In this base case application of the steady-state flow model, a homogenous vertical fault from the surface to a depth of 1000 m with a permeability of 1000 md is considered. The cross-sectional area allowable for flow is kept constant throughout the fault. The surface temperature is assumed to be at 290.15 K (17 °C) and the surface pressure is assumed to be 0.10135 MPa (14.7 psi). The temperature (320.15 K, 47 °C) and pressure (9.815 MPa, 1423.5 psi) at the bottom of the fault is calculated using the geothermal and hydrostatic gradients specified in Table 4.1. The bottom of the fault is assumed to be connected to a continuous source of CO_2 at constant pressure and temperature and explicitly not modelled here. The storage reservoir is over-pressurized due to the injection and storage ($\Delta P_s = P_{reservoir}-P_{hydrostatic}$). The overpressure is represented in psi units for ease of understanding. The fault is assumed to be at residual water saturation. No overpressure is assumed for this base case calculation. The geological description of the fault and relative permeability values used are shown in Table 4.1 and schematic representation of the fault is shown in Figure 4.3.

Table 4.1: Input parameters for base case in the steady state flow model

Parameters	**Values**
Geological Description	
Fault porosity, φ	0.3
Fault effective width (m)	0.1
Fault breadth (m)	10.0
Fault length (m)	1000
Permeability, k (md)	1000
Initial Conditions	
Surface temperature, T_{surf} (K)	290.15
Geothermal gradient, GG (K/m)	0.03
Hydrostatic gradient, HG (MPa/m)	0.0097
Temperature at the bottom of fault, T_b (K) ($T_b = T_{surf} + GG*D$)	320.15
Pressure at surface, P_{surf} (MPa) (psi)	0.10135 (14.7)
Pressure at the bottom of fault, P_b (MPa) (psi) ($P_b = P_{surf} + HG*D$)	9.815 (1423.5)
Residual water saturation, S_{wr}	0.2
Overpressure at the bottom of the fault, ΔP_s (MPa) (psi)	0 (0)
Relative permeability constants	
Gas relative permeability, k_{rg}	$k_{rg} = 0.64*(S_g/(1-S_{wr}))^2$
Liquid relative permeability, k_{rl}	$k_{rl} = 0.64*(S_l/(1-S_{wr}))^2$
Enthalpy exponent post hydrate, n	0.25
Hydrate exponent for permeability reduction, n_h	3

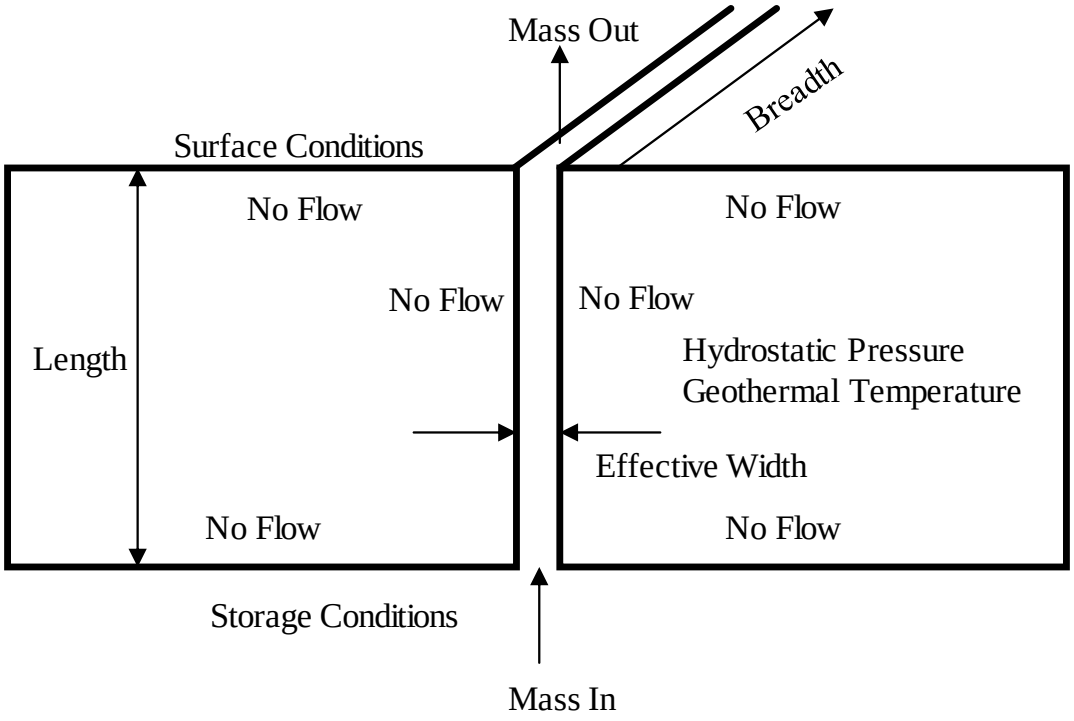

Figure 4.3: Schematic representation of the fault system used for base case calculation

The steady-state leakage mass fluxes for both the cases are estimated with the model and the results are shown in Table 4.2. For the sake of comparison, leakage mass flux from an isothermal model is also shown. Calculations for the isothermal model are performed with constant density and viscosity of CO_2, evaluated at leakage source conditions. The results indicated that the isothermal model overestimated leakage mass flux. As shown in Figure 4.5e and 4.5f, density and viscosity variation with depth is non-linear. Accounting for this non-isothermal nature (geothermal temperature case) decreased the estimated flux by 33% when compared to the isothermal model. As shown in Table 4.2, multiphase coexistence and hydrate formation (flowing total enthalpy case) decreased the leakage mass flux by 33% when compared to the geothermal case and 50% when compared to the isothermal model.

Table 4.2: Leakage mass flux estimated from three approaches for base case

Estimation Approach	**Leakage mass flux, kg/s/m^2**
Isothermal model	0.0485
Geothermal temperature case	0.0328
Flowing total enthalpy case	0.0235

The pressure-temperature profiles in the fault for both cases are shown in Figure 4.4. The depth profiles for pressure, temperature, density, viscosity, mass flux and Darcy velocity for both estimation approaches are shown in Figure 4.5. The pressure in the fault is higher than the corresponding hydrostatic pressure at that depth under both temperature conditions. Although this might provide a driving force for CO_2 to leak-off from the fault into intersecting permeable layers if any, higher pressures will provide a signal during monitoring which will lead to quicker remediation. Similarly, under multiphase coexistence conditions, temperature decreased by upto 14 K compared to the geothermal temperature at that depth and will act as a monitoring signal for quick remediation. Much smaller density closer to the surface resulted in larger Darcy velocity, which provided another monitoring signal for leakage. Thus, besides the uncertainty associated with the rock properties (permeability, etc.), the non-isothermal nature and multiphase coexistence have substantial impact on the steady state leakage mass flux estimates and provide substantial information for leakage identification.

The constant flowing total enthalpy assumption is able to capture all the multiphase regions shown in Figure 4.1 that exist during leakage. The profiles of saturation, mole fractions and flow fractions are shown in Figure 4.6. CO_2 existed in gas phase from the base of the fault until around 602 m depth (Depth of condensation/evaporation). Gas CO_2 transitioned into a two phase region of liquid and gas at this depth. The phase saturation remained almost constant in the two phase region

but the flow fraction and mole fraction of the gas phase continuously decreased in this region until hydrate formation at 346 m of depth (depth of hydrate formation). The liquid phase evaporated at 334 m of depth (depth of evaporation exit) and the formed hydrates melted at 330 m of depth (depth of hydrate exit). CO_2 existed as gas phase from 330 m till the surface. The amount of liquid and gas present is a function of the flowing total enthalpy (-146 kJ/kg for this case) and the relative permeability functions. Formed hydrates adversely affected the permeability in the hydrate formed regions and the mass flux.

The steady state leakage mass flux through a fault of 1000 md permeability for both situations are calculated to be 0.0328 kg/s/m^2 or 1,034,380 kg/yr/m^2 (geothermal case) and 0.0235 kg/s/m^2 or 741,096 kg/yr/m^2 (flowing total enthalpy case). Leakage mass flux is expressed independent of the area. Taking the area (0.1*10 m^2) into account, the leakage rate is approximately 1,034 tonnes/yr and 741 tonnes/yr. In the context of long term risk assessment, this leakage rate for 100 years would yield 0.1 and 0.07 million tonnes of escaped CO_2, approximated to 0.52% and 0.37% for a typical 20 million tonnes of stored CO_2, well below the 1% target. This result is sensitive to the area of the fault and to attenuation to intersecting permeable layers among other factors.

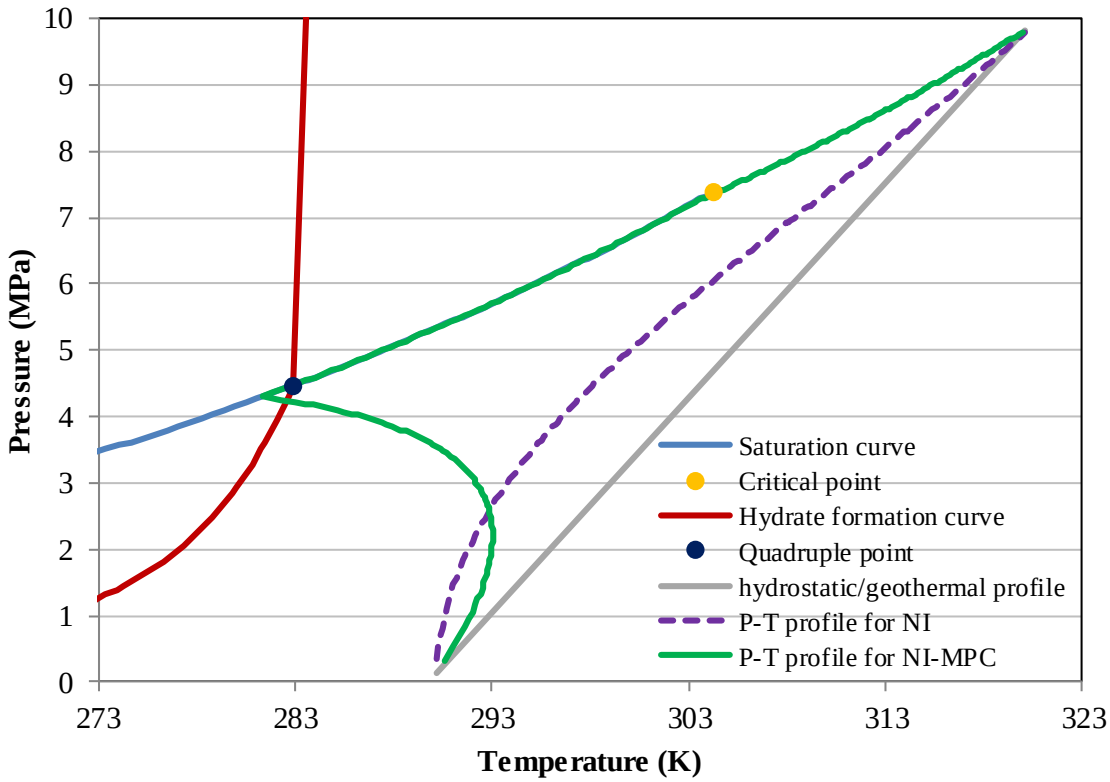

Figure 4.4: Phase diagram of CO_2-H_2O mixture is shown here along with the pressure-temperature profile in the fault for the geothermal case (NI) (dashed purple curve) and for the flowing total enthalpy case (NI-MPC) (green curve). Liquid and gas phases will coexist along the saturation curve as shown by the blue curve. The hydrate formation condition for CO_2-H_2O mixtures is shown by the red curve. The quadruple point (dark blue) for the CO_2- H_2O mixture where four phases exist: CO_2 in liquid, gas and hydrate phases and an aqueous phase coexist. The gray line shows the hydrostatic pressure – geothermal temperature profile.

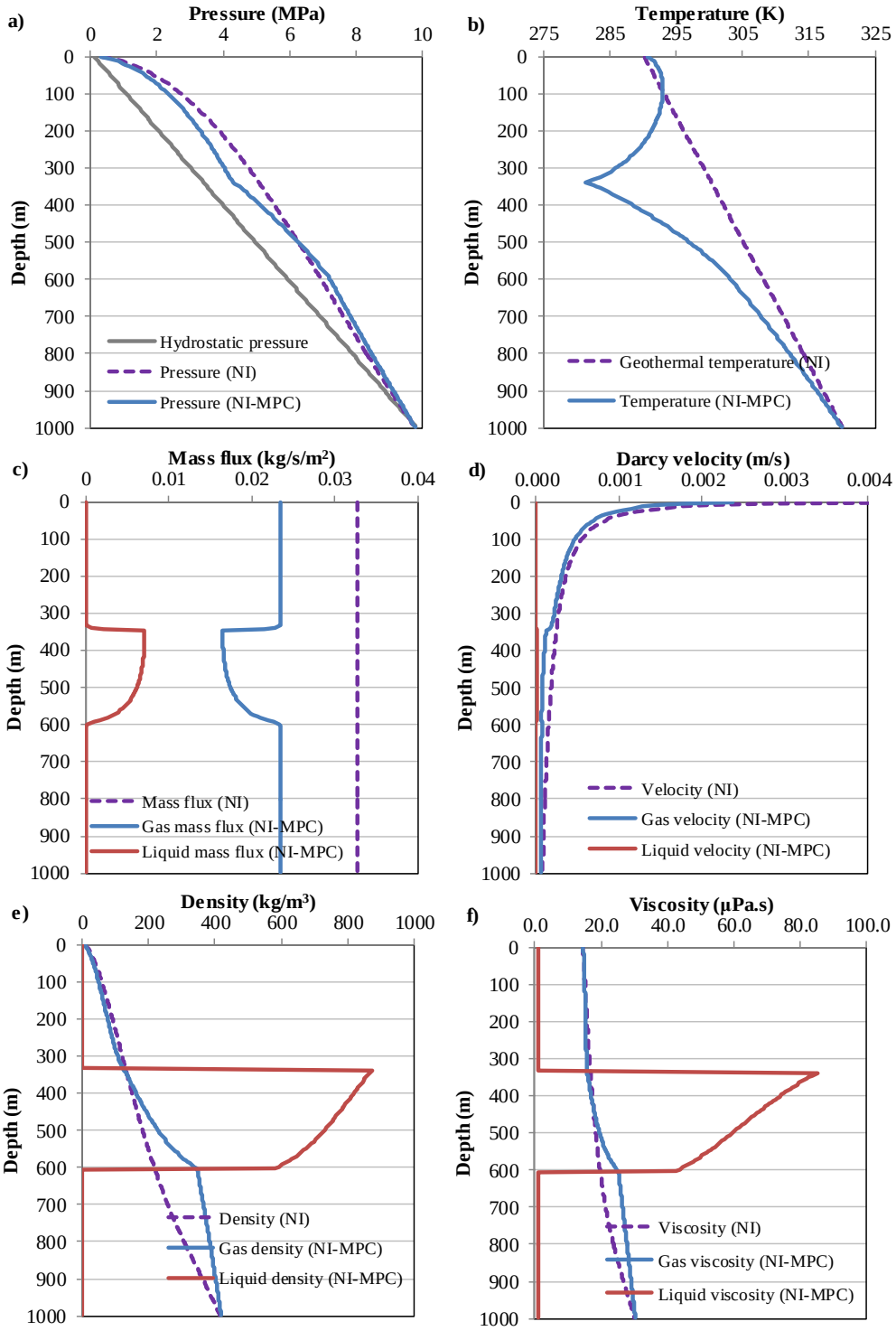

Figure 4.5: depth profile plots for both situations a) pressure profile, b) temperature profile, c) mass flux, d) Darcy velocity, e) density, f) viscosity.

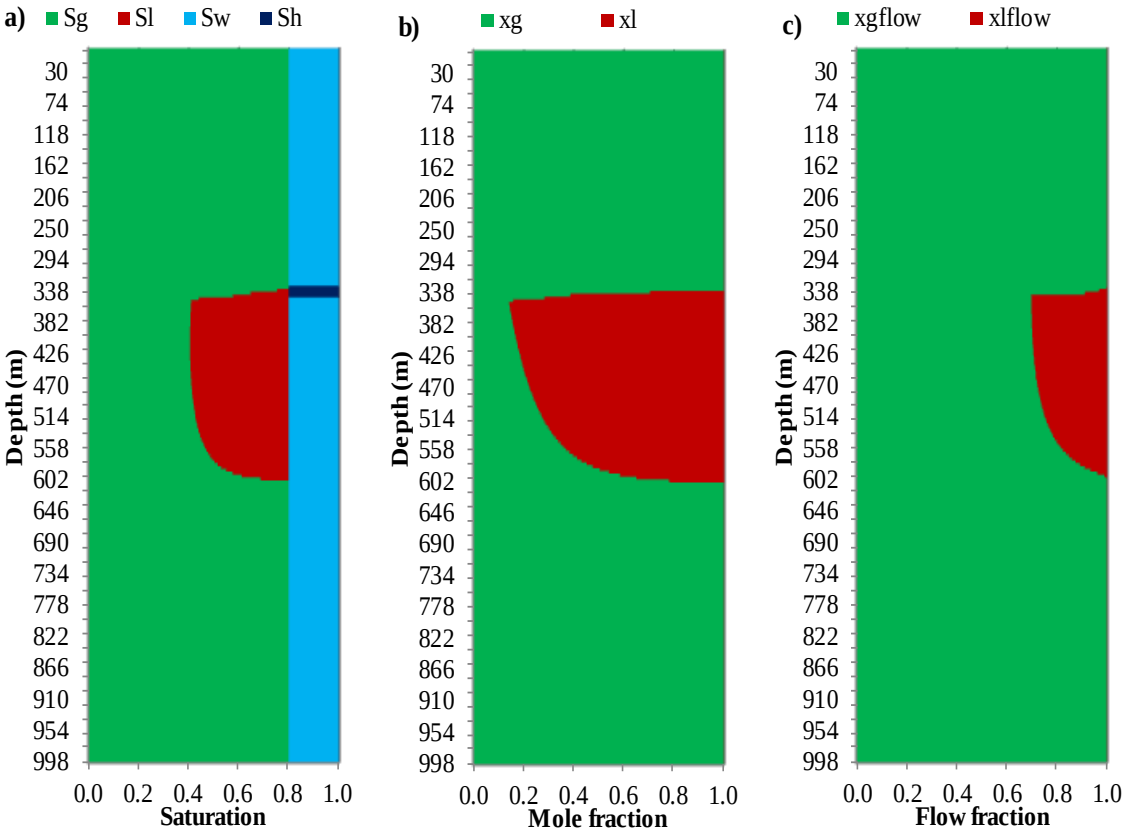

Figure 4.6: a) saturations as a function of depth, b) gas and liquid mole fraction of CO_2 as a function of depth, c) gas and liquid flow fraction as a function of depth.

4.4 Effect of Key Parameters on Leakage Mass Flux

Several factors affect the leakage mass fluxes. They can be divided into three groups. The first one deals with the initial conditions in the fault such as the water saturation, initial pressure and temperature at the base of the fault and overpressure associated with injection and storage. The second one deals with the fault geometry and rock properties such as permeability of the fault, fault effective width and fault length. These parameters can vary with depth. The third one deals with modelling approaches used to obtain the flux estimates such as, the relative permeability models used in the two

phase regions, the constant flowing total enthalpy assumption and its deviations after hydrate formation. It is instructive to consider variations in these parameters to evaluate their impact on steady state leakage mass fluxes. This is discussed in this section.

4.4.1 Overpressure

The CO_2 storage reservoir is typically at hydrostatic pressure. The pressure in the reservoir increases during injection assuming no production or leakage. This pressure increase is called overpressure. Calculations are performed for a wide variety of overpressure scenarios keeping all other parameters same as the base case. The goal of this analysis is to quantify the effect of overpressure on steady-state leakage mass flux and the multiphase depths and lengths. This will also help determine injection strategy that will yield the minimum leakage if any. This section will show the comparison of steady state leakage mass fluxes from three different approaches namely, 1) isothermal model, 2) geothermal case and 3) flowing total enthalpy case.

Increase in overpressure increased the leakage mass flux. The flux increased by up to 35% at 400 psi overpressure compared with the no overpressure for the geothermal case as shown in Figures 4.7a and 4.7b. This increase will also depend on the temperature in the fault (controlled by the geothermal gradient) and the depth of fault (depends on the storage reservoir location). Besides the concerns with respect to the unintended fracturing, higher rate of injection will increase the overpressure and the leakage mass flux. It is preferable to inject slower and longer than faster and shorter when concerned about minimizing the leakage mass flux. Thus, reservoir pressure management plays an active role to minimize leakage mass flux.

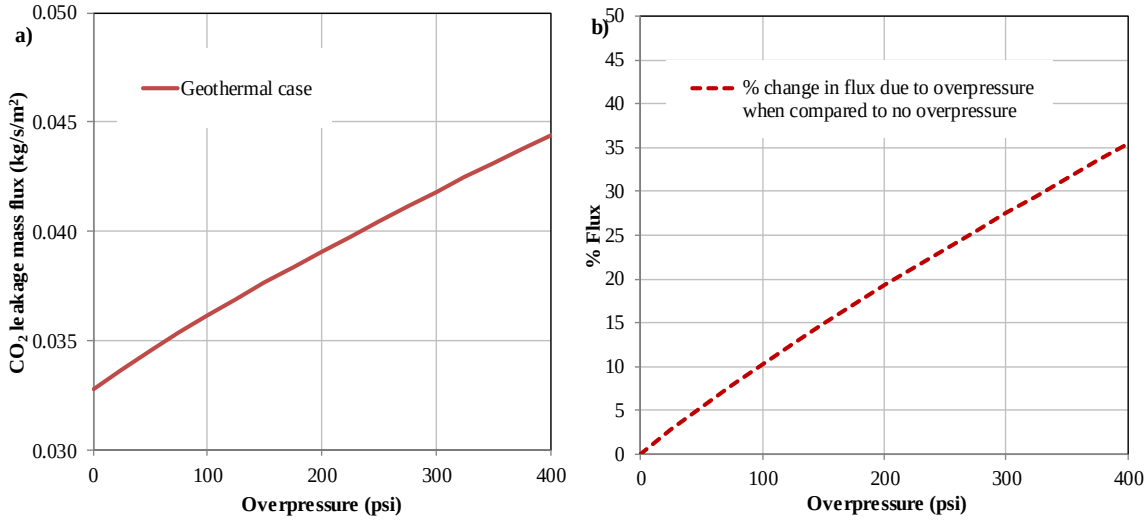

Figure 4.7: a) Leakage mass flux as a function of overpressure from the geothermal case, b) the % change in flux due to overpressure compared to no overpressure.

A comparison of leakage mass fluxes from the isothermal model and geothermal case for different overpressures are shown in Figure 4.8a. As observed in the base case results, the estimates from geothermal case decreased the estimated leakage mass flux by 33% when compared to isothermal model at no overpressure. With the increase in overpressure, the percentages increased to nearly 40% for the geothermal case at 400 psi overpressure as shown in Figure 4.8b. The decrease is primarily due to the non-linear variation of CO_2 properties such as density and viscosity in the fault. The isothermal model overestimated the steady state leakage mass flux and the direct consequences of such overestimation are

1) The risk associated with leakage is overestimated affecting the site selection process
2) The leakage pathway properties such as effective permeability are underestimated during field data analysis.

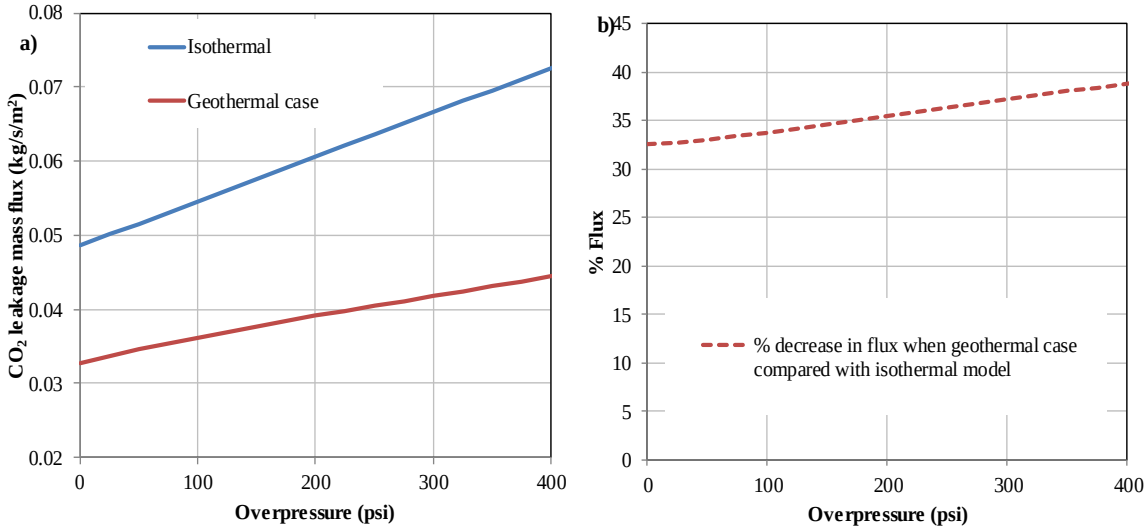

Figure 4.8: a) Leakage mass flux as a function of overpressure from estimation approaches (isothermal - blue, geothermal case - red), b) the % decrease in flux as a function of overpressure when using geothermal case when compared to isothermal model

The effect of multiphase coexistence is quantified by comparison between the leakage mass fluxes estimated from the geothermal case and flowing total enthalpy case for different overpressures as shown in Figure 4.9a. The percent decrease has a non-linear behavior with the increase in overpressure. The presence of multiphase regions decreased the leakage mass flux by 27 % when compared to the geothermal case at no overpressure. As the overpressure increased, the percentages increased to 37 % at 200 psi overpressure and decreased as shown in Figure 4.9b. The cumulative leakage for 100 years as a percent of CO_2 stored for a typical storage amount of 20 million tonnes is shown in Figure 4.9c. The increase in cumulative leakage with overpressure further emphasized the importance of reservoir pressure management during long term storage. A comparison of the numerical simulations results from Chapter 3 with results obtained from the steady-state flow model (SSFM) is shown in Figure 4.9d. The difference is less than 5 % when the results from geothermal case from SSFM are compared with the numerical maximum

flux results. The difference is less than 10 % when the results from the flowing total enthalpy case from SSFM are compared with the numerical results for first instance of hydrate formation. This is primarily due to the difference in the size of the hydrate regions between the models (SSFM is larger).

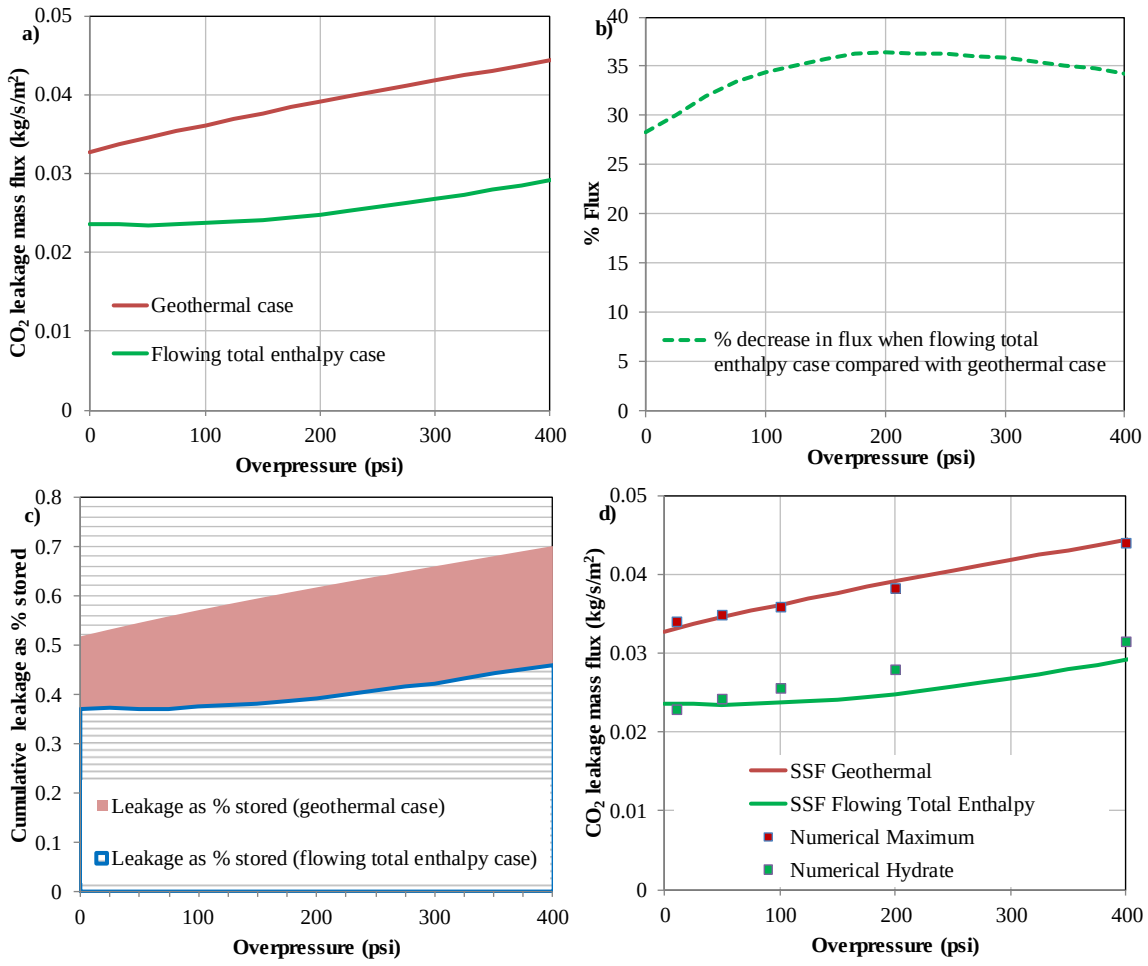

Figure 4.9: a) Leakage mass flux as a function of overpressure from estimation approaches (geothermal case – red, flowing total enthalpy case - green), b) The % decrease in flux as a function of overpressure due to maximum multiphase coexistence c) Cumulative leakage as a % of CO_2 stored for both cases d) Comparison of results obtained from this steady-state flow model (SSF) with the numerical model (Numerical) developed on chapter 2.

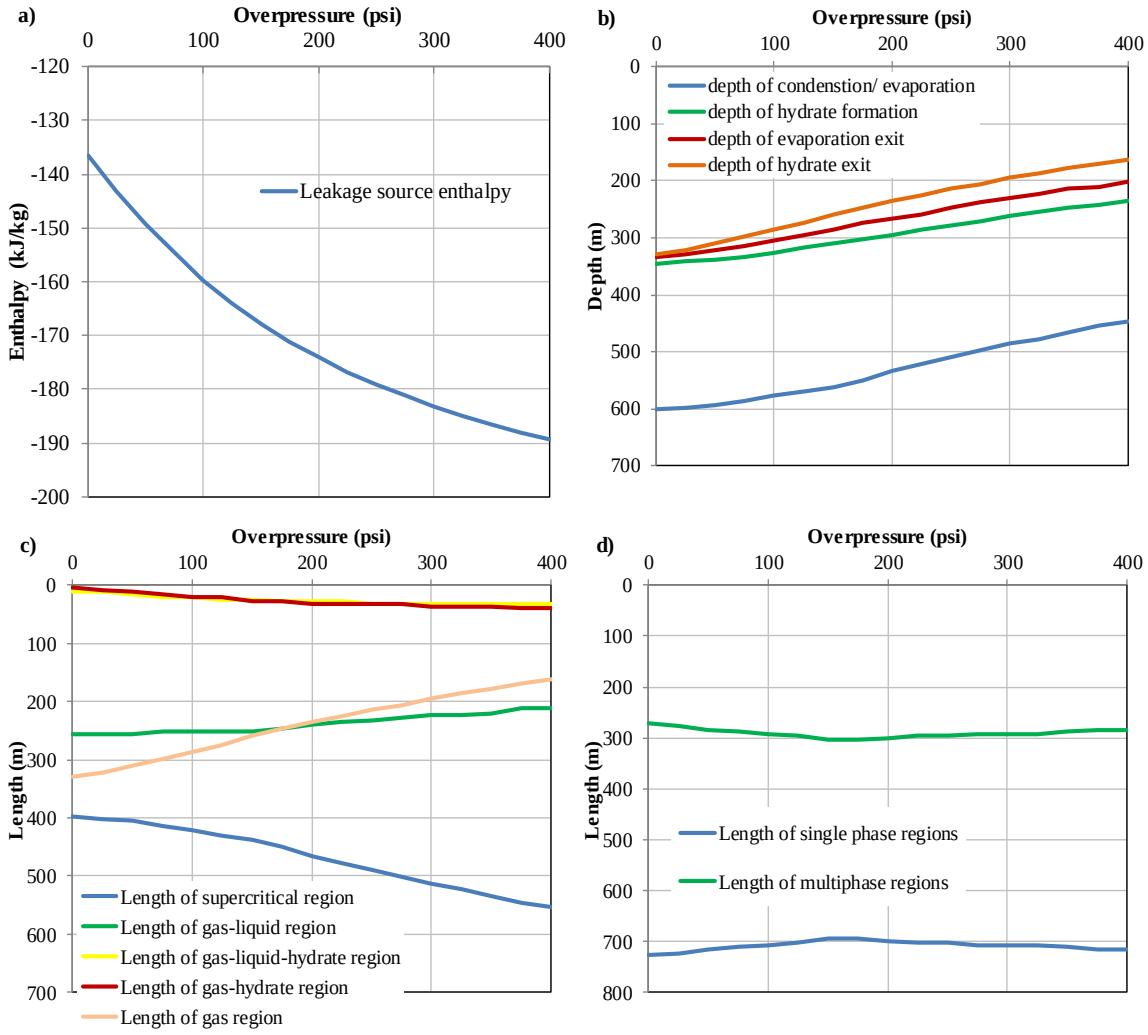

Figure 4.10: a) leakage source enthalpy as a function of overpressure, b) depth of phase changes as a function of overpressure, c) the length of the multiphase regions as a function of overpressure, d) the total length of single phase regions and multiphase regions as a function of overpressure

The non-linear nature of the percent decrease in flux with increase in overpressure as shown in Figure 4.9b is investigated here. The leakage source enthalpy is shown in Figure 4.10a. The depth at which the multiphase regions exist, lengths of the each multiphase region and the total length of single phase and multiphase regions are shown in Figure 4.10b, 4.10c and 4.10d, respectively. The leakage source enthalpy decreased

with the increase in overpressure. This resulted in an increase in the liquid flow fraction in gas-liquid region, decrease in the hydrate exit pressure and increase in the length of the hydrate regions. The overall length of the single phase regions decreased and the length of the multiphase regions increased until around 200 psi overpressure. This is a major factor in the increase in the percent decrease of flux when compared to geothermal case. Beyond 200 psi of overpressure, the length of the single phase regions increased and the length of the multiphase regions decreased. This resulted in the decrease in the percent decrease of flux compared to geothermal case.

4.4.2 Temperature Gradient in the Fault

The temperature gradient in the fault will control the temperature distribution in the direction of flow and the storage reservoir temperature. This property is by virtue of the geological location. A sensitivity study is performed to estimate its effect on steady state leakage mass flux for a wide variety of overpressure scenarios and temperature gradients keeping all other parameters same as the base case.

Increase in geothermal gradient increased the leakage mass flux for all overpressures as shown in Figures 4.11a and 4.11b. The effect of multiphase coexistence decreased with the increase in geothermal gradient for all overpressures when compared with the flux obtained from geothermal case as shown in Figure 4.11c. The cumulative leakage for 100 years as a percent of CO_2 stored for a typical storage amount of 20 million tonnes for all overpressures is shown in Figures 4.13a-e. The leakage risk increased with the overpressure and geothermal gradient.

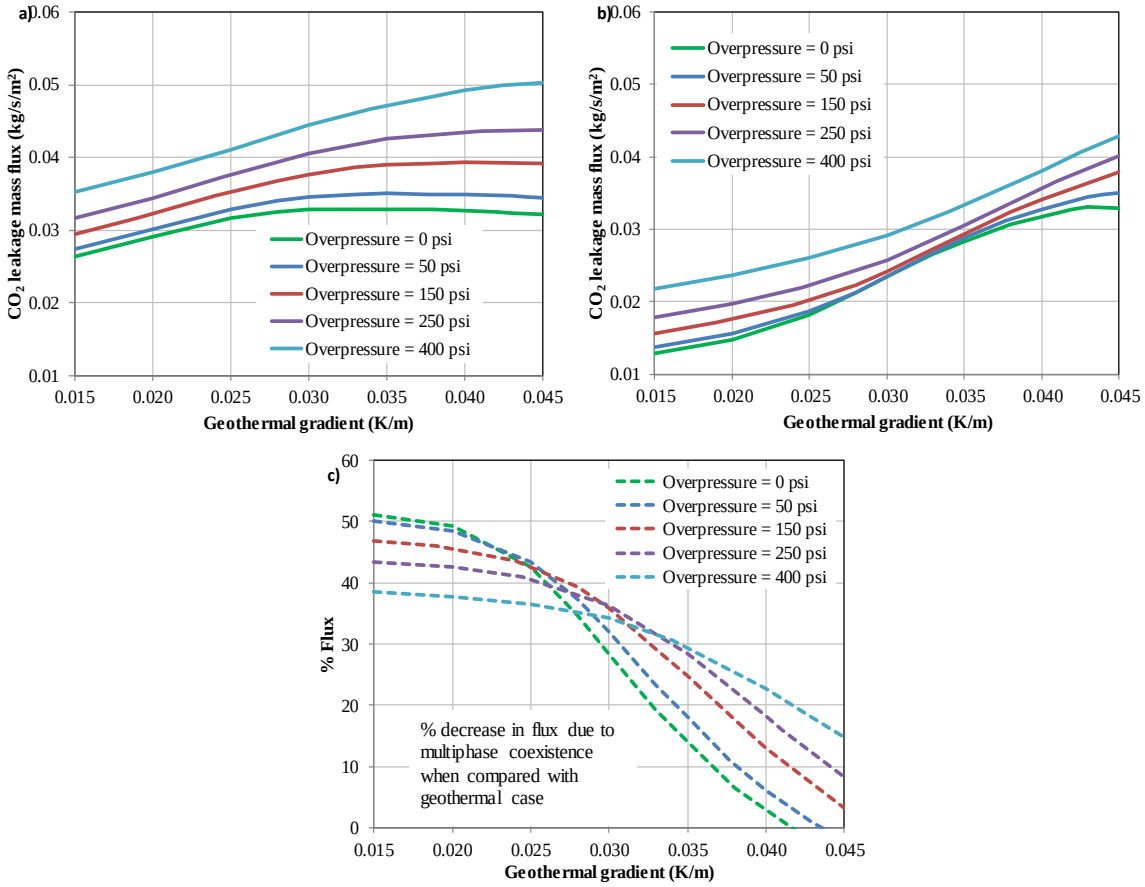

Figure 4.11: a) Leakage mass flux as function of geothermal gradient for various overpressures for geothermal case, b) Leakage mass flux as function of geothermal gradient for various overpressures for flowing total enthalpy case, c) The % decrease in flux as a function of geothermal gradient for various overpressures due to maximum multiphase coexistence.

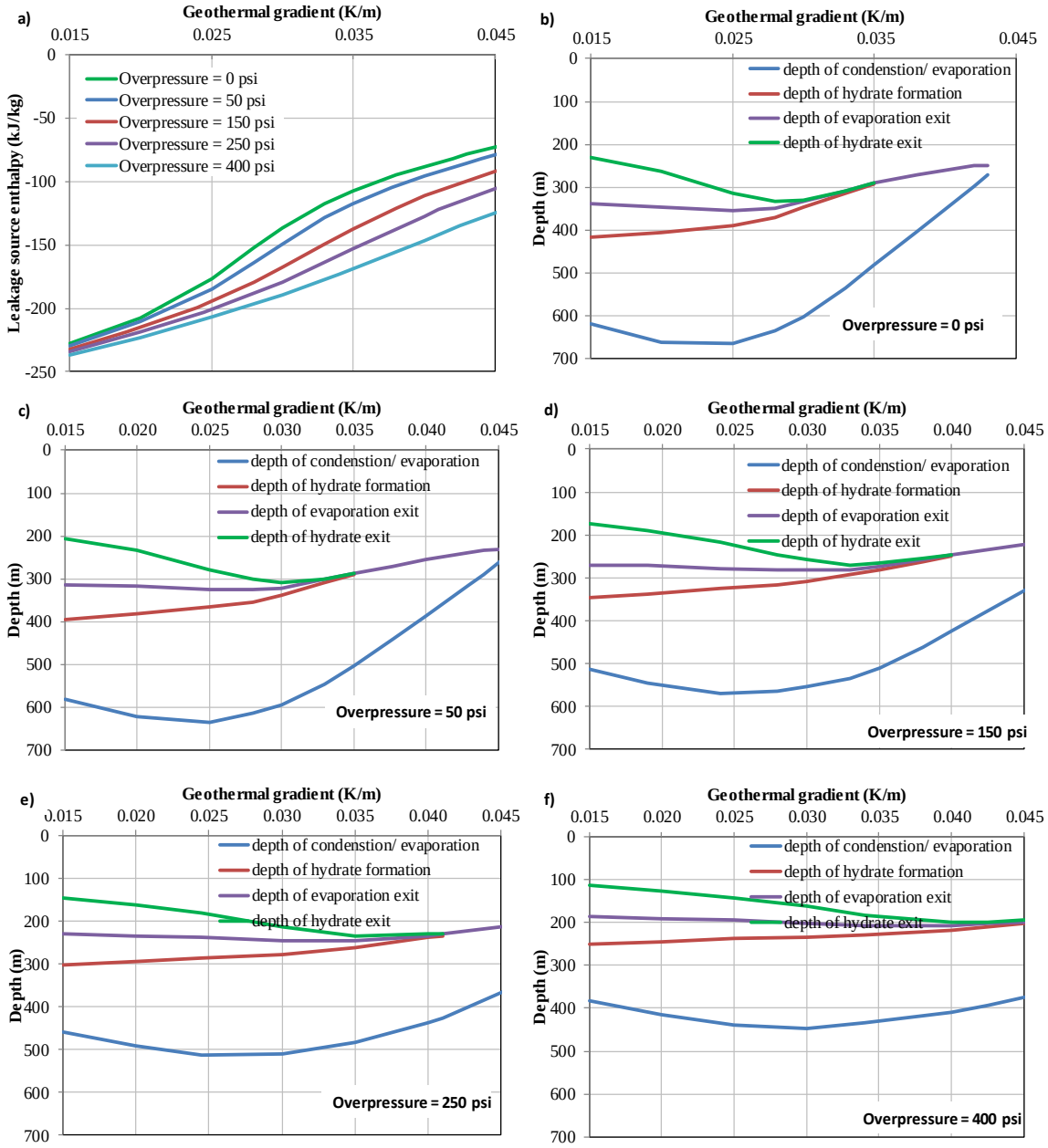

Figure 4.12: a) leakage source enthalpy as a function of geothermal gradient with various overpressures, b) phase change depths for overpressure = 0 psi, c) phase change depths for overpressure = 50 psi, d) phase change depths for overpressure = 150 psi, e) phase change depths for overpressure = 250 psi, f) phase change depths for overpressure = 400 psi.

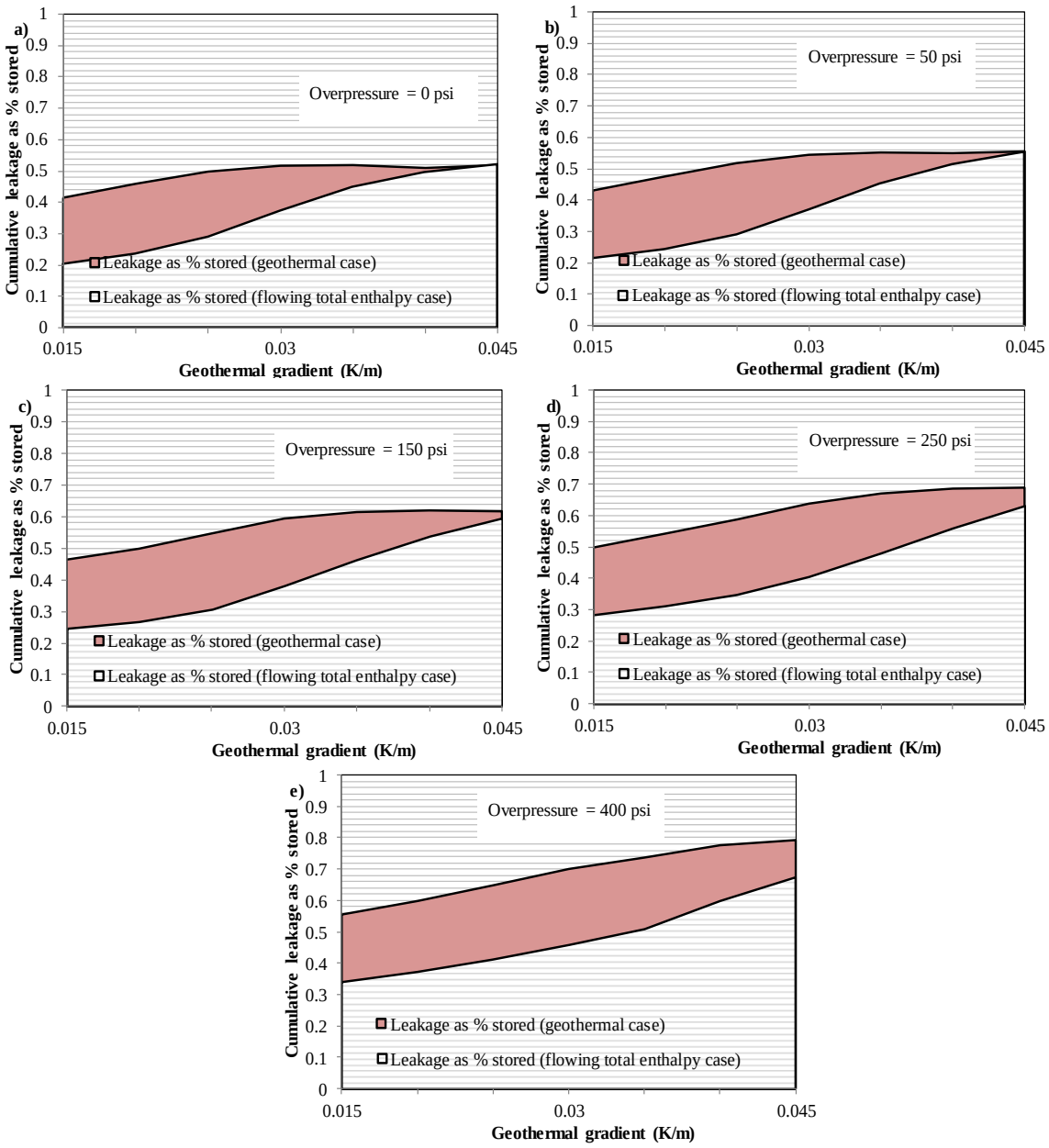

Figure 4.13: Cumulative leakage as a % of CO_2 stored with both cases as upper and lower bounds of the shaded region for varied geothermal gradient and different overpressures a) overpressure = 0 psi, b) overpressure = 50 psi, c) overpressure = 150 psi, d) overpressure = 250 psi, e) overpressure = 400 psi.

The effect of multiphase coexistence was larger in the colder reservoirs with up to 50% decrease in flux whereas it was less than 20% in the warmer reservoirs. With increase in geothermal gradient and consequently reservoir temperature, the leakage source enthalpy increased as shown in Figure 4.12a. At low geothermal gradients, the leakage source enthalpy was low; flow fraction was liquid-dominated and had low hydrate exit pressure which resulted in longer multiphase regions and lower flux as shown in Figure 4.12. As geothermal gradient increased, enthalpy increased, flow fraction was gas-dominated and had high hydrate exit pressure which resulted in shorter multiphase regions and higher flux. Colder reservoirs with colder geology above the reservoir have lower flux than warmer reservoirs with warmer geology above primarily due to denser and more viscous CO_2. Thus, knowledge of geothermal gradient will be critical during the site-selection phase and storage reservoirs can be chosen based on the temperature in and above the reservoir to minimize leakage mass flux.

4.4.3 Depth

Depth of the reservoir controls the pressure and temperature at the base of the fault (reservoir) besides the length of the fault. This property is by virtue of the location of storage reservoir. A sensitivity study is performed on this property to estimate its effect on steady state leakage mass flux for a wide variety of overpressure scenarios and depth keeping all other parameters same as the base case.

For all overpressures, increase in depth (> 1000 m) decreased the leakage mass flux for geothermal case and increased for flowing total enthalpy case as shown in Figures 4.14a and 4.14b.The effect of multiphase coexistence was minimal with an increase in depth as shown in Figure 4.14c. As the fault depth increased, the pressure and

temperature at the base of the fault increased. This resulted in an increase in the leakage source enthalpy as shown in Figure 4.15a. The leakage source enthalpy has a non-monotonic relationship with fault depth. The lengths of the multiphase regions were short at low depths. And as the depth increased till 1100m, the length of these regions increased which resulted in a decrease in the flux. After 1100m, the lengths of the multiphase regions remain almost constant which resulted in an increase in the flux due to increase in pressure at the base of the fault. The cumulative leakage for 100 years as a percent of CO_2 stored for a typical storage amount of 20 million tonnes for all overpressures is shown in Figures 4.16 a-e. The leakage risk decreased with the increase in depth beyond 1100m for all overpressure scenarios.

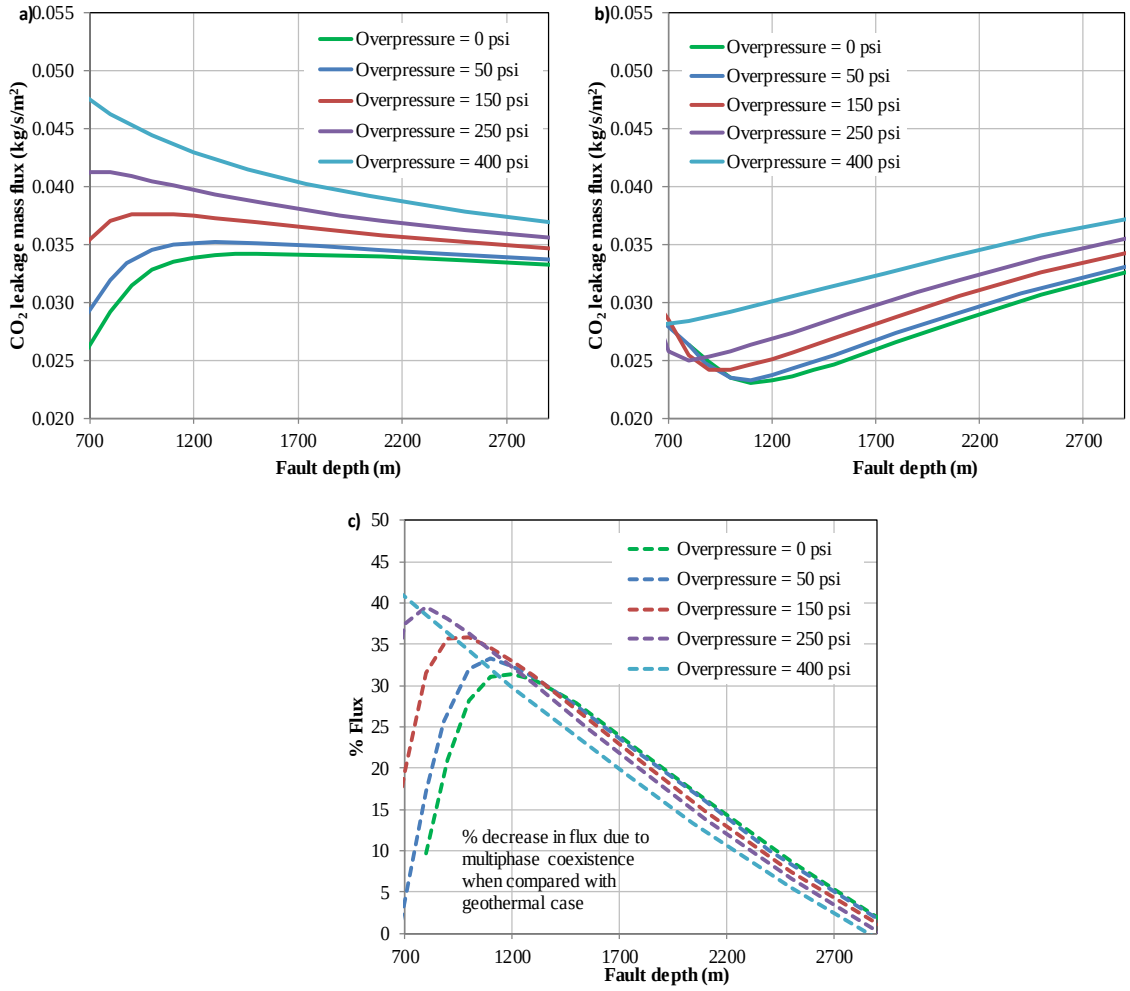

Figure 4.14: a) Leakage mass flux as function of depth for various overpressures for geothermal case, b) Leakage mass flux as function of depth for various overpressures for flowing total enthalpy case, c) The % decrease in flux as a function of depth for various overpressures due to maximum multiphase coexistence

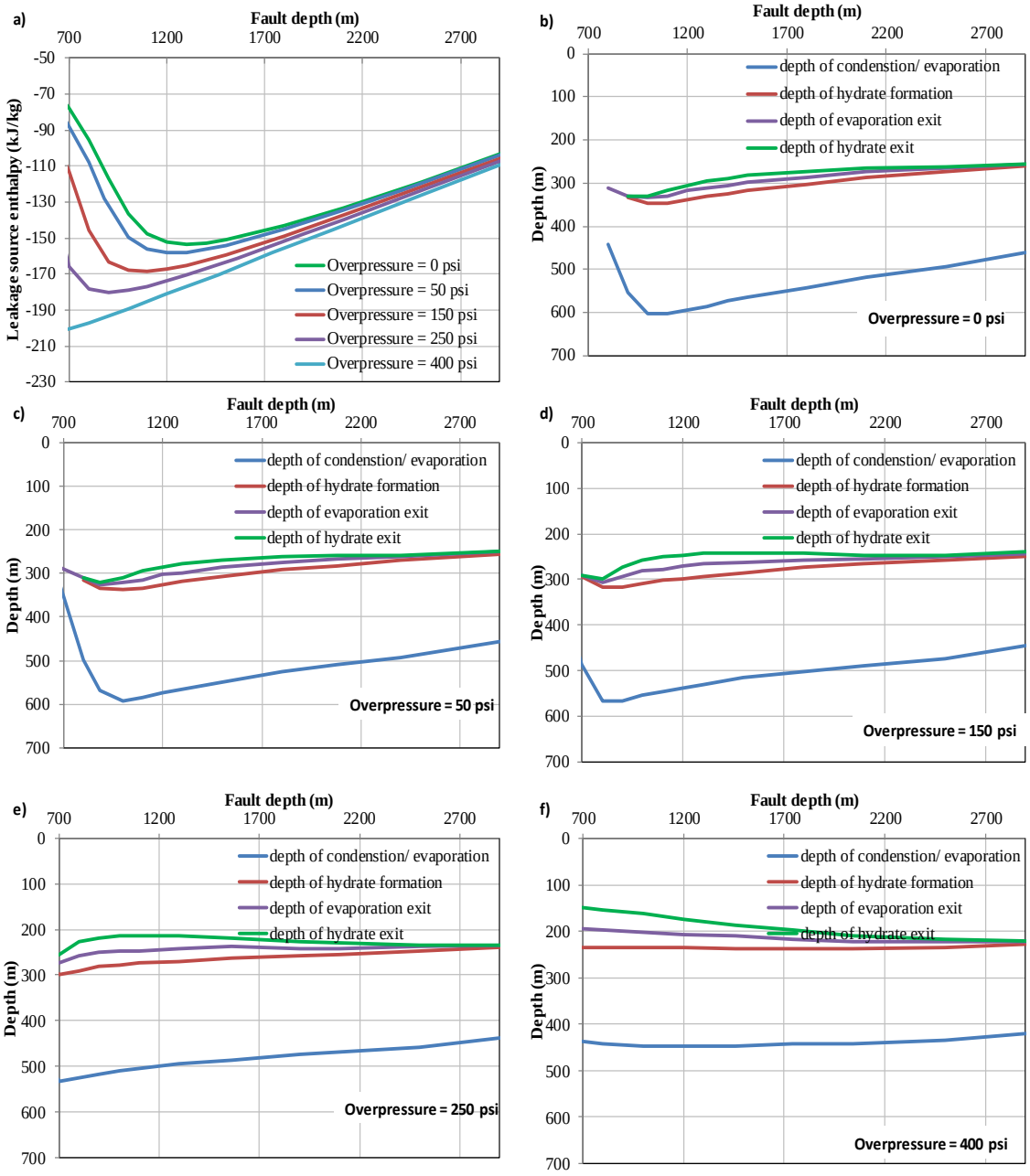

Figure 4.15: a) leakage source enthalpy as a function of depth with various overpressures, b) phase change depths for overpressure = 0 psi, c) phase change depths for overpressure = 50 psi, d) phase change depths for overpressure = 150 psi, e) phase change depths for overpressure = 250 psi, f) phase change depths for overpressure = 400 psi.

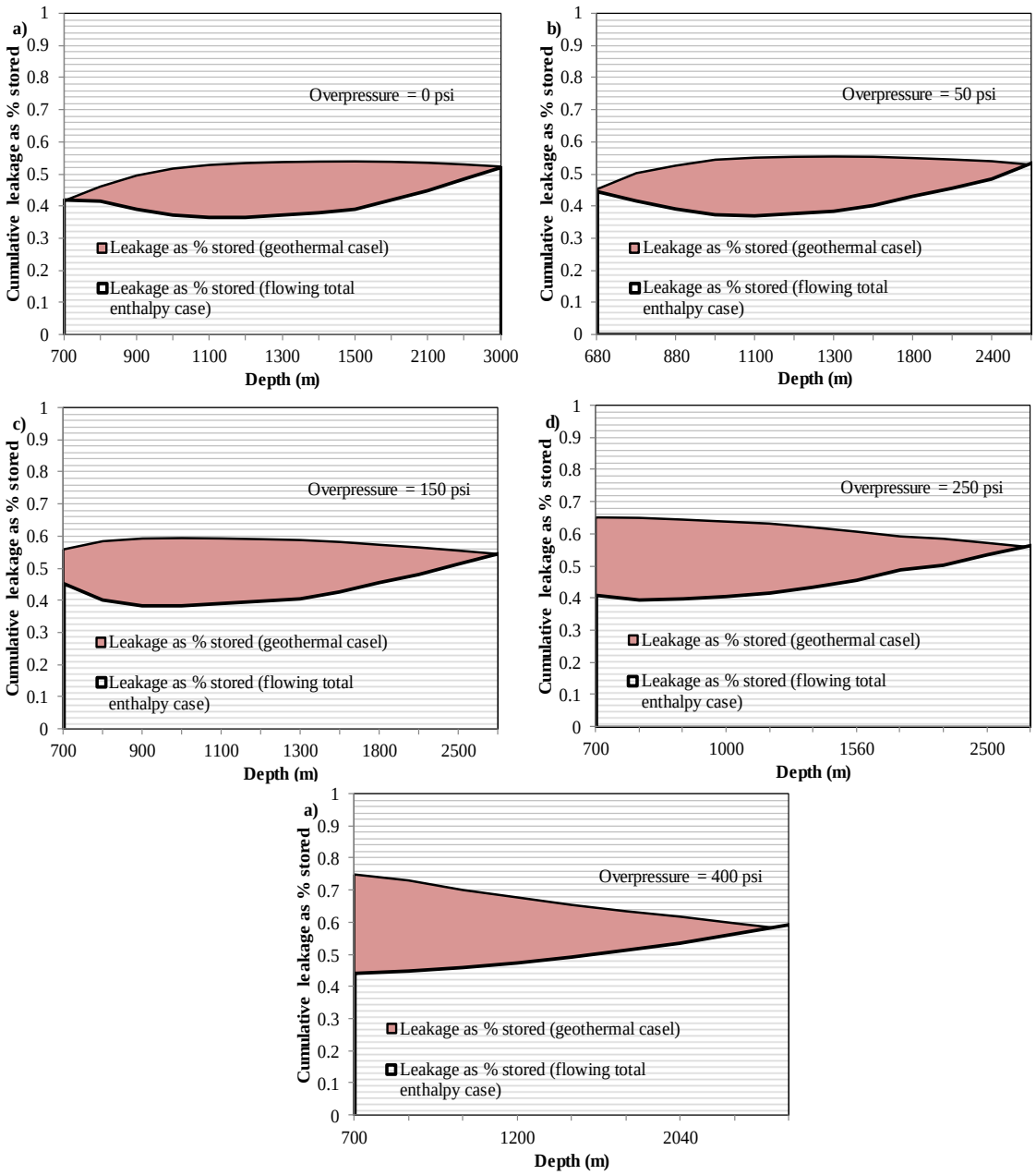

Figure 4.16: Cumulative leakage as a % of CO_2 stored with both situations as upper and lower bounds of the shaded region for varied depth and different overpressures a) overpressure = 0 psi, b) overpressure = 50 psi, c) overpressure = 150 psi, d) overpressure = 250 psi, e) overpressure = 400 psi.

4.4.4 Permeability

Permeability has a first order effect on leakage mass flux. Leakage mass flux increased in a linear fashion with the increase in permeability for both cases as shown in Figure 4.17. A sensitivity study was performed on this property to estimate its effect on steady state leakage mass flux keeping all other parameters same as the base case. The variation in permeability does not affect the fluid properties. For an order of magnitude permeability increase, the leakage mass flux increased by a factor of 10. For comparison, the leakage mass flux from natural analogues discussed in Chapter 1 along with CO_2 background flux at earth's surface (0.2 mg/m^2/s) (Allis et al., 2005) is shown here. The intention here is to set the calculated fluxes in context with naturally occurring fluxes and not to comment on whether the values are large or small enough to neglect compared to naturally occurring fluxes. This context provides the confidence that the leaks can be identified during monitoring for permeability greater than 0.01 md. Comparison of a heterogeneous fault case is shown in Figure 4.18.

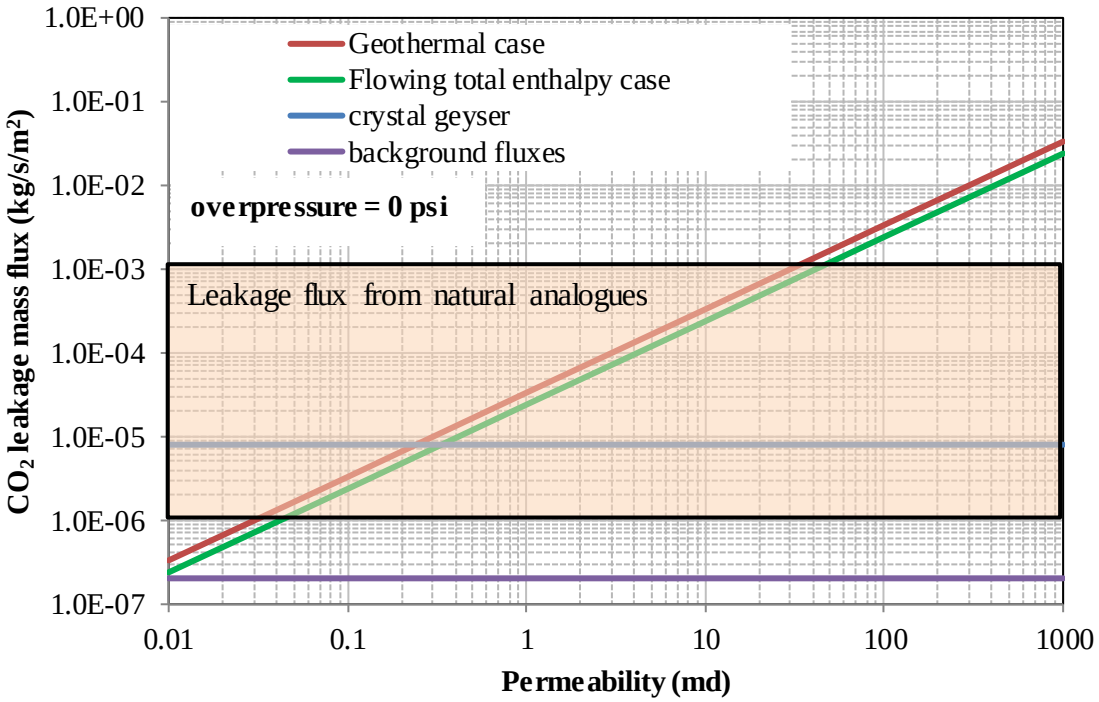

Figure 4.17: Steady state leakage mass flux as a function of permeability for two estimation approaches for the specified overpressure scenario of 0 psi.

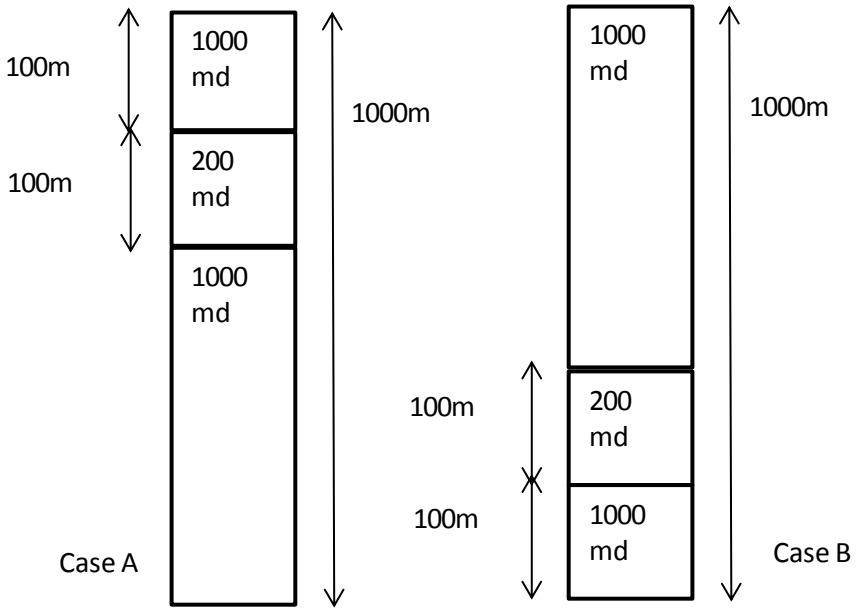

Figure 4.18: Schematic description of two variable permeability cases.

Two variable permeability cases are shown in Figure 4.18. A low-permeability layer of 200 md in 100 m length is situated close to the surface in Case A and close to leakage source in Case B. The rest of the parameters are kept the same as the base case such as no overpressure. The estimated leakage mass flux is shown in Table 4.3. The major conclusion is that low permeability layer close to the surface has a larger impact on leakage mass flux in both situations than the layer close to the leakage source. Thus, accounting for permeability variations will be extremely important from a leakage mass flux estimation standpoint.

Table 4.3: Leakage mass flux estimated for variable permeability case

Estimation approach	Leakage mass flux ($kg/s/m^2$)			% decrease from base case	
	Case A	Case B	Base case	Case A	Case B
Geothermal case	0.0219	0.0247	0.0328	33.24	24.82
Flowing total enthalpy case	0.0140	0.0188	0.0235	40.52	20.17

4.4.5 Enthalpy Exponent

Enthalpy exponent is a useful parameter to control the length of hydrate regions. This parameter is an empirical construct based on the observation from the numerical model results. When enthalpy exponent increased, the pressure at the hydrate exit became lower as shown in Figure 4.2. Decrease in leakage source enthalpy also resulted in the decrease of hydrate exit pressure. The lowering of hydrate exit pressure result in an increase in the length of hydrate regions for different overpressure values as shown in Figures 4.19b-f, which adversely affected the flux as observed in Figure 4.19a.

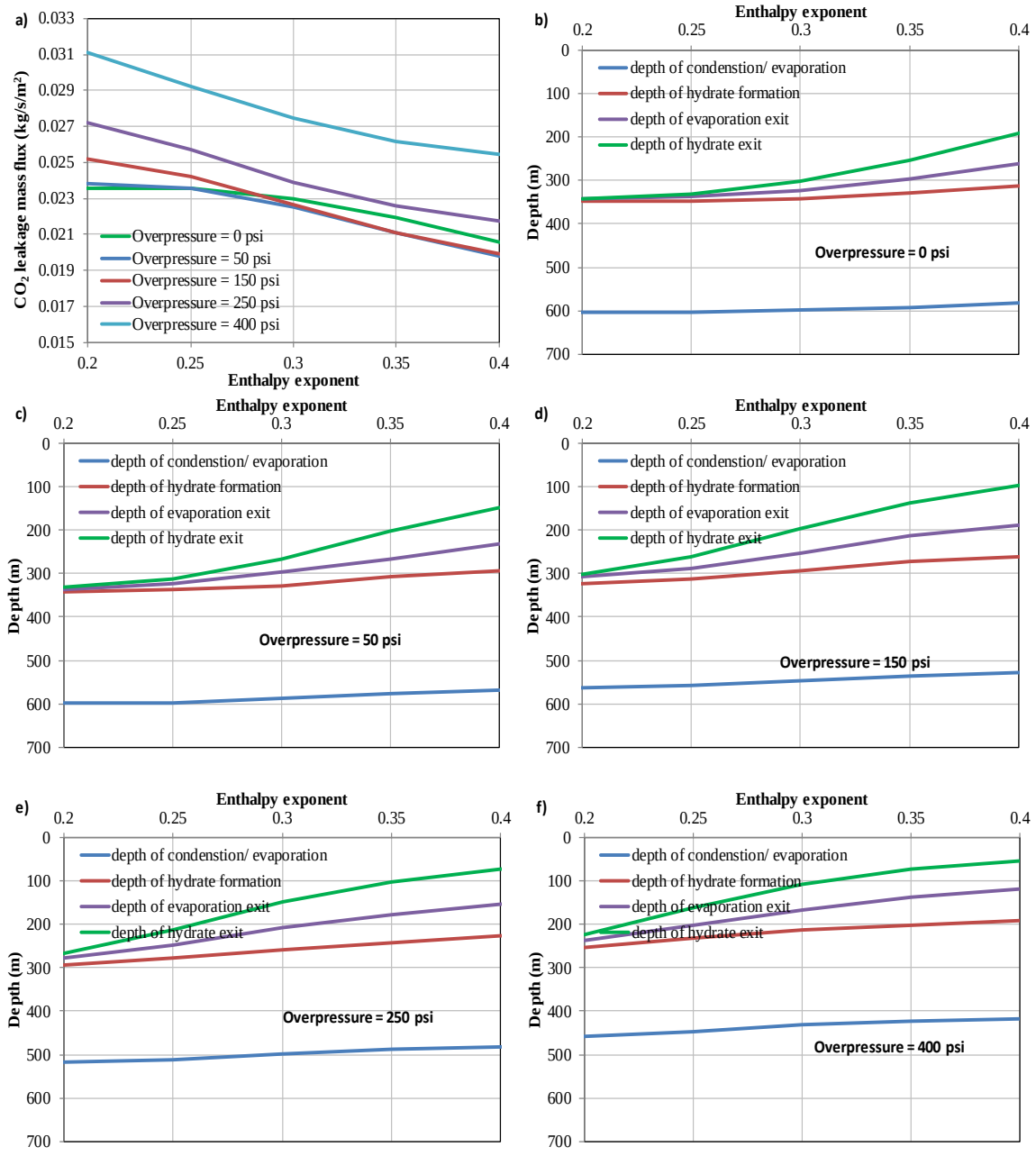

Figure 4.19: A sensitivity analysis for enthalpy exponent term. a) steady state leakage mass flux as a function of enthalpy exponent for five different overpressures, b) phase change depths for overpressure = 0 psi, c) phase change depths for overpressure = 50 psi, d) phase change depths for overpressure = 150 psi, e) phase change depths for overpressure = 250 psi, f) phase change depths for overpressure = 400 psi.

4.5 SUMMARY

A steady-state flow model (SSFM) was developed for quick estimation of leakage mass flux through faults and fractures as shown in Chapter 4. The model is highly simplified and is intended for inclusion in risk assessment studies at the site-selection phase for geologic storage. The leakage mass fluxes are calculated assuming two different conditions (1) The temperature of the CO_2 was assumed to be the same as the surroundings based on an assumed geothermal gradient and (2) The temperature of the CO_2 was calculated from the constant flowing total enthalpy specified at the leakage source. The enthalpy is constant when there are no heat losses (adiabatic system). The resulting estimates act as upper and lower bounds for leakage mass flux for a particular set of physical properties of the pathway and surrounding geology. A highly idealized representation of the fault is used to capture the interplay between several factors affecting leakage.

For the particular conditions used to calculate the steady state leakage mass flux illustrated in Chapter 4, liquid-CO_2 and CO_2-hydrate formation in the fault reduced the mass flux by 50% assuming constant enthalpy and 33% assuming a geothermal temperature gradient compared to isothermal flow. The isothermal flow model overestimated the steady state leakage mass flux. Direct consequences of such overestimation are 1) the risk associated with leakage is overestimated affecting the site selection process and 2) the leakage pathway properties such as effective permeability are underestimated during field data analysis. The difference was less than 5% when the leakage mass flux from geothermal case was compared with the numerical maximum mass flux results in Chapter 3. The difference was greater than 10% when the leakage mass flux from the flowing total enthalpy case was compared with the numerical results for first instance of hydrate formation. This was primarily due to the difference in the size

of the hydrate regions between the models (SSFM was larger). From a purely mass flux estimation perspective, the SSFM is more useful than the numerical model.

A higher geothermal gradient increased the leakage mass flux for all overpressures. The leakage risk increased with the overpressure and geothermal gradient. The effect of multiphase coexistence was more pronounced in the colder reservoirs with up to 50% decrease in mass flux whereas it was less than 20% in the warmer reservoirs when compared to the geothermal case. Thus, knowledge of geothermal gradient will be important during the site-selection phase and storage reservoirs could be chosen in part based on the temperature in and above the reservoir to minimize leakage mass flux. Depth of the reservoir controls the pressure and temperature at the base of the fault (reservoir). For all overpressures, increase in depth (> 1000 m) decreased the leakage mass flux for geothermal case and increased for flowing total enthalpy case. The leakage risk decreased with the increase in depth beyond 1100 m for all overpressure scenarios.

Increase in overpressure increased the leakage mass flux. For geothermal case, the leakage mass flux increased by up to 35% at 400 psi overpressure when compared to no overpressure scenario. The presence of multiphase regions decreased the leakage mass flux by up to 30% when compared to the geothermal case. Permeability has a first order effect on leakage mass flux. Leakage mass flux increased linearly with the increase in permeability for both cases. The variation in permeability does not affect the fluid properties. For an order of magnitude permeability increase, the leakage mass flux increased by a factor of 10. Low permeability layer close to the surface has a larger impact on leakage mass flux in both cases than the layer close to the leakage source for heterogeneous fault scenario.

Chapter 5: Summary, Conclusions and Future Work

5.1 Summary and Conclusions

The biggest risk associated with geological storage of CO_2 is the possibility of leakage. Leakage has potentially detrimental consequences on the environment and human health which could impact the viability of the chosen storage formation. The leakage pathways such as faults/fracture and leaky wellbores enable CO_2 to migrate out of intended storage formation through the subsurface towards the atmosphere. Non-isothermal multiphase flow is likely because of large spatial gradients in pressure and temperature when CO_2 flows toward the surface with the possibility of liquid condensation and hydrate formation. As a consequence, the fluid and flow properties will change and affect leakage mass flux. It is important to estimate leakage mass fluxes to perform risk assessment and understand leakage behavior to develop better monitoring strategies.

The main goal of this dissertation research was to develop and test models needed to estimate the leakage mass flux for different scenarios taking thermodynamic phase changes into account. Specifically, the leakage through faults was modelled. A non-isothermal, quasi-1D numerical model was developed to estimate the leakage mass flux as a function of time. Mass flux was allowed only in the vertical direction. The conductive heat flux was accounted for in the direction perpendicular to flow. The model description, equations and solutions methods are discussed in Chapter 2. A highly idealized representation of a fault was used to capture the coupled effect of the thermal and multiphase flow aspects of leakage. Simulation results reveal how the fault properties combine with reservoir overpressure to affect CO_2 leakage.

For the particular conditions used to calculate the CO_2 leakage mass flux illustrated in Chapter 3, liquid-CO_2 condensation and CO_2-hydrate formation occurred because of the decreasing temperature and pressure as CO_2 migrated up in the fault. Decompression near the critical pressure of CO_2 resulted in a strong cooling effect which reduced CO_2 temperature enough to reach gas-liquid coexistence conditions. The mobility of the CO_2 initially decreased when CO_2 condensation occurred based on the assumed relative permeability curves. Heat gain from the surrounding rock eventually evaporated the liquid CO_2 resulting in an increase in mobility and leakage mass flux. The CO_2 phase changes (gas to gas-liquid to gas) caused the leakage mass flux to cycle, which led to cyclic variations in temperature, gas saturation and pressure. The time period and the amplitude increased with each successive cycle. Eventually hydrates formed in part of the fault. The hydrates further reduced the CO_2 mobility and leakage mass flux in a cyclic manner. The pressure increased at every depth when compared to the hydrostatic pressure and there was a significant temperature decrease in the multiphase regions. The maximum temperature decrease at each time occurred at the top of the two phase region with close to a 15 K decrease at the hydrate formation depth.

The pressure in the storage reservoir increases upon CO_2 injection. This pressure increase is termed as overpressure. Leakage mass fluxes increased about 29% with an overpressure of 400 psi. The mass flux decreased 30% for all cases at the first instance of hydrate formation. The time taken for the first instance of gas-liquid coexistence and hydrate formation decreased exponentially with an increase in overpressure. At higher overpressures (> 400 psi), the multiphase coexistence conditions were reached in less than 1 year. Thus, the effect of overpressure on leakage should be considered when managing a storage reservoir.

The fault permeability has a first order effect on leakage. The leakage mass flux increased in a linear fashion and the time taken to reach multiphase conditions decreased in a power law fashion with an increase in permeability. The leakage mass flux increased by a factor of 10 when the fault permeability was increased a factor of 10. The cooling effect and the cyclic nature of leakage are much less important for faults with low permeability. Condensation takes more than 100 years and hydrate formation takes more than 300 years for faults with a permeability less than 500 md. The time taken to reach multiphase flow conditions decreased in a power law fashion with the increase in fault effective width, but did not increase the leakage mass flux. Increase in fault effective width increased the convective energy flux in the fault and dominated the conductive heat flux to the surroundings and hence cooled faster.

A steady-state flow model (SSFM) was developed for quick estimation of leakage mass flux through faults and fractures as shown in Chapter 4. The model is highly simplified and is intended for inclusion in risk assessment studies at the site-selection phase for geologic storage. The leakage mass fluxes are calculated assuming two different conditions (1) The temperature of the CO_2 was assumed to be the same as the surroundings based on an assumed geothermal gradient and (2) The temperature of the CO_2 was calculated from the constant flowing total enthalpy specified at the leakage source. The enthalpy is constant when there are no heat losses (adiabatic system). The resulting estimates act as upper and lower bounds for leakage mass flux for a particular set of physical properties of the pathway and surrounding geology. A highly idealized representation of the fault is used to capture the interplay between several factors affecting leakage.

For the particular conditions used to calculate the steady state leakage mass flux illustrated in Chapter 4, liquid-CO_2 and CO_2-hydrate formation in the fault reduced the

mass flux by 50% assuming constant enthalpy and 33% assuming a geothermal temperature gradient compared to isothermal flow. The isothermal flow model overestimated the steady state leakage mass flux. Direct consequences of such overestimation are 1) the risk associated with leakage is overestimated affecting the site selection process and 2) the leakage pathway properties such as effective permeability are underestimated during field data analysis. The difference was less than 5% when the leakage mass flux from geothermal case was compared with the numerical maximum mass flux results in Chapter 3. The difference was greater than 10% when the leakage mass flux from the flowing total enthalpy case was compared with the numerical results for first instance of hydrate formation. This was primarily due to the difference in the size of the hydrate regions between the models (SSFM was larger). From a purely mass flux estimation perspective, the SSFM is more useful than the numerical model.

A higher geothermal gradient increased the leakage mass flux for all overpressures. The leakage risk increased with the overpressure and geothermal gradient. The effect of multiphase coexistence was more pronounced in the colder reservoirs with up to 50% decrease in mass flux whereas it was less than 20% in the warmer reservoirs when compared to the geothermal case. Thus, knowledge of geothermal gradient will be important during the site-selection phase and storage reservoirs could be chosen in part based on the temperature in and above the reservoir to minimize leakage mass flux. Depth of the reservoir controls the pressure and temperature at the base of the fault (reservoir). For all overpressures, increase in depth (> 1000 m) decreased the leakage mass flux for geothermal case and increased for flowing total enthalpy case. The leakage risk decreased with the increase in depth beyond 1100 m for all overpressure scenarios.

The maximum leakage mass flux through a fault with a permeability of 1000 md and other properties as mentioned in Table 3.1 was 0.044 kg/s/m^2 or 1,387,584 kg/yr/m^2.

The mass flux decreased to 0.032 kg/s/m^2 or 1,009,152 kg/yr/m^2 after liquid and hydrate formation. The multiphase coexistence conditions and hydrate formation reduced fluxes about 30% for all cases. The magnitude of flux reduction depends on the relative permeability model used to account for multiphase flow, which is very uncertain because of the lack of experimental data for multiphase flow in faults. For comparison, the leakage mass flux from natural analogues discussed in Chapter 1 range between 1.25 x 10^{-3} and 5.78 x 10^{-5} kg/s/m^2 and the CO_2 background flux at earth's surface is up to 2 x 10^{-7} kg/s/m^2 (Allis et al., 2005). The leakage area for the natural analogues discussed in Chapter 1 ranged from 1000 to 500,000 m^2 (Lewicki et al., 2007).

Leakage mass flux calculated from the model is expressed independent of the cross-sectional area of the fault. For an assumed area of 1 m^2, the multiphase flow leakage rate would be 3.2 x 10^{-2} kg/s or 1,009,000 kg/yr, or 100,000 tonnes over 100 years. Assuming 20 million tonnes of CO_2 are initially stored in the reservoir, less than 0.5% of the CO_2 would leak over a period of 100 years. This result is sensitive to the area of the fault and to attenuation to intersecting permeable layers among other factors. Observations from natural analogues suggest that the cross-sectional area of the fault leaking CO_2 increases near the surface. The total leakage rate from Solfatara, Italy is estimated as 17.36 kg/s with diffuse leakage over an area of 500,000 m^2 (Lewicki et al., 2007). Although the computed leakage mass fluxes from the fault modelled in this work are were higher than the natural analogues, the computed leakage rates are 1000 times lower than for the Solfatara site. Hence it is very important to know the cross-sectional area of a leaking fault.

The fluxes computed from the model developed in this research are higher than the values computed from models reported in the literature (Lu et al., 2012; Pruess 2004, 2007, 2008, 2011), which assumed different fault conditions such as assuming the fault is

saturated with 100% brine before leakage, different fluid properties and different relative permeability models. Assuming the fault is at residual water saturation as done here results in a higher computed CO_2 leakage mass flux.

All the calculations have limitations due to the idealized representation of the fault. Actual faults have complex geological characteristics. There is a large uncertainty in fault parameters such as permeability and width and considerable difficulty in measuring them. In order to assess the impact of low permeability layers on leakage, a calculation for mass flux for a heterogeneous fault was presented in Chapter 3. The estimated leakage mass flux decreased by a factor of 7 compared to the flux calculated for a homogenous fault with a permeability of 1000 md. Joule- Thomson like cooling was observed as the CO_2 passed through the low permeability layers as evidenced by the pressure drop and the temperature decline.

The models developed in this research were used to estimate the effect of multiphase coexistence and hydrate formation on the leakage mass flux. However, the mass flux estimates should be considered as relative values based on the idealized assumptions and approximations rather than predictions of actual values. The purpose was to determine the impact of multiphase coexistence and non-isothermal flow on the leakage mass flux and to gain insight into the effect of different parameters such as fault permeability and fault effective width. The geometry and properties of an actual fault will be much more complex than assumed in these simple models. The results from Chapter 3 indicate that phase changes need to be taken into account for faults with high permeability and high effective width to avoid over predicting the leakage mass flux. However, the uncertainty in estimating leakage is likely to be greater than the impact of the phase changes.

5.2 FUTURE WORK

Future research should focus on modeling faults with more realistic characteristics to improve the estimates of CO_2 leakage from storage reservoirs. Some important factors to consider are:

1) The numerical model should be extended to 3-D to include more realistic geological models of the fault and the surrounding formations.
2) Research is needed to determine realistic fault zone characteristics.
3) A better representation of fluid flow parameters is needed to obtain realistic leakage estimates. As a first step, an uncertainty analysis of the relative permeability parameters should be considered.
4) Only CO_2 was allowed to leak through faults in the current simulation study. However, for an overpressured reservoir brine near the leakage source will also flow. Hence, the numerical model should be extended to include the flow of water in the fault.
5) The phase behavior model should also include the solubility of CO_2 in the water and the solubility of water in the gas and CO_2 liquid.
6) Geochemical reactions should be included in the model.
7) The dynamic nature of the fault was neglected in this study. The presence of overpressure in the reservoir will alter the stress states and reactivate fault and alter porosity/permeability of faults. The numerical flow model should be coupled with geomechanical models.

REFERENCES

Abanades, J.C., Arias, B., Lyngfelt, A., Mattisson, T., Wiley, D.E., Li, H., Ho, M.T., Mangano, E. and Brandani, S., 2015. Emerging CO 2 capture systems. *International Journal of Greenhouse Gas Control*, *40*, pp.126-166.

Adisasmito, S., Frank III, R.J. and Sloan Jr, E.D., 1991. Hydrates of carbon dioxide and methane mixtures. *Journal of Chemical and Engineering Data*, *36*(1), pp.68-71.

Allis, R., Bergfeld, D., Moore, J., McClure, K., Morgan, C., Chidsey, T., Heath, J. and McPherson, B., 2005, May. Implications of results from CO2 flux surveys over known CO2 systems for long-term monitoring. In *Fourth annual conference on carbon capture and sequestration, DOE/NETL*.

Alnes, H., Eiken, O., Nooner, S., Sasagawa, G., Stenvold, T. and Zumberge, M., 2011. Results from sleipner gravity monitoring: Updated density and temperature distribution of the CO2 plume. *Energy Procedia*, *4*, pp.5504-5511.

Aydin, A., 2000. Fractures, faults, and hydrocarbon entrapment, migration and flow. *Marine and petroleum geology*, *17*(7), pp.797-814.

Bachu, S. (2000). Sequestration of CO 2 in geological media: criteria and approach for site selection in response to climate change. *Energy conversion and management*, *41*(9), 953-970.

Bachu, S. (2015). Review of CO_2 storage efficiency in deep saline aquifers. Int. J. Greenh. Gas Control, http://dx.doi.org/10.1016/j.ijggc.2015.01.007 (in press).

Baklid, A., Korbol, R. and Owren, G., 1996, January. Sleipner Vest CO2 disposal, CO2 injection into a shallow underground aquifer. In *SPE Annual Technical Conference and Exhibition*. Society of Petroleum Engineers. SPE-36600-MS

Barton, P.B. and Toulmin, P., 1961. Some mechanisms for cooling hydrothermal fluids. *US Geological Survey Professional Paper*, *424*, pp.348-352.

Benson, S. (2006). Monitoring Carbon Dioxide Sequestration in Deep Geological Formations for Inventory Verification and Carbon Credits. Proceedings of SPE Annual Technical Conference and Exhibition. Society of Petroleum Engineers. 102833-MS

Benson, S. M., Hepple, R., Apps, J., Tsang, C. F., & Lippmann, M. (2002). Lessons learned from natural and industrial analogues for storage of carbon dioxide in deep geological formations. *Lawrence Berkeley National Laboratory*.

Benson, S.M., Bennaceur, K., Cook, P., Davison, J., de Coninck, H., Farhat, K., Ramirez, C.A., Simbeck, D., Surles, T., Verma, P. and Wright, I., 2012. Carbon capture and storage. Global Energy Assessment-Toward a Sustainable Future, p.993.

Bielinski, A., Kopp, A., Schütt, H. and Class, H., 2008. Monitoring of CO 2 plumes during storage in geological formations using temperature signals: numerical investigation. *International journal of greenhouse gas control*, *2*(3), pp.319-328.

Blunt, M., Fayers, F. J., & Orr, F. M. (1993). Carbon dioxide in enhanced oil recovery. *Energy Conversion and Management*, *34*(9), 1197-1204.

Boreham, C., Underschultz, J., Stalker, L., Kirste, D., Freifeld, B., Jenkins, C. and Ennis-King, J., 2011. Monitoring of CO 2 storage in a depleted natural gas reservoir: gas

geochemistry from the CO2CRC Otway Project, Australia. *International Journal of Greenhouse Gas Control*, *5*(4), pp.1039-1054.

Böttcher, N., Taron, J., Kolditz, O., Park, C.H. and Liedl, R., 2012. Evaluation of thermal equations of state for CO2 in numerical simulations. *Environmental Earth Sciences*, *67*(2), pp.481-495.

Bourne, S., Crouch, S. and Smith, M., 2014. A risk-based framework for measurement, monitoring and verification of the Quest CCS Project, Alberta, Canada. *International Journal of Greenhouse Gas Control*, *26*, pp.109-126.

Brantferger, K.M., 1990. Development of a thermodynamically consistent, fully implicit, compositional, equation-of-state, steamflood simulator. PhD Dissertation

Brown, D.W., 2000, January. A hot dry rock geothermal energy concept utilizing supercritical CO2 instead of water. In *Proceedings of the twenty-fifth workshop on geothermal reservoir engineering, Stanford University* (pp. 233-238).

Busch, A., Alles, S., Gensterblum, Y., Prinz, D., Dewhurst, D. N., Raven, M. D., Stanjek, H., & Krooss, B. M. (2008). Carbon dioxide storage potential of shales.*International Journal of Greenhouse Gas Control*, *2*(3), 297-308.

Busch, A., Amann-Hildenbrand, A., Bertier, P., Waschbuesch, M. and Krooss, B.M., 2010, January. The significance of caprock sealing integrity for CO2 storage. In *SPE International Conference on CO2 Capture, Storage, and Utilization*. Society of Petroleum Engineers.

Caine, J.S., Evans, J.P. and Forster, C.B., 1996. Fault zone architecture and permeability structure. *Geology*, *24*(11), pp.1025-1028.

Cappa, F. and Rutqvist, J., 2011. Modeling of coupled deformation and permeability evolution during fault reactivation induced by deep underground injection of CO 2. *International Journal of Greenhouse Gas Control*, *5*(2), pp.336-346.

Celia, M.A., Bachu, S., Nordbotten, J.M., Gasda, S.E. and Dahle, H.K., 2004, September. Quantitative estimation of CO2 leakage from geological storage: Analytical models, numerical models and data needs. In *Proceedings of 7th International Conference on Greenhouse Gas Control Technologies. (GHGT-7)* (pp. 663-672).

Chadwick, A., Williams, G., Delepine, N., Clochard, V., Labat, K., Sturton, S., Buddensiek, M.L., Dillen, M., Nickel, M., Lima, A.L. and Arts, R., 2010. Quantitative analysis of time-lapse seismic monitoring data at the Sleipner CO2 storage operation. *The Leading Edge*

Chang, K.W., Minkoff, S.E. and Bryant, S.L., 2008, January. Modeling leakage through faults of CO2 stored in an aquifer. In *SPE Annual Technical Conference and Exhibition*. Society of Petroleum Engineers.

Childs, C., Manzocchi, T., Walsh, J.J., Bonson, C.G., Nicol, A. and Schöpfer, M.P., 2009. A geometric model of fault zone and fault rock thickness variations. *Journal of Structural Geology*, *31*(2), pp.117-127.

Dixon, T., McCoy, S.T. and Havercroft, I., 2015. Legal and regulatory developments on CCS. *International Journal of Greenhouse Gas Control*, *40*, pp.431-448.

Dodson, M.H., 1971. Isenthalpic Flow, Joule—Kelvin Coefficients and Mantle Convection. *Nature*, *234*.

Dusseault, M. B., Bachu, S., & Rothenburg, L. (2004). Sequestration of CO in Salt Caverns. *Journal of Canadian Petroleum Technology*, *43*(11).

EIA, Energy Information Administration, (2014) (http://www.eia.gov/totalenergy/)

Emberley, S., Hutcheon, I., Shevalier, M., Durocher, K., Mayer, B., Gunter, W.D. and Perkins, E.H., 2005. Monitoring of fluid–rock interaction and CO 2 storage through produced fluid sampling at the Weyburn CO 2-injection enhanced oil recovery site, Saskatchewan, Canada. *Applied Geochemistry*, *20*(6), pp.1131-1157.

Fan, S.S. and Guo, T.M., 1999. Hydrate formation of CO2-rich binary and quaternary gas mixtures in aqueous sodium chloride solutions. *Journal of Chemical & Engineering Data*, *44*(4), pp.829-832.

Faulkner, D.R., Jackson, C.A.L., Lunn, R.J., Schlische, R.W., Shipton, Z.K., Wibberley, C.A.J. and Withjack, M.O., 2010. A review of recent developments concerning the structure, mechanics and fluid flow properties of fault zones. *Journal of Structural Geology*, *32*(11), pp.1557-1575.

Faust, C. R. and Mercer, J.W. (1979a). Geothermal reservoir simulation: 1. Mathematical models for liquid-and vapor-dominated hydrothermal systems. *Water resources research*, *15*(1), 23-30.

Faust, C. R. and Mercer, J.W. (1979b). Geothermal reservoir simulation: 2. Numerical solution techniques for liquid-and vapor-dominated hydrothermal systems. *Water Resources Research*, *15*(1), 31-46.

Faust, C.R. and Mercer, J.W., 1976. January. An analysis of finite-difference and finite-element techniques for geothermal reservoir simulation. In *SPE Symposium on Numerical Simulation of Reservoir Performance*. Society of Petroleum Engineers.

Faust, C.R. and Mercer, J.W., 1977a. *Finite-difference model of two-dimensional, single, and two-phase heat transport in a porous medium-Version I* (No. 77-234). US Geological Survey,.

Faust, C.R. and Mercer, J.W., 1977b. *A theoretical analysis of fluid flow and energy transport in hydrothermal systems* (No. 77-60). US Geological Survey,

Fenghour, A., Wakeham, W.A. and Vesovic, V., 1998. The viscosity of carbon dioxide. *Journal of Physical and Chemical Reference Data*, *27*(1), pp.31-44.

Fisher, Q.J. and Knipe, R., 1998. Fault sealing processes in siliciclastic sediments. *Geological Society, London, Special Publications*, *147*(1), pp.117-134.

Freifeld, B., Daley, T., Cook, P., Trautz, R. and Dodds, K., 2014. The Modular Borehole Monitoring Program: a research program to optimize well-based monitoring for geologic carbon sequestration. *Energy Procedia*, *63*, pp.3500-3515.

Ganguly, J., 2005. Adiabatic decompression and melting of mantle rocks: An irreversible thermodynamic analysis. *Geophysical research letters*, *32*(6).

GEM, C., 2014. Computer Modelling Group. *Calgary, Alberta Canada*.

Gunter, W.D., Bachu, S. and Benson, S., 2004. The role of hydrogeological and geochemical trapping in sedimentary basins for secure geological storage of carbon dioxide. *Geological Society, London, Special Publications*, *233*(1), pp.129-145.

Hagoort, J., 2005. Prediction of wellbore temperatures in gas production wells. *Journal of Petroleum Science and Engineering*, *49*(1), pp.22-36

Hayba, D.O. and Ingebritsen, S.E., 1994a. *The computer model HYDROTHERM, a three-dimensional finite-difference model to simulate ground-water flow and heat transport in the temperature range of 0 to 1,200 degrees C* (No. 94-4045). US Geological Survey; USGS Earth Science Information Center, Open-File Reports Section [distributor].

Hayba, D.O. and Ingebritsen, S.E., 1994b. *Flow near the critical point: examination of some pressure-enthalpy paths* (No. SGP-TR-147-12). US Geological Survey, Reston, VA; US Geological Survey, Menlo Park, CA.

IEA Greenhouse Gas R&D Programme (IEA GHG), "Remediation of Leakage form CO2 Storage Reservoirs, 2007/11, September 2007".

IEAGHG, "Fault Permeability" 2016/13, October, 2016

Ingebritsen, S.E. and Manning, C.E., 2010. Permeability of the continental crust: dynamic variations inferred from seismicity and metamorphism. *Geofluids*, *10*(1-2), pp.193-205.

Ingebritsen, S.E. and Rojstaczer, S.A., 1996. Geyser periodicity and the response of geysers to deformation. *Journal of Geophysical Research: Solid Earth*, *101*(B10), pp.21891-21905.

Ingebritsen, S.E., Geiger, S., Hurwitz, S. and Driesner, T., 2010. Numerical simulation of magmatic hydrothermal systems. *Reviews of Geophysics*, *48*(1).

International Energy Agency Report. 2004 Improvements in power generation with post-combustion capture of CO2. IEA Greenhouse Gas R&D Programmes, PH4/33;

IPCC (Intergovernmental Panel on Climate Change), (2005). Special Report on Carbon Dioxide Capture and Storage. Cambridge University Press, Cambridge, UK, New York, NY, USA.

IPCC (Intergovernmental Panel on Climate Change), (2014). Summary for policymakers. In: Edenhofer, O., Pichs-Madruga, R., Sokona, Y., Farahani, E., Kadner, S., Seyboth, K., Adler, A., Baum, I., Brunner, S., Eickemeier, P., Kriemann, B., Savolainen, J., Sclömer, S., von Stechow, C., Zwickel, T., Minx, J.C. (Eds.), Contribution of Working Group III to the Fifth Assessment Report of the Intergovernmental Panel on Climate Change. Cambridge University Press, Cambridge, UK, New York, NY, USA

Jaffe, P. R., & Wang, S. (2003). Potential effect of CO2 releases from deep reservoirs on the quality of fresh-water aquifers. In *Sixth International Conference on Greenhouse Gas Control Technologies, Kyoto* (Vol. 2, pp. 1657-1660).

Jansen, D., Gazzani, M., Manzolini, G., van Dijk, E. and Carbo, M., 2015. Pre-combustion CO 2 capture. *International Journal of Greenhouse Gas Control*, *40*, pp.167-187.

Jenkins, C., Chadwick, A. and Hovorka, S.D., 2015. The state of the art in monitoring and verification—Ten years on. *International Journal of Greenhouse Gas Control*, *40*, pp.312-349.

Jimenez, J. and Chalaturnyk, R.J., "Are discussed oil and gas reservoir safe for the geological storage of CO2?" 6th International Conference on Greenhouse Gas Control Technologies, Kyoto; Vol.I; pp.471-476, 2003

Jones, D.G., Beaubien, S.E., Blackford, J.C., Foekema, E.M., Lions, J., De Vittor, C., West, J.M., Widdicombe, S., Hauton, C. and Queirós, A.M., 2015. Developments since 2005 in understanding potential environmental impacts of CO 2 leakage from geological storage. *International Journal of Greenhouse Gas Control*, *40*, pp.350-377.

Jung, N.H., Han, W.S., Han, K. and Park, E., 2015. Regional-scale advective, diffusive, and eruptive dynamics of CO2 and brine leakage through faults and wellbores. *Journal of Geophysical Research: Solid Earth*, *120*(5), pp.3003-3025.

Kiessling, D., Schmidt-Hattenberger, C., Schuett, H., Schilling, F., Krueger, K., Schoebel, B., Danckwardt, E., Kummerow, J. and CO2SINK Group, 2010. Geoelectrical methods for monitoring geological CO 2 storage: first results from cross-hole and surface–downhole measurements from the CO 2 SINK test site at Ketzin (Germany). *International Journal of Greenhouse Gas Control*, *4*(5), pp.816-826.

Kipp, K.L., Hsieh, P.A. and Charlton, S.R., 2008. *Guide to the revised ground-water flow and heat transport simulator: HYDROTHERM-Version 3* (No. 6-A25). Geological Survey (US).

Konno, U., Tsunogai, U., Nakagawa, F., Nakaseama, M., Ishibashi, J.I., Nunoura, T. and Nakamura, K.I., 2006. Liquid CO2 venting on the seafloor: Yonaguni Knoll IV hydrothermal system, Okinawa Trough. *Geophysical research letters*, *33*(16).

Krooss, B.M., Busch, A., Alles, S. and Hildenbrand, A., 2003, November. Experimental investigation of molecular diffusion of CO2 in coals and shales. In *International Conference on Gas-Water-Rock Interactions Induced by Reservoir Exploitation, CO2 Sequestration, and other Geological Storage. IFP, Rueil-Malmaison, France* (pp. 18-20).

Kumar, A., Maini, B., Bishnoi, P.R., Clarke, M., Zatsepina, O. and Srinivasan, S., 2010. Experimental determination of permeability in the presence of hydrates and its effect on the dissociation characteristics of gas hydrates in porous media. *Journal of Petroleum Science and Engineering*,*70*(1), pp.114-122.

Kumar, A., Noh, M. H., Ozah, R. C., Pope, G. A., Bryant, S. L., Sepehrnoori, K., & Lake, L. W. (2005). Reservoir Simulation of CO 2 Storage in Aquifers.*Spe Journal*, *10*(03), 336-348.

Lauwerier, H.A., 1955. The transport of heat in an oil layer caused by the injection of hot fluid. *Applied Scientific Research, Section A*, *5*(2-3), pp.145-150.

Leung, D. Y., Caramanna, G., & Maroto-Valer, M. M. (2014). An overview of current status of carbon dioxide capture and storage technologies. *Renewable and Sustainable Energy Reviews*, *39*, 426-443.

Leuning, R., Etheridge, D., Luhar, A. and Dunse, B., 2008. Atmospheric monitoring and verification technologies for CO 2 geosequestration. *International Journal of Greenhouse Gas Control*, *2*(3), pp.401-414.

Lewicki, J.L., Birkholzer, J. and Tsang, C.F., 2007. Natural and industrial analogues for leakage of CO2 from storage reservoirs: identification of features, events, and processes and lessons learned. *Environmental Geology*, *52*(3), p.457.

Liang, Z.H., Rongwong, W., Liu, H., Fu, K., Gao, H., Cao, F., Zhang, R., Sema, T., Henni, A., Sumon, K. and Nath, D., 2015. Recent progress and new developments in post-combustion carbon-capture technology with amine based solvents. *International Journal of Greenhouse Gas Control*, *40*, pp.26-54.

Lu, C., Sun, Y., Buscheck, T.A., Hao, Y., White, J.A. and Chiaramonte, L., 2012. Uncertainty quantification of CO2 leakage through a fault with multiphase and nonisothermal effects. *Greenhouse Gases: Science and Technology*, *2*(6), pp.445-459.

Lupton, J., Butterfield, D., Lilley, M., Evans, L., Nakamura, K.I., Chadwick, W., Resing, J., Embley, R., Olson, E., Proskurowski, G. and Baker, E., 2006. Submarine venting of liquid carbon dioxide on a Mariana Arc volcano. *Geochemistry, Geophysics, Geosystems*, *7*(8).

Lupton, J., Lilley, M., Butterfield, D., Evans, L., Embley, R., Massoth, G., Christenson, B., Nakamura, K.I. and Schmidt, M., 2008. Venting of a separate CO2-rich gas phase from submarine arc volcanoes: Examples from the Mariana and Tonga-Kermadec arcs. *Journal of Geophysical Research: Solid Earth*, *113*(B8).

Mastin, L.G. and Ghiorso, M.S., 2001. Adiabatic temperature changes of magma–gas mixtures during ascent and eruption. *Contributions to Mineralogy and Petrology*, *141*(3), pp.307-321.

Masuda, Y., Naganawa, S., Ando, S. and Sato, K., 1997, June. Numerical calculation of gas-production performance from reservoirs containing natural gas hydrates. In *SPE Asia Pacific Oil and Gas Conference* (pp. 14-17).

Mathieson, A., Midgely, J., Wright, I., Saoula, N. and Ringrose, P., 2011. In Salah CO2 Storage JIP: CO2 sequestration monitoring and verification technologies applied at Krechba, Algeria. *Energy Procedia*, *4*, pp.3596-3603.

Matter, J. M., Broecker, W. S., Stute, M., Gislason, S. R., Oelkers, E. H., Stefánsson, A., Wolff-Boenisch, D., Gunnlaugsson, E., Axelsson, G., & Björnsson, G. (2009). Permanent carbon dioxide storage into basalt: the CarbFix pilot project, Iceland. *Energy Procedia*, *1*(1), 3641-3646.

Mazzoldi, A., Rinaldi, A.P., Borgia, A. and Rutqvist, J., 2012. Induced seismicity within geological carbon sequestration projects: maximum earthquake magnitude and leakage potential from undetected faults. *International Journal of Greenhouse Gas Control*, *10*, pp.434-442.

Mazzotti, M., Pini, R. and Storti, G., 2009. Enhanced coalbed methane recovery. *The Journal of Supercritical Fluids*, *47*(3), pp.619-627.

Mercer, J.W. and Faust, C.R. 1975. January. Simulation of water-and vapor-dominated hydrothermal reservoirs. In *Fall Meeting of the Society of Petroleum Engineers of AIME*. Society of Petroleum Engineers.

Mercer, J.W. and Faust, C.R., 1979. Geothermal reservoir simulation: 3. Application of liquid-and vapor-dominated hydrothermal modeling techniques to Wairakei, New Zealand. *Water Resources Research*, *15*(3), pp.653-671.

Mercer, J.W., Faust, C.R., Miller, W.J. and Pearson Jr, F.J., 1982. Review of simulation techniques for aquifer thermal energy storage (ATES). *Adv. Hydrosci*, *13*, pp.1-129.

Myers, M., Stalker, L., Pejcic, B. and Ross, A., 2013. Tracers–Past, present and future applications in CO 2 geosequestration. *Applied geochemistry*, *30*, pp.125-135.

Ng, H.J. and Robinson, D.B., 1985. Hydrate formation in systems containing methane, ethane, propane, carbon dioxide or hydrogen sulfide in the presence of methanol. *Fluid Phase Equilibria*, *21*(1-2), pp.145-155.

NIST, National Institute of Standards and Technology, (2015) Thermophysical properties database. http://webbook.nist.gov/chemistry/fluid/

NOAA, National Oceanic and Atmospheric Administration, (2015) (http://www.esrl.noaa.gov/gmd/ccgg/trends)

Nordbotten, J.M., Celia, M.A., Bachu, S. and Dahle, H.K., 2005., Semianalytical solution for CO2 leakage through an abandoned well. *Environmental science & technology*, *39*(2), pp.602-611.

Norton, D. and Knight, J., 1977. Transport phenomena in hydrothermal systems: cooling plutons. *Am. J. Sci.;(United States)*, *277*.

Paterson, L., Lu, M., Connell, L. and Ennis-King, J.P., 2008, January. Numerical modeling of pressure and temperature profiles including phase transitions in carbon dioxide wells. In *SPE Annual Technical Conference and Exhibition*. Society of Petroleum Engineers.

Pawar, R.J., Bromhal, G.S., Carey, J.W., Foxall, W., Korre, A., Ringrose, P.S., Tucker, O., Watson, M.N. and White, J.A., 2015, Recent advances in risk assessment and risk management of geologic CO2 storage. *International Journal of Greenhouse Gas Control*, *40*, pp.292-311.

Pearce, J., Baker, J., Beaubien, S., Brune, S., Czemichowski-Lauriol, I., Faber, E., Hatziyannis, G., Hildenbrand, A., Krooss, B. M., Lombardi, S., Nador, A., Pauwels, H., and Schroot, B., 2002. Natural CO_2accumulations in Europe: understanding long-term geological processes in CO_2 sequestration, Proceedings of the 6th International Conference on Greenhouse Gas Control Technologies (GHGT-6), Kyoto, Japan: 105 – 111.

Pedersen, K.S., Christensen, P.L. and Shaikh, J.A., 2014. *Phase behavior of petroleum reservoir fluids*. CRC Press.

Pedersen, K.S., Fredenslund, A., Christensen, P.L. and Thomassen, P., 1984. Viscosity of crude oils. *Chemical Engineering Science*, *39*(6), pp.1011-1016.

Peng, D. Y., & Robinson, D. B. A new two-constant equation of state.*Industrial & Engineering Chemistry Fundamentals*, *15*(1), 59-64, 1976.

Pruess, K., 2004. Numerical simulation of CO2 leakage from a geologic disposal reservoir, including transitions from super-to subcritical conditions, and boiling of liquid CO2. *Spe Journal*, *9*(02), pp.237-248.

Pruess, K., 2005. Numerical studies of fluid leakage from a geologic disposal reservoir for CO2 show self-limiting feedback between fluid flow and heat transfer. *Geophysical research letters*, *32*(14).

Pruess, K., 2008. On CO2 fluid flow and heat transfer behavior in the subsurface, following leakage from a geologic storage reservoir. *Environmental Geology*, *54*(8), pp.1677-1686.

Pruess, K., 2011. Integrated modeling of CO2 storage and leakage scenarios including transitions between super-and subcritical conditions, and phase change between liquid and gaseous CO2. *Greenhouse Gases: Science and Technology*, *1*(3), pp.237-247.

Pruess, K., Moridis, G., Oldenburg, C., & Laboratory, L. B. N. (1999). TOUGH2 user's guide, version 2.0. Contract (Vol. 43134). Lawrence Berkeley National Laboratory Berkeley, CA.

Ramachandran, H., Pope, G.A. and Srinivasan, S., 2014. Effect of Thermodynamic Phase Changes on CO2 leakage. *Energy Procedia*, *63*, pp.3735-3745.

Ramachandran, H., Pope, G.A. and Srinivasan, S., 2017. Numerical Study on the Effect of Thermodynamic Phase Changes on CO2 leakage. *Energy Procedia*, *114C*, pp.3511-3519.

Ramberg, H.. Temperature changes associated with adiabatic decompression in geological processes. Nature, 234, 539-540. 1971

Randolph, J.B. and Saar, M.O., 2011. Coupling carbon dioxide sequestration with geothermal energy capture in naturally permeable, porous geologic formations: Implications for CO2 sequestration. *Energy Procedia*, *4*, pp.2206-2213.

Rao AB, Rubin ES (2002) A technical, economic, and environmental assessment of amine based CO2 capture technology for power plant greenhouse gas control. Environ Sci Technol 36(20):4467–4475

Reeves, S.R., 2001, January. Geological sequestration of CO2 in deep, unmineable coalbeds: an integrated research and commerical-scale field demonstration project. In *SPE annual technical conference and exhibition*. Society of Petroleum Engineers.

Rinaldi, A.P., Jeanne, P., Rutqvist, J., Cappa, F. and Guglielmi, Y., 2014. Effects of fault-zone architecture on earthquake magnitude and gas leakage related to CO2 injection in a multi-layered sedimentary system. *Greenhouse Gases: Science and Technology*, *4*(1), pp.99-120.

Rinaldi, A.P., Jeanne, P., Rutqvist, J., Cappa, F. and Guglielmi, Y., 2014. Effects of fault-zone architecture on earthquake magnitude and gas leakage related to CO2 injection in a multi-layered sedimentary system. *Greenhouse Gases: Science and Technology*, *4*(1), pp.99-120.

Ringrose, P.S., Mathieson, A.S., Wright, I.W., Selama, F., Hansen, O., Bissell, R., Saoula, N. and Midgley, J., 2013. The In Salah CO 2 storage project: lessons learned and knowledge transfer. *Energy Procedia*, *37*, pp.6226-6236..

RISCS, (2014). A Guide to Potential Impacts Of Leakage From CO_2 Storage. British Geological Survey, 70.

Romanak, K.D., Bennett, P.C., Yang, C. and Hovorka, S.D., 2012. Process-based approach to CO2 leakage detection by vadose zone gas monitoring at geologic CO2 storage sites. *Geophysical Research Letters*, *39*(15).

Rostron, B., White, D., Hawkes, C. and Chalaturnyk, R., 2014. Characterization of the Aquistore CO2 project storage site, Saskatchewan, Canada. *Energy Procedia*, *63*, pp.2977-2984.

Rubin, E. S., Davison, J. E., & Herzog, H. J. (2015) The cost of CO 2 capture and storage. *International Journal of Greenhouse Gas Control*, *40*, 378-400.

Rutqvist, J., 2012. The geomechanics of CO2 storage in deep sedimentary formations. *Geotechnical and Geological Engineering*, *30*(3), pp.525-551.

Rutqvist, J., Birkholzer, J., Cappa, F. & Tsang, C.F. (2007). Estimating maximum sustainable injection pressure during geological sequestration of CO2 using coupled fluid flow and geomechanical fault-slip analysis. Energy Conversion and Management, 48(6), 1798-1807.

Sakai, H., Gamo, T., Kim, E.S., Tsutsumi, M., Tanaka, T., Ishibashi, J., Wakita, H., Yamano, M. and Oomori, T., 1990. Venting of carbon dioxide-rich fluid and hydrate formation in mid-Okinawa trough backarc basin. *Science*, *248*(4959), pp.1093-1097.

Seebeck, H., Nicol, A., Walsh, J.J., Childs, C., Beetham, R.D. and Pettinga, J., 2014. Fluid flow in fault zones from an active rift. *Journal of Structural Geology*, *62*, pp.52-64.

Seifritz, W. (1990). CO2 disposal by means of silicates. *Nature*, *345*, 486.

Sorey, M.L., Evans, W.C., Kennedy, B.M., Farrar, C.D., Hainsworth, L.J. and Hausback, B., 1998. Carbon dioxide and helium emissions from a reservoir of magmatic gas beneath Mammoth Mountain, California. *Journal of Geophysical Research: Solid Earth*, *103*(B7), pp.15303-15323.

Span, R. and Wagner, W., 2003. Equations of state for technical applications. I. Simultaneously optimized functional forms for nonpolar and polar fluids. *International journal of thermophysics*, *24*(1), pp.1-39.

Stangeland, A., & Laird, B., (2006). Energy Infrastructure with CO_2 Capture and Storage (CCS).

Stanger, R., Wall, T., Spoerl, R., Paneru, M., Grathwohl, S., Weidmann, M., Scheffknecht, G., McDonald, D., Myöhänen, K., Ritvanen, J. and Rahiala, S., 2015. Oxyfuel combustion for CO 2 capture in power plants. *International Journal of Greenhouse Gas Control*, *40*, pp.55-125.

Stevens, S. H., Kuuskraa, V. A., Gale, J. and Beecy, D. (2001), CO_2 Injection and Sequestration in Depleted Oil and Gas Fields and Deep Coal Seams: Worldwide Potential and Costs. Environmental Geosciences, 8: 200–209. doi: 10.1046/j.1526-0984.2001.008003200.x

Streit, J.E. and Hillis, R.R., 2004. Estimating fault stability and sustainable fluid pressures for underground storage of CO 2 in porous rock. *Energy*, *29*(9), pp.1445-1456.\

Streit, J.E., and Watson, M.N., 2004. Estimating Rates of Potential CO2 Loss from Geological Storage Sites for Risk and Uncertainty Analysis, GHGT-7 2004, Vancouver, Canada: 1309-1314

Sun, A.Y., Nicot, J.P. and Zhang, X., 2013. Optimal design of pressure-based, leakage detection monitoring networks for geologic carbon sequestration repositories. *International Journal of Greenhouse Gas Control*, *19*, pp.251-261.

Tao, Q., 2012. Modeling CO2 Leakage from Geological Storage Formation and Reducing the Associated Risk. *University of Texas*.

UNFCCC. (2015a). Decision 1/CP.21, in report of the conference of the parties on its twenty-first session, held in Paris from 30 November to 13 December 2015. Addendum Part two: Action taken by the Conference of the Parties at its twenty-first session (FCCC/CP/2015/10/Add.1).

UNFCCC. (2015b). Synthesis report on the aggregate effect of the intended nationally determined contributions (FCCC/CP/2015/7).

Varavei, A., 2009. Development of an equation-of-state thermal flooding simulator. PhD Dissertation

Vesovic, V., Wakeham, W.A., Olchowy, G.A., Sengers, J.V., Watson, J.T.R. and Millat, J., 1990. The transport properties of carbon dioxide. *Journal of physical and chemical reference data*, *19*(3), pp.763-808.

Vinsome, P. K. W., and J. Westerveld. "A Simple Method For Predicting Cap And Base Rock Heat Losses In Thermal Reservoir Simulators." *Journal of Canadian Petroleum Technology* 19(03), (1980).

Wall, T.F., 2007. Combustion processes for carbon capture. *Proceedings of the combustion institute*, *31*(1), pp.31-47.

Wendland, M., Hasse, H. and Maurer, G., 1999. Experimental pressure− temperature data on three-and four-phase equilibria of fluid, hydrate, and ice phases in the system carbon dioxide− water. *Journal of Chemical & Engineering Data*, *44*(5), pp.901-906.

West, J.M., Pearce, J., Bentham, M. and Maul, P., 2005. Issue profile: environmental issues and the geological storage of CO2. *Environmental Policy and Governance*, *15*(4), pp.250-259.

Wigley, T.M. L., Richels, R. & Edmonds, J.A. (1996) Economic and environmental choices in the stabilization of atmospheric CO2 concentrations. *Nature 379*, 240–243

Wollenweber, J., Alles, S., Busch, A., Krooss, B.M., Stanjek, H. and Littke, R., 2010. Experimental investigation of the CO 2 sealing efficiency of caprocks. *International Journal of Greenhouse Gas Control*, *4*(2), pp.231-241.

Wright, I.W., Lee, A., Middleton, P., Lowe, C., Imbus, S.W. and Miracca, I., 2004, January. CO2 Capture Project: Initial Results. In *SPE International Conference on Health, Safety, and Environment in Oil and Gas Exploration and Production*. Society of Petroleum Engineers.